Flexible Fibers for Optoelectronic Probing of Spinal Cord Circuits

By

Chi Lu

B.S. Materials Science and Engineering, University of Illinois at Urbana-Champaign, 2012
M.S. Materials Science and Engineering, University of Illinois at Urbana-Champaign, 2012

Submitted to the Department of Materials Science and Engineering
in Partial Fulfillment of the Requirements for the Degree of

Doctor of Philosophy in Program in Polymers and Soft Matter
and Materials Science and Engineering

at the

MASSACHUSETTS INSTITUTE OF TECHNOLOGY

May 2017 [June 2017]

Signature of Author..... Signature redacted .....
Department of Materials Science and Engineering
April 28, 2017

Certified by..... Signature redacted .....
Polina Anikeeva
Professor of Materials Science and Engineering
Thesis Supervisor

Accepted by..... Signature redacted .....
Donald Sadoway
Chair, Departmental Committee on Graduate Students

Flexible Fibers for Optoelectronic Probing of Spinal Cord Circuits

by
Chi Lu

Submitted to Department of Materials Science and Engineering
on April 28th, 2017, in Partial Fulfillment of the Requirements for the Degree of
Doctor of Philosophy in Program in Polymers and Soft Matter
and Materials Science and Engineering

ABSTRACT

The majority of the neural engineering efforts in the past decade have focused on brain interfaces. The searching of tools for recording and modulation of neural activity in the spinal cord limits fundamental understanding of neural dynamics in this organ. Spinal cord poses a challenge to probe design due to its fibrous structure, repeated deformation, low elastic modulus, and sensitivity to implantation procedures. This work addresses the elastic modulus mismatch between spinal cord tissue and synthetic devices by designing flexible multifunctional neural probes capable of conforming to the spinal cord geometry and mechanical properties, while providing functions for optical stimulation and neural recording. In this thesis, fiber drawing techniques are applied to produce flexible and stretchable probes.

The utility of the devices for recording and optical stimulation is demonstrated in the spinal cord of transgenic mice expressing the light sensitive protein channelrhodopsin 2 (ChR2). Furthermore, it is shown that the optical stimulation of the spinal cord with the polymer fiber probes induces on-demand limb movements. Finally, the modest dimensions and high flexibility of the devices permitting chronic implantation into the mouse spinal cord with minimal damage to the neural tissue are demonstrated. The findings of this thesis are anticipated to aid the studies of the spinal cord circuits and pave way to new directions in flexible fiber-based optoelectronic devices.

Thesis Supervisor: Polina Anikeeva
Title: Professor of Materials Science and Engineering

ACKNOWLEDGEMENTS

I would not be able to complete this degree without the support of many people. First of all, I would like to express my deepest gratitude to my advisor Professor Polina Anikeeva. Professor Polina Anikeeva's knowledge and vision in the field of flexible neural interfaces inspired my research career MIT. Her enthusiasm for research and diligent attitude toward her career have been the driving force for my progress and will continue motivating me for my future career. I would also like to thank my thesis committee members, Professor Yoel Fink, Professor Michael Rubner, and Professor Chet Moritz. Professor Yoel Fink generously supported me by providing access to his facility and by guiding my work; Professor Michacel Rubner provided his support and advice; Professor Chet Moritz offered his resources and insight to help me understand the biological meaning of my projects. In addition to my current advisor and committee members, I would like to thank my previous advisor in University of Illinois at Urbana-Champaign, Professor John Rogers, who admitted me to his group while I was a freshmen in college and opened the door for me to the world of science and engineering. He has always been supportive on my career and will always be my role model.

Special thanks to: Prof. Xiaoting Jia and Andres Canales for teaching me how to fabricate preforms and draw fibers; Prof. Vittorio Caggiano, Dr. Ulrich Froriep, and Dr. Thomas Richner for teaching me how to perform animal surgeries and analyze electrophysiological data. Their assistance and collaboration helped me complete my projects. Also, I would like to thank all of my undergraduate researchers, Imogen Brown (Oxford), Alex Derry, Jeewoo Kang, and Jennifer Selvidge for their diligent work. In addition, I thank all other group members in Anikeeva group and Fink group for their assistance and support: Marc-Joseph Antonini, Ritchie Chen, Michael Christiansen, Junsang Moon, Seongjun Park, Alexander Senko, Dr. Elizabeth Canovic, Dr. Danijela Gregurec, Dr. Mehmet Kanik, Dr. Ryan Koppes, Dr. Siyuan Rao, Dr. Dekel Rosenfeld, Dr. Chong Hou, Dr. Benjamin Grean, Michael Rein, Rodger Yuan, and Dr. Lei Wei.

Many research technicians, teaching staffs, and scientists at MIT Department of Materials Science and Engineering (DMSE), Institute for Solider Nanotechnologies (ISN), and MIT Center for Materials Science and Engineering (CMSE) helped me a lot. I greatly appreciated the trainings and generous help from Michael Tarkanian and Ike Feitler at DMSE, Bill DiNatale at ISN, and Tim McClure and Libby Shaw at CMSE.

I would also like to convey thanks to MIT DMSE, National Science Foundation, and National Institute of Health for providing the financial means needed to conduct this work.

It is a joyful and pleasant journey in the past four and half years in Cambridge. I am thankful to all friends who have gone through this journey with me. Especially, I would like to thank Dr. YiChang Shih for his guidance for career and life and the emotional support. Finally, I am infinitely indebted to my family, especially my parents, Shu-Hwa Tsai and Tsung-Hsien Lu, who always give me unconditional love and support.

Table of Contents

List of Figures and Tables

Chapter I

Introduction

In this chapter, the motivation of investigating neural circuits in the spinal cord and basic anatomy of neurons and neural networks will be introduced (section 1.1), followed by the discussion of state-of-the-art of the technology in neural recording and neural stimulation in the brain and in the spinal cord (section 1.2). Afterwards, how the application of current techniques and the innovation of new materials and architectures can contribute to the investigation of neural circuits in the spinal cord will be discussed (sections 1.3 and 1.4). In the end of the chapter, the hypothesis and proposed approaches to create devices suitable for investigating neural circuits in the spinal cord will be mentioned (section 1.5).

1.1 Investigation of neural circuits in the spinal cord

1.1.1 Motivation

The spinal cord is one of the most delicate organs in our bodies because of its inhomogeneous structure, its fibrous geometry, and its dimension (human: 400 to 500 mm long and 10 to 15 mm in diameter[1]; mouse 110 mm long and 2 to 2.5 mm in diameter[2]). Injury to the spinal cord results in various degrees of paralysis, which can lead to loss of organ function and limb control and cause a debilitating decrease in quality of life[3-6]. In addition, pain associated with spinal cord injury (SCI) can exacerbate the disability for the patients. To treat these debilitating symptoms, scientists need to better understand the nerve regeneration mechanisms[7,8]. These studies, however, are currently limited by the technologies available for monitoring and control of the neural dynamics within the spinal cord. Existing tools do not allow for simultaneous stimulation and recording because the noise from electrical stimulation interferes with the signals of recorded neural activity[9-11]. With the development of optogenetics, which enables optical control of neural activity through the introduction of light-sensitive opsin proteins, simultaneous stimulation and recording becomes possible due to decoupling of the optical and electrical signals[12,13]. While applied extensively in the brain, optogenetic modulation of genetically identifiable neuronal populations in the rodent spinal cord remains challenging due to the lack of flexible devices that can conform to the material properties of this complex organ[14]. Furthermore, repeated spinal cord deformations during normal movement demand the resilience of the implantable devices to bending and extension fatigue. The design and engineering of an optoelectonic device with elastic properties closely matching that of the spinal cord would enable identification of the neural pathways crucial for recovery following spinal cord injury[14-16].

1.1.2 Neural circuits in the spinal cord

Before starting to investigate the neural circuits in the spinal cord, one first needs to understand the basic components (neurons) of the neural circuits and what roles they play. Similar to transistors, neurons never operate alone; they are organized into circuits and process information in groups rather than individually (Figure 1.1)[17]. The human nervous system can be divided into two parts: central nerves system (CNS) and peripheral nerves system (PNS). The CNS includes the brain and the spinal cord, and it is where all of the analysis of information takes places[1,18]. The PNS includes the neurons and parts of neurons found outside of the CNS, which are sensory neurons and motor neurons[18]. Sensory neurons bring signals from the organs into the CNS, and motor neurons carry signals out of the CNS to convey commands to the muscles, the organs, and the glands. In addition to sensory and motor neurons, there are also interneurons which can only be found in the CNS. Interneurons connect one neuron to another by receiving information from other neurons (either sensory neurons or other interneurons) and transmitting information to other neurons (either motor neurons or other interneurons)[18].

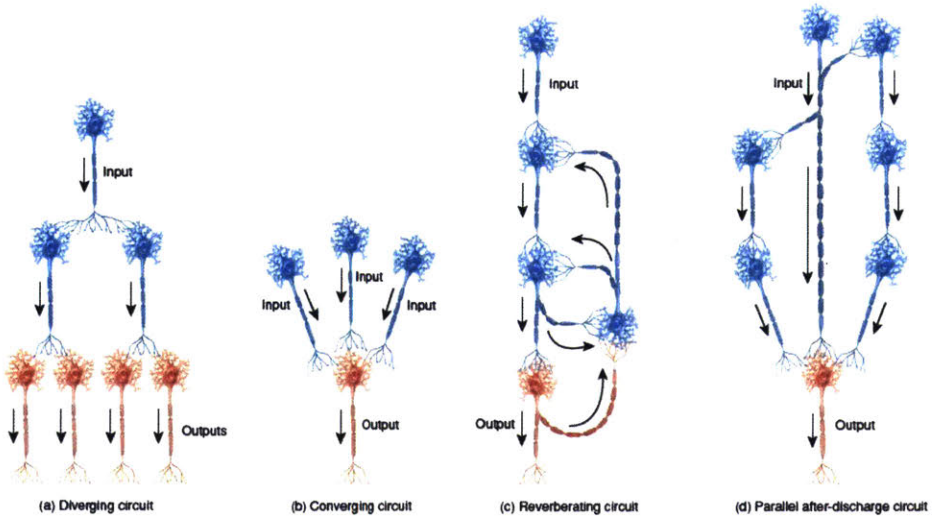

Figure 1.1 Examples of neural circuits
A neural circuit is a functional group of neurons that processes a specific kind of information[17]. (Image taken from ref. 17).

There are three basic functions of neurons: receiving signals (or information), integrating incoming signals (to determine whether or not the information should be passed along), and communicating signals to target cells (other neurons, muscles, or glands). Similar to other cells, neurons have a cell body called the soma (Figure 1.2)[1,18], where the nucleus of the neuron can be found and most neuronal protein syntheses take place. There are various processes (appendages or protrusions) extending from the cell body, including the short, branching processes known as dendrites, and a separate process that is typically longer than the dendrites, known as the axon (Figure 1.2)[1,18]. Receiving and processing incoming information generally take place in the dendrites and cell body. These incoming signals can be either excitatory (tend to make the neuron fire and then generate an electrical impulse) or inhibitory (tend to keep the neuron from firing). If the sum of all of the excitatory signals is sufficient, the neuron ends up firing, and the nerve impulse (or action potential) is conducted down the axon (Figure 1.2)[1,18]. The axon hillock is the axon which arises from the cell body at a specialized area, and in motor neurons and interneurons, it is at where that the action potential is initiated (Figure 1.2)[1,18]. Towards the end, the axon splits up into many branches known as axon terminals (or nerve terminals) and makes connections on target cells[1,18].

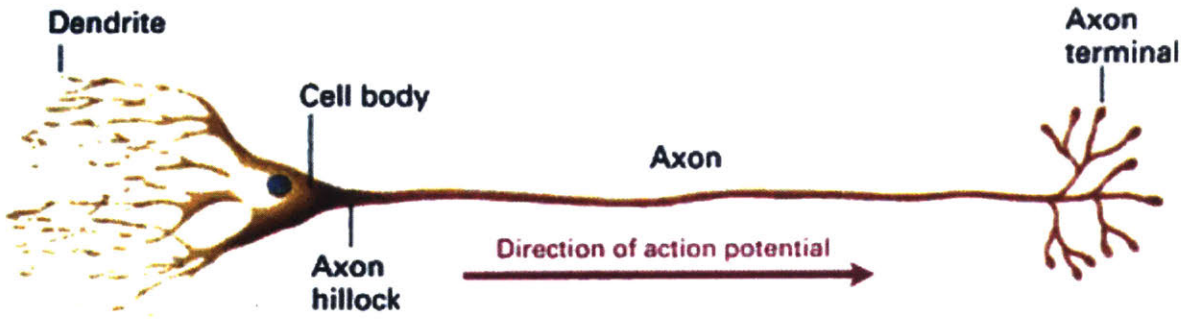

Figure 1.2 Structure of a neuron
A neuron consists of a soma (cell body), dendrites, and axons[18]. (Image taken from ref. 18)

The arrangement and function of neural circuits vary and depending on the synaptic connections (neuron-to-neuron connections), which are comprised of dendrites and axon terminals, and information is transmitted in the form of chemical messengers called neurotransmitters. To understand the function of any circuit, knowing the direction of information flow is important. For instance, nerve cells carrying information toward the CNS are called afferent neurons, and nerve cells carrying information away from the CNS toward the organs are called efferent neurons.

A simple example of a neural circuit is the one that subserves the myotatic (or "knee jerk") spinal reflex (Figure 1.3)[19].

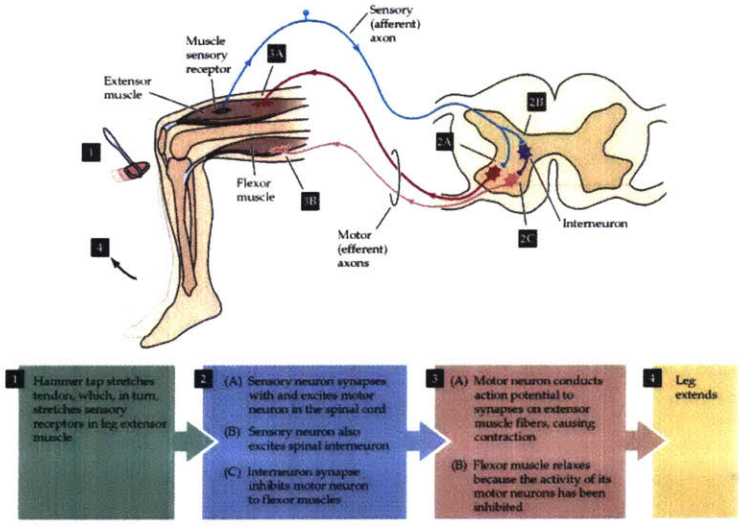

Figure 1.3 Illustration of a simple reflex circuit.
A simple reflex circuit, the knee-jerk response, illustrates several points about the functional organization of neural circuits[19]. (Image taken from ref. 19)

When a knee is hit, the corresponding peripheral nerve terminals are triggered which causes the receptor potentials to trigger action potentials that travel centrally along the afferent axons of sensory neurons. The information stimulates spinal motor neurons through synaptic contacts. Afterwards, the action potentials triggered by the synaptic potential in motor neurons travel peripherally in efferent axons and cause muscle contraction and a behavioral response. One of the purposes of this particular reflex is to help maintain an upright posture in the circumstance of

unexpected changes. This is a case of excitatory synapsis between the sensory afferent neurons and the extensor efferent neurons causing the extensor muscles to contract[19]. In turn, inhibitory synapsis occurs when the interneurons are activated by the afferents and such activation diminishes electrical activity in motor neuron and causes flexor muscles to become less active (Figure 1.4)[19]. Both of excitatory and inhibitory activations are used to control the position of the leg. In this section, the components of the neural circuit and examples were introduced. In the next section, the approaches to investigate the neural circuits will be mentioned.

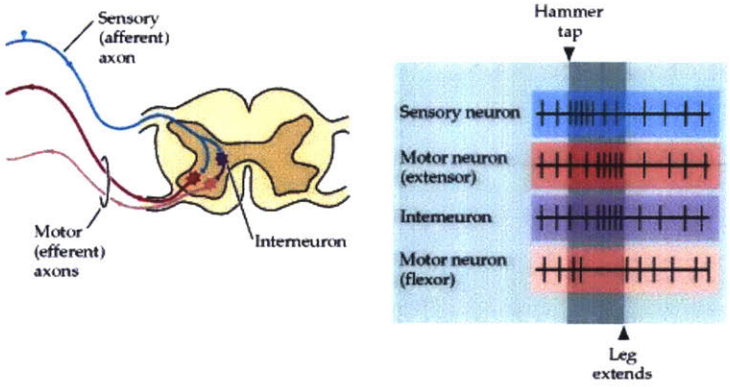

Figure 1.4 Action potentials for different types of neurons in the reflex pathway
Relative frequency of action potentials in different components of the myotatic reflex as the reflex pathway is activated. The differences in frequency and latency provide insight about how this neural circuit processes information[19]. (Image taken from ref. 19)

1.2 Neural recording and stimulation in the central nervous system

1.2.1 Neural recording

Two common approaches to investigating the neural circuits are neural recording and neural stimulation. Neural recording is a means to sense the electrical activity in the nervous system. In the eighteenth century, Luigi Galvani found the first evidence of electrical activity in the nervous system with his studies on dissected frogs[20,21]. He discovered that one can induce a twitch in a leg of dead frog with a spark of electricity. This discovery proved that the nervous system had electrical properties, and since then recording of isolated single neuronal activity (single-unit recording) has become one of the most important approaches to understand the function of the nervous system[21]. There are, in general, three broad classes of neural recording for extracellular *in vivo* recording in the CNS: electroencephalography (EEG), electrocardiography (ECoG), and local field potential (LFP) (Figure 1.5). The first two will be introduced briefly, while the third one will be detailed because of its relevance to this thesis.

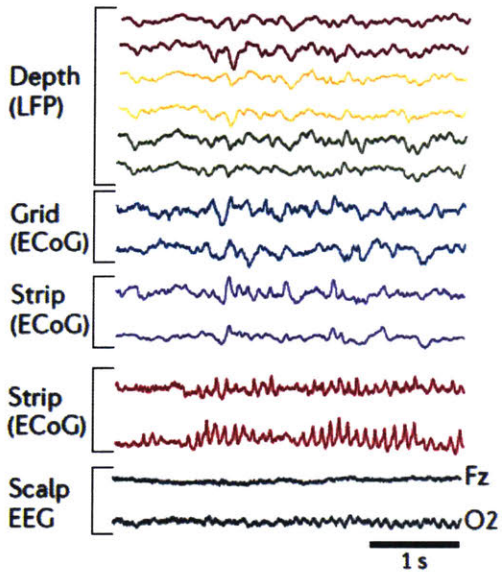

Figure 1.5 Extracellular traces using different recording methods
Simultaneous recordings from three depth electrodes in the left amygdala and hippocampus (measuring the local field potential (LFP)); a 3 × 8 subdural grid electrode array placed over the lateral left temporal cortex (measuring the electrocorticogram (ECoG); two four-contact strips placed under the inferior temporal surface (measuring the ECoG); an eight-contact strip placed over the left orbitofrontal surface (measuring the ECoG); and scalp electroencephalography (EEG) over both hemispheres (selected sites are the Fz and O2) in a patient with drug-resistant epilepsy. The amplitude signals are larger and the higher-frequency patterns have greater resolution at the intracerebral (LFP) and ECoG sites compared to scalp EEG[22]. (Image taken from ref. 22)

1. Electroencephalography (EEG) (Figure 1.5)

This is the least invasive approach and the neural activity is recorded from the scalp[22]. However, the skull (thickness 5.2 ± 0.8 mm)[23] separates the recording device from neurons in the brain, which can potentially lead to low spatial and temporal resolution of recording and limiting its application in neuroprosthetic use[22].

2. Electrocorticogram (ECoG) (Figure 1.5)

With this approach, neural signals are recorded on the surface of the brain, underneath the skull. Since a craniotomy needs to be performed to get these electrodes below the skull, ECoG electrodes

are more invasive than EEG electrodes and require surgery to implant. However, being underneath the skull allows ECoG to have a higher signal resolution compared to EEG[22].

3. Local field potential (LFP) (Figure 1.5)

To record LFP, small electrodes that can penetrate into the tissue are required[22,24]. LFP offers the highest signal resolution, but it is also the most invasive approach of neural recording. Nevertheless, there is still significant interest in developing the electrodes and signal processing techniques for LFP because monitoring the activity of single neurons *in vivo* is the basis of understanding the mechanisms underlying behavior[24]. LFP, basically, is the lowpass-filtered electrophysiological data reflecting the dynamics of the neural tissues (around 1 mm in diameter) surrounding the electrode [24]. The basic steps for spike sorting include the followings: (i) applying a bandpass filter to the recorded raw data, e.g., frequency between 300 Hz and 3000 Hz, to keep the most useful part of the spectrum for spike sorting; (ii) applying an amplitude threshold to the filtered data; (iii) extracting relevant features of the spike shapes and achieving a dimensionality reduction; (iv) inputting features to a clustering algorithm that performs the classification of the waveforms and associate each cluster to a unit[24]. The waveforms of the firing spikes from each neuron in the vicinity of the recording electrode is unique. It is mainly determined by the morphology of neuronal dendritic tree, the distance and orientation relative to the recording site, the distribution of ionic channels, and the properties of the extracellular medium[25]. The detected spikes are grouped into different clusters based on their shapes in a process known as spike sorting [26]. The unique shape of each spike provides information about identifying the function of a neuron (single-unit), and thus, contributes to the analysis of neural circuits. Unfortunately, not all the signals from LFP recordings can be isolated into single-unit spikes. Some shapes cannot be

separated due to a low signal-to-noise ratio, leading to a cluster associated with multiunit activity which provides less information when analyzing neural circuits (Figure 1.6).

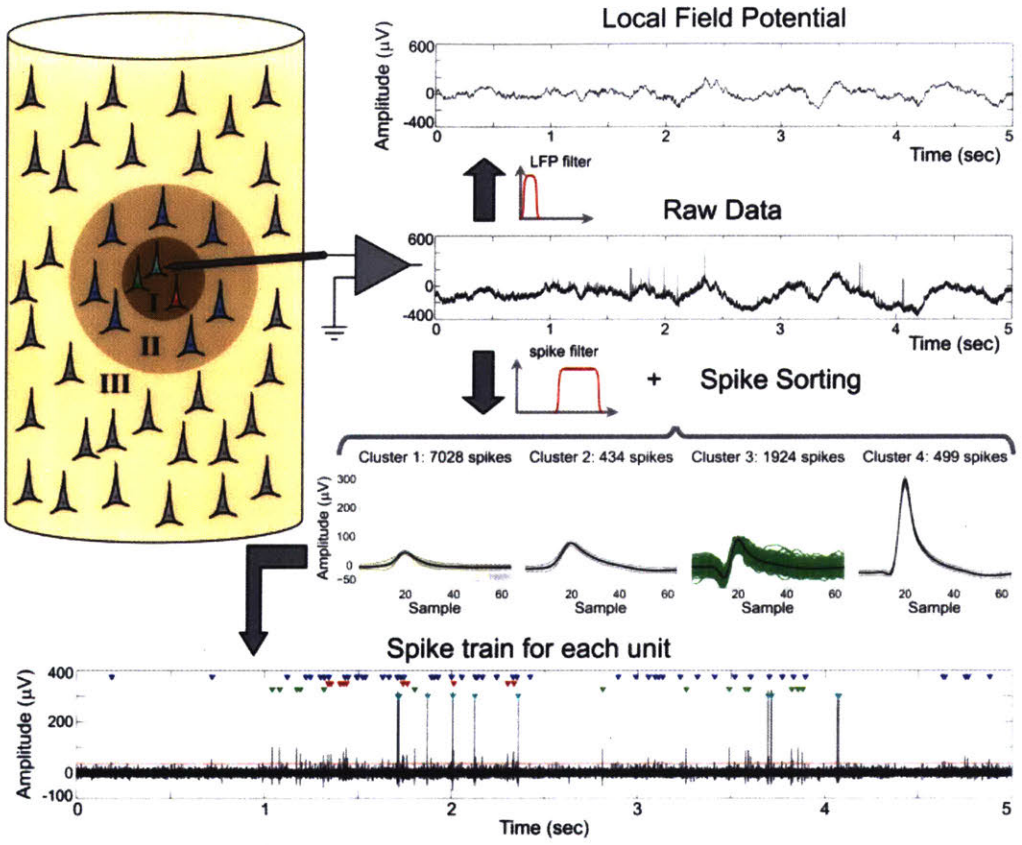

Figure 1.6 Spike sorting process

An example of an extracellular recording (raw data) from the human right entorhinal cortex. The low frequency content (f =1 to 100 Hz) of that signal is associated with the local field potential. Within the higher frequency content (f = 300 to 3000 Hz; black trace in bottom panel) there is a superposition of several effects. Neurons in zone III (distance to the tip of the electrode >140 μm) contribute to the background noise, so their spikes cannot be detected. The neurons in zone II generate spikes larger than the background noise, but they cannot be separated into different units, thus being associated to the multiunit activity (cluster 1). Finally, the neurons in zone I (distance to the tip of the electrode <50 μm) have even larger spikes, and sorting algorithms allow us to assign the recorded spikes to the different neurons that generated them (clusters 2–4), hence the so-called single unit activity. In the bottom panel, the time of occurrence of each spike is marked with a triangle color-coded according to the isolated clusters in each classification[24]. (Image taken from ref. 24).

1.2.2 Neural stimulation

Neural stimulation technology has been used to assist those suffering from Parkinson's diseases and nerve-injury-induced loss of organ function to regain the motor functions, and to relieve the pain associated with the injury to the nerve system. The majority of neural stimulation is performed via electrical means due to the nature of neural activity. Neural activity itself is a change of electrical state; therefore, stimulating neurons can cause excitation or inhibition of action potentials, allowing for manipulation of the nervous system. Clinically, various neurological diseases can be improved via electrical stimulation. Current technologies for electrical neuromodulation include deep brain stimulation, which is used clinically to treat movement disorders such as Parkinson's disease[27]; spinal cord stimulation, which allows management of the chronic neuropathic pain[10,28]; cochlear implants, which have provided partial hearing to more than 324,000 persons worldwide as of 2012[29]; visual prostheses, which can provide some vision to people losing the photoreceptive elements of their retinas[30,31], and cardiac electrostimulation devices (i.e., implanted pacemakers)[32]. However, electrical stimulation[27,33-40] is not the only approach to modulate the state of the nervous system, there are also chemical[41-45], magnetic[46-51], thermal[52-55], or optical[12,13,56-60] approaches. Electrical stimulation and optical stimulation to the CNS will be introduced in detail because the former one is the most commonly used approach and the latter one is the approach of interest in this thesis. Chemical, magnetic, and thermal stimulation of the CNS will be briefly mentioned.

1. Electrical stimulation of the central nervous system:

One of the most commonly used approaches for neuromodulation is electrical stimulation. With electric currents, neural signals can be blocked in order to treat movement disorders or to suppress pain[61]. There are many applications of electrical stimulation of the nervous systems. For example,

deep brain stimulation is a US Food and Drug Administration (FDA)-approved therapy for Parkinson's disease. It has also been used in treating epilepsy, obsessive-compulsive disorder, depression, and etc.[27,33,34] (Figure 1.7A). The electrical stimulation in the brain can be done with surgery and by placing electrodes directly on the targeted regions in the brain (Figure 1.7A).

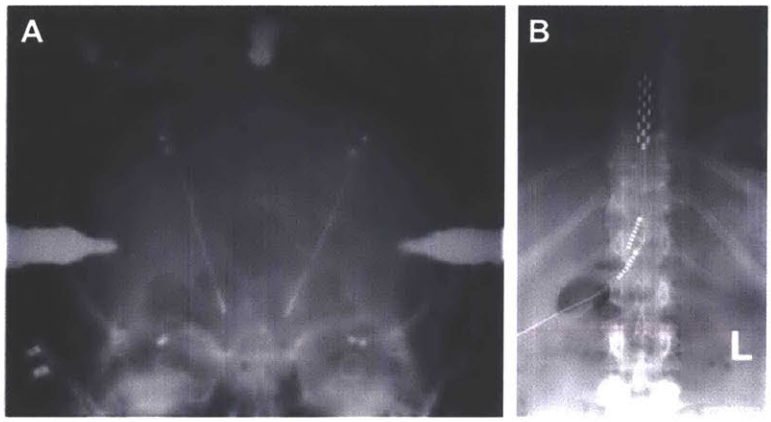

Figure 1.7 Deep brain stimulation and neuromodulation in spinal cord
(A) X-ray image of a brain with metal electrodes implanted for deep brain stimulation[27], and (B) X-ray image of a patient with an implanted spinal cord stimulator[28]. (Images taken from ref. 27 and 28)

In addition to brain stimulation, neuromodulation of the spinal cord is commonly used to control the pain associated with spinal cord injury. FDA-approved neuromodulation devices (Figure 1.7B) are primarily made by established medical device companies such as Boston Scientific, Medtronic, and Nervo. Around the world, some 14,000 patients undergo spinal cord stimulator implants each year[35]. The implantation of devices can be done by inserting the leads into the epidural space in the spinal cord[62]. Other than pain control, both clinical and laboratory research has shown that combining electrical stimulation and rehabilitation enables those who lose limb function because of SCI to step and perform simple motor tasks again[36-38].

Similar to the CNS, peripheral nerves can also be stimulated electrically. This functional electrical stimulation in peripheral nerves can be used to restore motor function in paralyzed limbs by electrically stimulating specific peripheral nerves[39,40].

The development of electrical stimulation of the CNS has benefited many patients suffering from neurological diseases; however, extracellular electrodes have limited cellular specificity and it is generally impossible to target specific classes of neurons in heterogeneously populated tissues with extracellular electrodes, which leads to side effects. The indiscriminate activation of excitatory neurons, all classes of inhibitory neurons, and fibers of passage in the stimulated area can result in the unintended stimulation of non-targeted regions and even cause damage to non-targeted tissues[63]. For instance, spinal cord stimulation for the treatment of chronic pain[62] fails in many patients for reasons that are not fully understood[64], which is in part due to nonselective nature of electrical stimulation[65].

2. Chemical stimulation:

Chemical stimulation is accomplished by delivering chemical substance to the neurons and using a chemical reaction to modulate the neural activity. The methods for chemical stimulation in the CNS can be divided into two categories: systemic and local delivery. Systemic delivery is a route of administration of medication into the circulatory system so that the entire body is affected. Common examples for systemic delivery include oral administration, intravenous injection, and intraperitoneal injection. Systemic delivery approaches are often preferred due to ease of administration. However, systemic delivery may result in suboptimal drug concentration being achieved in the CNS, and lead to erroneous conclusions regarding agent efficacy[44]. Local drug delivery methods are more invasive, but may be necessary to achieve therapeutic drug levels in the CNS. For example, anesthesia can be performed through intrathecal administration, where drugs are delivered directly into the cerebrospinal fluid by injection into the subarachnoid space of the spinal cord in order to bypass the blood-brain barrier[45]. Chemical stimulation of the CNS does not always require the use of neural interfaces and can therefore be non-invasive. However,

invasive neural interfaces are available for chemical stimulation and are typically used in combination with other functionalities, such as recording, to enable readout of the effects of the drug on neuronal function[41-43].

3. Magnetic stimulation:

Neural stimulation can also be accomplished by using induction to modulate neural activity. Transcranial magnetic stimulation (TMS) enables noninvasive neural modulation whereby short pulses of high amplitude magnetic field (typically a few Tesla) is applied through the skull to induce neural activity in a specific cortical area[46-49]. TMS it is an established neurophysiological tool to examine the integrity of the fast-conducting corticomotor pathways in a wide range of diseases associated with motor dysfunction[49]. This includes but is not limited to patients with multiple sclerosis, amyotrophic lateral sclerosis, stroke, movement disorders, disorders affecting the spinal cord, facial and other cranial nerves[49]. In addition, repetitive transcranial magnetic stimulation (rTMS) is a FDA-approved treatment for depression[50,51]. During TMS, a magnetic coil is positioned on one side of the patient's scalp, through which produces a series of strong magnetic pulses that are similar in strength to those produced during a magnetic resonance imaging (MRI) scan are delivered to an appropriate cortical region identified by a physician. It is a painless procedure so no anesthesia is needed. The most common side effects of the treatment include a mild to moderate headache, scalp pain below where the coil placement was positioned, and in some cases, patients may experience from ringing in the ears from the noise associated with this treatment[51]. The most serious risk of TMS is a seizure, but this is rare, occuring in fewer than 1 person in 1,000[46,50,51].

4. Thermal stimulation:

In addition to magnetic stimulation, thermal stimulation is an alternative approach for non-invasive neural modulation. Heat can be introduced by alternating magnetic fields[53], or light[54,55] to activate neurons in the CNS. One of the examples of thermal stimulation of the CNS is infrared neural stimulation (INS), which allows the direct stimulation of neurons with infrared light (wavelength 1.84-1.94 μm)[55,66,67]. There are many advantages over traditional electrical stimulation, including greater spatial resolution[55], no artefact on recording electrodes [68], no gene modification required[69,70]. However, the mechanism of infrared stimulation has been a mystery, hindering its path to the clinic. In some cases, INS appear to be mediated by water absorption of the laser light causing rapid localized heating[68], which drives a transient change in the membrane capacitance[54] and may activate the transient receptor potential cation channel subfamily vanilloid receptor (TRPV 1, 2, 3, and 4, types of ion channel proteins that can not only be activated by osmotic, mechanical and chemical cues, but also responds to thermal changes)[71,72].

5. Optical stimulation:

While the majority of neuromodulation in the past few decades has been based on electrical stimulation, the emergence of optogenetics[12] – a technique that enables optical control of neural activity– in 2005 has provided new research areas in the development of techniques and applications for neuromodulation. Optogenetics is a method in which cells are genetically modified to be sensitive to light with specific wavelengths. In recent years, this approach has been largely used in neuroscience to excite or inhibit neural activity on demand[13,56,57,59,60]. A most commonly used optogenetic tool is channelrhodopsin (ChR2), which is a rather non-specific, single-component cation channel that has a binding moiety for all-trans retinal, a chromophore that renders the channel sensitive to blue light (Figure 1.8)[73-75].

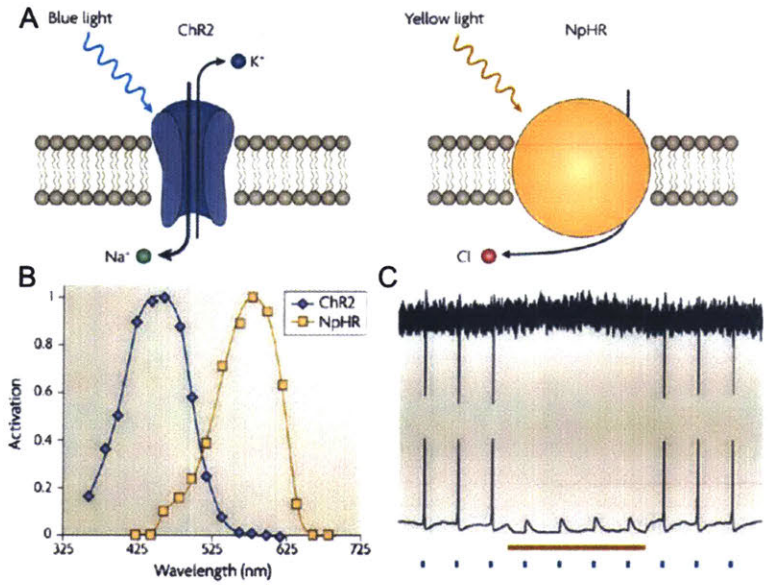

Figure 1.8 Mechanism of optogenetic tools
(A) Schematic of channelrhodopsin-2 (ChR2, left) and the halorhodopsin (NpHR, right) pump. Following illumination with blue light (wavelength ~473 nm), ChR2 allows the entry of cations into the cell. NpHR is activated by yellow light illumination (wavelength ~580 nm) and allows the entry of Cl- anions. (B) Action spectra for ChR2 and NpHR. The excitation maxima for ChR2 and NpHR are separated by approx100 nm, making it possible to activate each opsin independently with light. (C) Cell-attached (top) and whole-cell current-clamp (bottom) traces from hippocampal neurons showing all-optical neural activation and inhibition. Blue pulses represent the blue light flashes used to drive ChR2-mediated activation and the yellow bar denotes NpHR-mediated inactivation[75]. (Image taken from ref. 73)

When ChR2 incorporates into the membranes and expressed in neurons, this channel opens and selectively allows cation exchange through the neuronal membrane upon illumination with blue light, leading to a depolarization of the neurons and the firing of action potentials. While ChR2 is a commonly used optogenetic tool to excite neural activity, light-gated ion pump halorhodopsin (NpHR) is an inhibitory counterpart isolated from the bacteria *Natronomonas pharaoni* (Figure 1.8)[75,76]. NpHR uses the energy of yellow light to move chloride ions into the cell, overcoming the membrane potential (Figure 1.8)[75,76]. In addition of ChR2 and NpHR, neuroscientists have been developing different types of optogenetic tools with various characteristics (absorption spectra, photocycle dynamics, intracellular targeting) (Figure 1.9)[57].

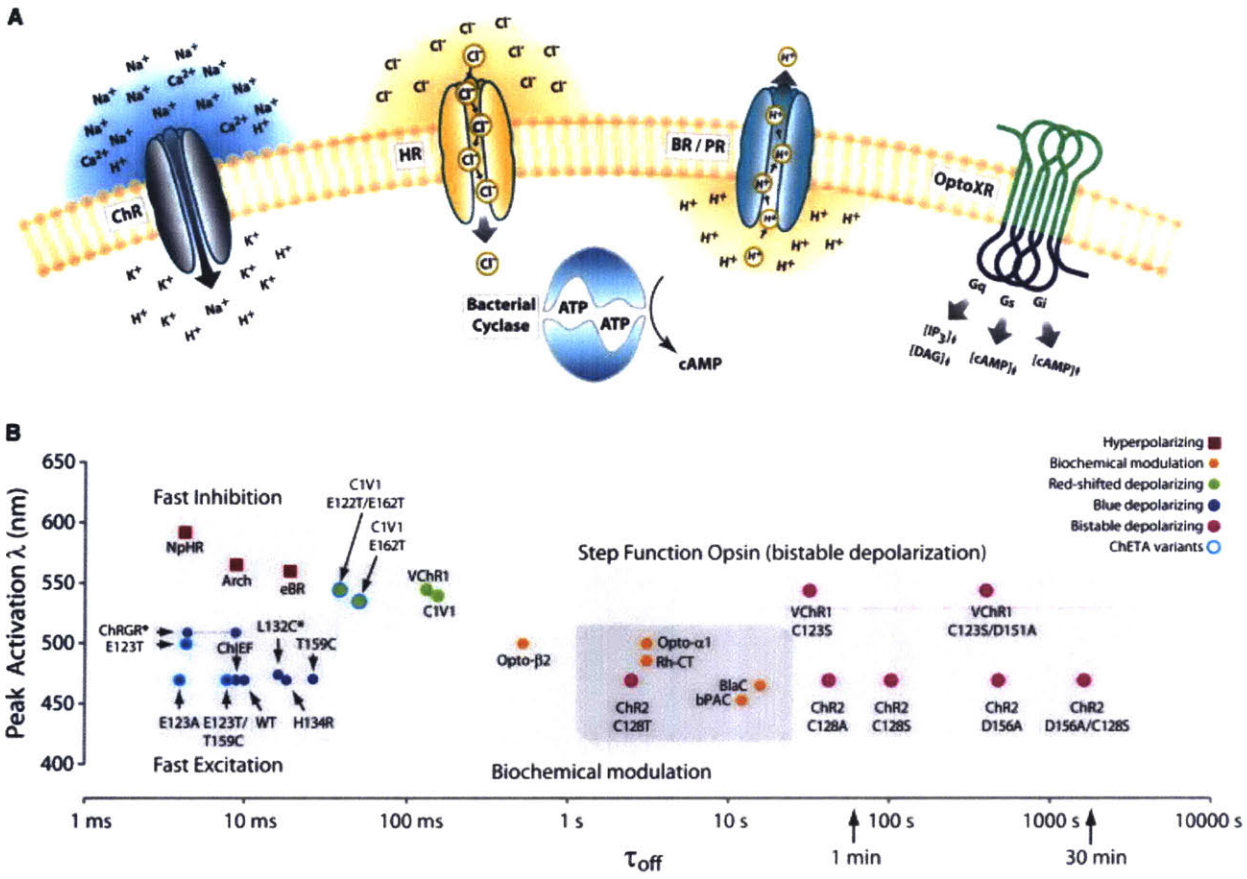

Figure 1.9 Basic properties of known single-component optogenetic tools
(A) Single-component optogenetic tool families with their transported ions and signaling pathways indicated. (B) Kinetic and spectral attributes of optogenetic tool variants for which both of these properties have been reported and for which minimal activity in the dark is observed[57]. (Image taken from ref. 57)

1.3 Materials and devices for neural interfaces

In this section, the development of neural interfaces will be introduced; especially, the needs of the neuroscience community, the development of probes, and the limitations of currently available bidirectional neural interfaces.

1.3.1 Materials and devices for neural recording

Neuroscientists have reached a number of milestones in the development of neural recording interfaces in the past century:

- 1888: Santiago Ramón y Cajal described the structure of the nervous system and concept of neurons (Nobel Prize in Physiology or Medicine , 1906)[77].
- 1928: Edgar Adrian published one of the first recordings of electrical discharges in single nerve fibers (Nobel Prize in Physiology or Medicine , 1932)[78].
- 1950: S. Woldring and M. N. Dirken recorded spike activity from the surface of the cerebral cortex with platinum wires[79].
- 1953: R. M. Dowben and J. E. A Rose developed metal-filled microelectrodes for recording single-unit activity[80].
- 1957: David H. Hubel recorded single-unit activity in the nervous system in cats with tungsten microelectrodes[81].
- 1958: Strumwasser recorded single-unit activity in freely moving squirrels[82] with stainless steel wires.
- 1967: Elwin Marg and John E. Adams published the first record of multi-electrode arrays (MEA) for recording in a single patient for diagnostic and therapeutic brain surgery[83].

- 1986: Invention of multi-channel Michigan probes (Figure 1.10), a silicon planar electrode with multiple recording sites[84-86].
- 1989: Invention of Utah Intracortical Electrode Array (UIEA) (Figure 1.11)[87-92]

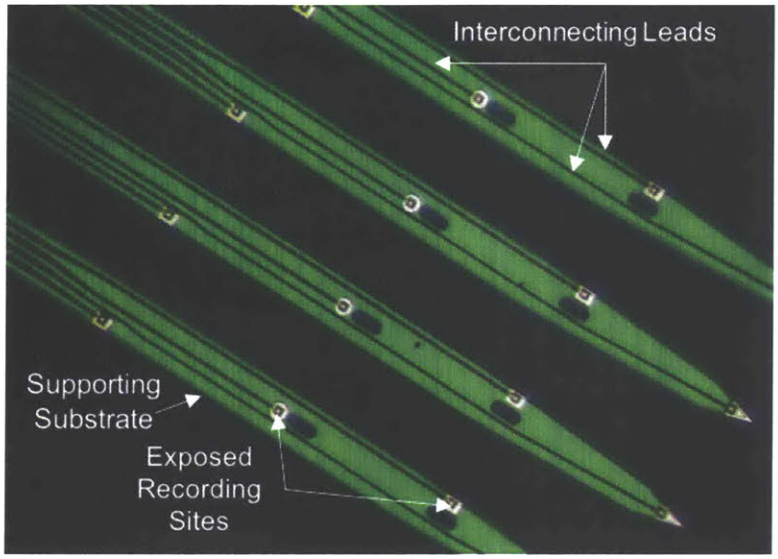

Figure 1.10 Optical image of the Michigan probes
A photo[86] of multi-channel "Michigan Probes" under optical microscope. Thin-film conductors are supported by a micromachined silicon substrate. The entire structure is defined photolithographically with dimensions that are reproducible to within 1 μm[84]. (Inmage modified from ref. 85)

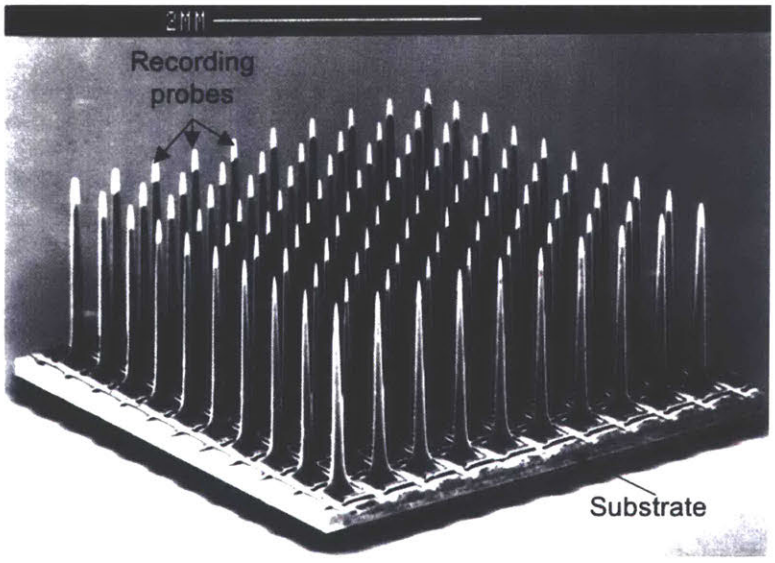

Figure 1.11 Scanning electron (SEM) of the Utah Array
A SEM image of a 10 x 10 probe Utah array developed in University of Utah[92].

From the chronicle listed above, especially over the past 50 years, it can be concluded that the development of neural recording devices has progressed from single electrodes to multi-electrode arrays, and application of these tools has been translated from laboratory to clinical research. However, the key technical challenges enabling long-term implantation remain unsolved. Currently, none of the multi-electrode arrays have been verified to stably and reliably record action potentials over an extended period of time (i.e., several years)[93], and this might stem from the foreign-body response and the encapsulation of devices by glial scars, leading to degradation of signal-to-noise ratio (SNR) of neural recording and decrease in the lifetime of neural interfaces. The foreign-body response is hypothesized to result from initial tissue damage during device insertion[94,95], elastic mismatch between the neural interfaces (GPa) and the surrounding tissues (kPa-MPa) especially in the context of relative micromotion[96-98], disruption of glial networks[99], materials neurotoxicity[100], and chemical mismatch between the implant surface and the cell membranes and extracellular matrix[94]. The challenges emerging from the first two causes of the foreign-body response are especially important when designing neural interfaces for the spinal cord because of its inhomogeneous geometry and relative motions due to daily movements from the implanted subject. Moreover, degradation of materials, delamination of encapsulating layers, and fatigue in the implants are also common issues leading to device failure in the warm, aqueous and saline environments of living subjects[101]. All of these suggest that the design of an interface between the nervous system and a neural probe requires additional materials research.

The interaction between the tissue and the device tethered to the skull or the vertebrae is determined by the bending stiffness (Equation 1. 1) of the material, rather than by its Young's

modulus. The bending stiffness is defined as the force that is required to achieve a certain deflection[101].

$$\frac{F}{d} = \frac{48EI}{L^3} \qquad \text{Equation 1.1}$$

Here, F is the force, d is the deflection, E is Young's modulus, I is the moment of inertia, and L is the length of the device. For a probe with a rectangular cross-section, inputting the expression for the moment of inertia gives:

$$\frac{F}{d} = \frac{4Ewt^3}{L^3} \qquad \text{Equation 1.2,}$$

where w and t are the width and thickness of the device, respectively[101]. For a probe with a circular cross-section, inputting the expression for the moment of inertia gives:

$$\frac{F}{d} = \frac{12E\pi r^4}{L^3} \qquad \text{Equation 1.3,}$$

where r is the radius of the device.

Wires for recording were traditionally made with hard materials such as platinum (Young's modulus, E = 172.4 GPa)[79,102], iridium (E = 528 GPa)[80,102], tungsten (E = 411 GPa)[81,102], stainless steel (E = 189-210 GPa)[103,104], and silicon (E = 113 GPa)[85,89,91,102,105,106]; however, since the stiffness scales cubically (devices with rectangular cross-sections) or to the power of four (devices with circular cross-sections) with the thickness of the material (Equations 1.2 and 1.3), reducing the dimensions of a high-modulus device can dramatically improve its flexibility[107]. Based on this, recently, research on neural interfaces has been focused on the design and the fabrication of devices by taking advantage of compliant microscale wavy surfaces, meshes, serpentines and fibers composed of materials with Young's moduli in the gigapascal range. For example, electronic components can be fabricated with traditional microelectromechanical systems (MEMS) process with thicknesses of a few micrometers and laminated between flexible and/or stretchable polymer encapsulation layers[15,16,108-112]. These hybrid material systems have been developed to address

issues with biocompatibility, mechanical properties, and resolution[113-116]. Nevertheless, recording in the spinal cord has only seen a few demonstrations[117] because of the dramatic mismatch in mechanical properties, the relative motion, and the design challenges due to the fibrous geometry of the spinal cord, and these challenges will be addressed in this thesis.

1.3.2 Bidirectional neural interfaces for the central nervous system

1.3.2.1 Development of bidirectional neural interfaces

To help patients with SCI to fully restore their sensory and motor functions, bidirectional neural devices (i.e., closed-loop sensor-actuator devices) interfacing with nervous systems and organs are required. Unfortunately, simultaneous stimulation and recording in nervous system with a pure electrical device is technically challenging because the current applied during electrical stimulation of neurons introduces noise and prevents artifact-free neural recording[118]. Moreover, electrical stimulation of the nervous system is not selective to a specific groups of neurons (Figure 1.12A), leading to indiscriminate activation/inhibition of all types of neurons[63] (for more information, please refer to 1.2.2 Neural stimulation).

The development of optogenetics a decade ago provided a new solution to create a bidirectional neural interface. Now, the signal from the stimulation (light) is decoupled from the signal from neurons (electricity). Moreover, optical stimulation allows selective manipulation of specific neural populations because it relies on genetic methods to render cells sensitive to a particular wavelength of visible light (Figure 1.9B)[57,119].

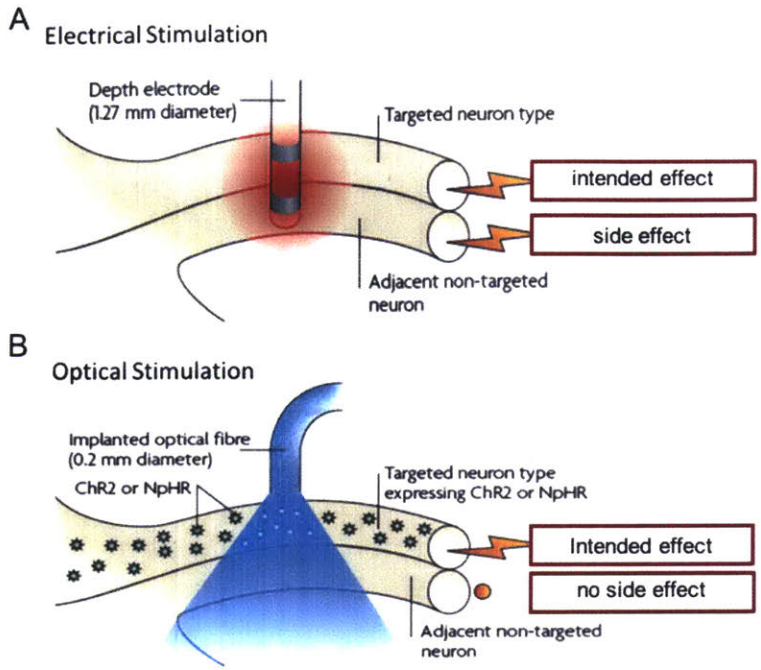

Figure 1.12 Comparison of electrical and optical stimulation in nervous system
(A) An electrode is in contact with nerve cells to conduct electricity for stimulation. (B) Light with specific wavelength is delivered to nerve cells and stimulates neurons selectively[63]. (Image modified form ref. 63)

1.3.2.2 Bidirectional optoelectronic neural interfaces for spinal cord

The introduction of optogenetics has enabled on-demand excitation and inhibition of activity in optically-sensitized neurons with light pulses (Figure 1.9)[12,57,120]. To capitalize on this, closed-loop sensor-actuator devices have been designed by integrating photonic modules into microelectronic neural recording probes[59] to allow simultaneous optical stimulation and neural recording. Traditionally, these probes are combinations of optical fibers with established neural recording technologies such as silicon multielectrode arrays[121,122], multitrodes[123,124] and tetrodes.[125] Recently, microelectromechanical systems (MEMS) and contact printing fabrication methods have allowed for innovative structures with multiple integrated modalities[110,126] (Figure 1.13).

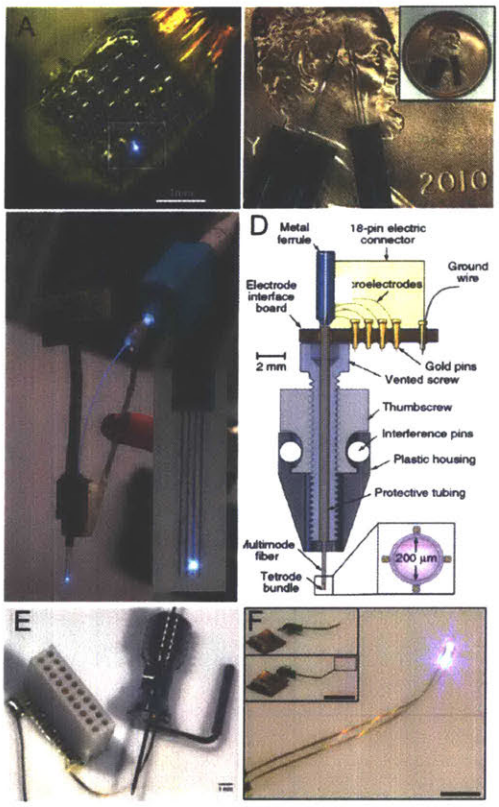

Figure 1.13 Images and schematics of optical probes for neural stimulation
Images of (A) optrode-multielectrode array (optrode-MEA)[122], (B) and (C) multifunctional silicon based neural probes[123,124], (D) schematic of a optetrode[125], and (E) and (F) pictures of polymer-based neural probes[110,126].

These advances in optoelectronic neural probe technologies have helped further investigation of brain circuits and contributed to the development of therapies for neurological disorders[127-129]. While thousands of articles are reporting the use of optogenetics in the brain, only a few studies have explored application of optogenetics in the spinal cord, and even fewer in restoring motor functions[130-137]. Spinal cord neural circuits are complex and heterogeneous and include tissues of vastly different sizes, shapes, stiffness, opacity, and cellular and molecular structure, thereby imposing unique challenges for neural modulation. Moreover, neural structures outside the brain exhibit significant relative motion during movement of the organism[14]. Especially the spinal cord also undergoes meaningful displacement relative to the vertebral column during animal movement, which can result in shear-induced damage in penetrating neural interfaces[14]. Moreover, the spinal cord is highly viscoelastic (elastic modulus of 0.5–1 MPa) and experiences up to ~10% of repeated strain during motion[138,139], making it even more challenging to combine intraspinal neural recording and optical stimulation.

Since the majority of neural probes and light-delivery devices are comprised of hard and brittle materials[93,140,141], the dramatic mismatch in mechanical properties can potentially damage the neural tissue and fail under repeated deformation[142]. Recently, more work has focused on flexible and stretchable probes for optical and electrical stimulation on the surfaces of rodent spinal cords (Figure 1.14)[15,16]. Nevertheless, a highly flexible neural interface allowing simultaneous optical stimulation and neural recording to probe the neural circuits in the spinal cord remains to be demonstrated. In this thesis, flexible and stretchable biomimetic polymer fiber probes are developed with a combined optical core for optogenetic stimulation and conductive electrode(s) for simultaneous neural recording. Fabrication in our studies is so called fiber drawing process, which will be introduced in depth in the next section (1.4).

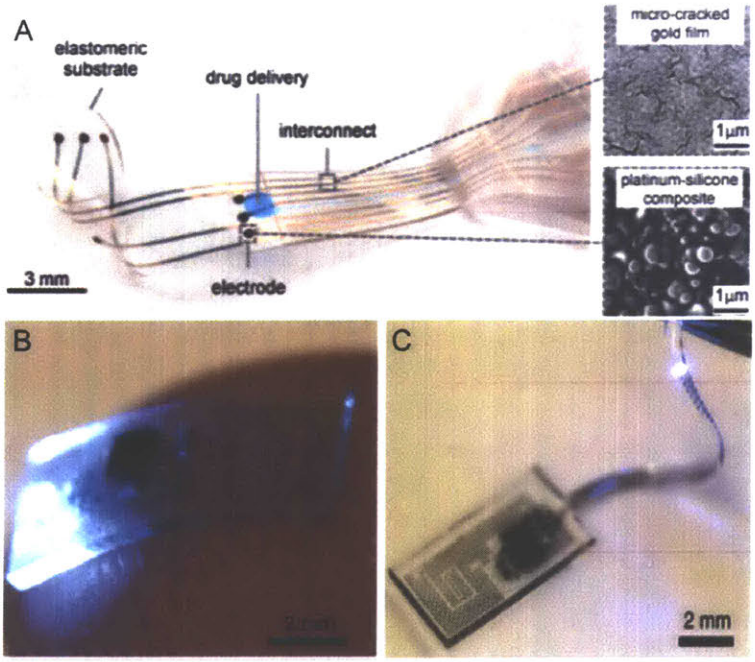

Figure 1.14 Stretchable neural interfaces for stimulation in rodent spinal cord
(A) Electronic dura mater for long-term multimodal neural modulation[15]. (B) and (C) wireless powered LED system for optogenetic neural modulation in mouse spinal cord[16].

1.4 Fiber drawing process

To fabricate the flexible neural probes with integrated waveguides and electrodes, fiber drawing process was used most importantly because it allowed simultaneous processing of multiple materials and the devices yield could be as thin as hair with was very similar to the geometry of nerve fibers. In this section, the background, fabrication process, advantages, and constrains of fiber drawing will be introduced.

1.4.1 Background of fiber drawing

The applications of fiber have been widely integrated into our daily lives for thousands of years. The form of fibers ranges from soft materials such as fabrics for clothes to hard materials such as silica optical fibers for telecommunication [143,144]. With the development of processing methods in the past few decades, fiber can either be created from a single-material and serve simple functionality or be comprised of multiple materials with various optical, electrical, and mechanical properties and functions[43,145,146]. Optical waveguides, electrodes, drug-delivering channels, tissue scaffolds, thermal detectors, chemical sensors, surface-emitting lasers, diodes, and other functional components have been demonstrated as fibers, both single function or multifunction in one fiber [43,145,147-155]. The rules and constraints of fiber fabrication will be discussed in the following sections, but due to their relevance for biomedical applications, fabrication of polymer fibers will be emphasized.

1.4.2 Process

To fabricate a multifunctional fiber, a material set with similar thermomechanical properties (temperature-dependent viscosity and glass transition/ melting temperature) is selected

and then integrated into the preform, which is the macroscale model of the device. Usually, a preform is a cylindrical or a rectangular rod with dimensions of 1.5 inch thick and comprised of different materials, depending on the design and functionality[145]. Assembly of the preform usually requires macroscale machining, film-rolling or film-stacking, followed by consolidation in a vacuum oven or a hot press to eliminate the trapped air between the interfaces. The preform is usually designed to incorporate a thick outer cladding to support the functional components during the drawing. Because the cladding material usually takes up the majority of the preform volume, the processing temperatures during fiber drawing are mainly determined by the glass transition temperature (T_g) of the cladding material. T_g is the transition temperature at which an amorphous polymer goes from the glassy state to the rubber state, or vice versa (Figure 1.15A)[156]. In practice, T_g is not a specific transition temperature but a range of temperatures over where segment mobility changes. This range is of the order of 20 °C for a usual distribution of polymeric molecular weights[156]. At temperature above T_g, the modulus of polymers drop dramatically (Figure 1.15B)[157] and the increase in the mobility of polymer chains (Figure 1.15A) enables the flow[156].

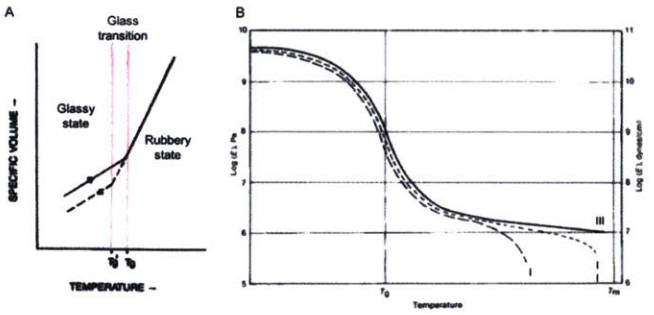

Figure 1.15 The glass transition temperature
(A) As the temperature is decreased in a rubbery polymer, the specific volume decreases linearly until the glass transition temperature is reached. At the glass transition temperature, the rate of change of the specific volume changes as the polymer becomes glassy. The point at which the specific volume changes slope, or the glass transition temperature, is at a higher temperature if the polymer is cooled from the rubber state than if the polymer is heated from the glassy state. The former is marked as T_g and the latter is marked T_g'[156]. (B) Temperature dependence of the modulus, E, of polymers. Examples of idealized behaviors exhibited by an amorphous thermoplastic (I), a semicrystalline thermoplastic (II), and a thermoset (III)[157].

As mentioned in the previous section, consolidation is a process to integrate different materials into a one-piece structure. Deformation is not desirable during the consolidation; therefore, temperature and time should be controlled based on the size, the geometry, and the material properties of each component in the preform[158,159]. The ideal temperature for consolidation is higher than the T_g of all the polymers in the preform but lower than that of the drawing temperature. After a full consolidation at temperature above T_g, all the polymer structures become amorphous and the boundaries of crystalline and amorphous regimes leading to light scattering disappear upon heating[160], as a result, the preform becomes transparent. As for the draw temperature, a rule of thumb to determine it is to look for a point at which all materials flow, i.e. viscosity smaller than 10^6 Pa*s[145].

During the drawing process, the total volume of the preform is critical to sustain a stable draw. Therefore, a sacrificial cladding material can be added on the outermost surface of preform to further reduce the size of functional parts of fibers while maintaining a stable draw. In addition, three main parameters should be controlled well and two parameters should be carefully monitored. The parameters that need to be controlled include the furnace temperature, the feeding speed of the preform, and the draw speed of the fiber (Figure 1.16). These three parameters play critical roles during the drawing process and determine the tension and stress on the preform/fiber. Thus, tension and stress should be always monitored to avoid failure during drawing. The maximum stress each preform can withstand depends on the geometry and the mechanical properties of materials (Figure 1.17)[161,162] in the preform.

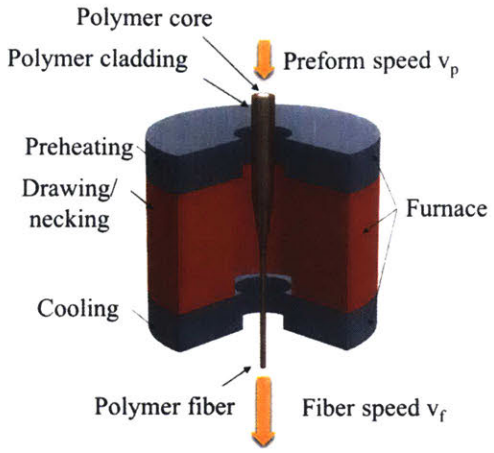

Figure 1.16 Schematic of thermal fiber drawing process
The preform is loaded to the furnace at speed v_p, and pulled at speed v_f. There are three temperature zones. The polymer is first preheated and then deformed at higher temperature. Before exposed to the air, the fiber is cooled in the buffer zone[163]. (Schematic taken fron ref. 164)

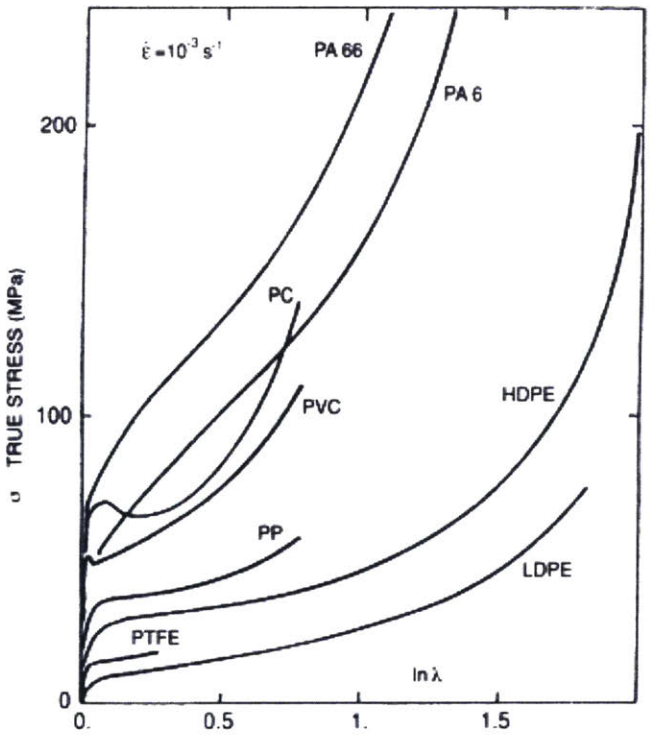

Figure 1.17 True stress-strain curves of different polymers.
PA 6 and 66, polyamides; PC, polycarbonate; PVC, poly(vinyl chloride); PP, polypropylene; HDPE and LDPE, high and low density polyethylene respectively; and PTFE, polytetrafluoroethylene) (Image originally created from ref. 161 and taken from ref. 162)[161,162].

Drawing parameters are generally determined by two rules. First, volume (V_p = volume of the preform, and V_f = volume of the fiber) is conserved. Based on that, the relation between the radius of the preform (r_p), the radius of the fiber (r_f), the feeding speed of the preform (v_p), and the draw speed of the fiber (v_f) can be described as following equation:

$$\Delta V_p = \pi r_p^2 \Delta h_p = \pi r_p^2 \Delta t = \Delta V_f = \pi r_f^2 \Delta h_f = \pi r_f^2 \Delta t \quad \text{(Equation 1.3)}$$

$$\frac{r_p}{r_f} = \sqrt[2]{\frac{v_p}{v_f}} \quad \text{(Equation 1.4)}$$

In Equation 1.3, t is the time of the draw. The ratio between the radius of the preform and the radius of the fiber is described as Equation 1.4, and it is called the draw-down-ratio. The draw-down-ratio can be tuned during the draw by changing the draw speed or the feeding rate; however, the radius does not change to the desired size immediately, but gradually[164]. It takes time for the materials inside the preform to respond to the change, e.g., it takes time for the heat to redistribute and then affect the tension/stress. The second rule relates to temperature. During the draw, all materials must flow, i.e., temperature needs to be set at a point where the viscosities of all the materials are in the range of $10^{2.5}$ to 10^6 Pa*s in order to preserve the structure of the preform within the fiber[163]. Polymers respond to the heat slowly because of their low thermal conductivity (three orders of magnitude lower) compared to metals, consequently buffer zones to preheat the preform and cool the fiber before exposing it to cold air are necessary[164]. Therefore, a 3-zone furnace is used for the experimental setup (Figure 1.16).

1.4.3 Advantages and constrains

There are a few advantages of applying fiber drawing to fabricate multifunctional devices. Fiber drawing not only allows the reduction of cross-sectional areas up to 10,000 times in a single step but also allows high yield and mass production. For our application, a preform (template of device) which is typically 25 to 37.5 mm thick and 300-mm-long cylindrical rod can be turned into ~3 km of fibers with diameter = 265 μm. Moreover, fiber drawing allows for processing of multiple materials in a single-step process, unlike the MEMS fabrication, which usually requires tens to hundreds of steps to fabricate a multifunctional integrated device.

Despite the advantages enumerated in the previous section, there are some limitations and constraints on the material selection. Depending on the desired functionality, the material set we choose may needs to be optically transparent, electrically conductive, flexible, biocompatible, stable in ionic environment, etc. In addition, the viscosity of different materials that need to be co-drawn should be similar at the drawing temperature. Ideally, at the drawing temperature the viscosity of the cladding material should be higher than that of other materials inside preform to support the fiber during the draw and to avoid preform failure.

A wide selection of thermoplastic polymers have been studied and explored for the co-drawing process over the years. High glass-transition temperature (T_g) thermoplastic polymers are mainly used for cladding to support the structure and materials inside because of their thermomechanical properties. For example, thermoplastic polymers such as polycarbonate (PC), cyclic olefin copolymers (COC), polysulfone (PSU), polyphenylsulfone (PPSU), polyetherimide (PEI), and polyether sulfone (PES) are suitable for draw temperatures between 200 – 300 °C, and they are usually used as cladding materials. Other thermoplastic polymers such as polyethylene (PE), poly(methyl methacrylate) (PMMA), thermoplastic polyurethane (TPU), and cyclic olefin

copolymer elastomers (COCE) can also be drawn at 200 – 300 °C, but mostly co-drawn with a cladding material to sustain the structure due to their relatively lower T_g compared to the other group of thermoplastics introduced above. Low-melting-temperature metals and alloys such as tin-based metal alloys can also be included inside the preform and co-drawn with high T_g thermoplastic polymers[43,163].

From the examples stated above, one of the limitations on fiber drawing can be easily observed – the functionality of a fiber is limited by the materials compatible with the drawing temperature. Taking an electrode as an example, it may seem ideal to draw a gold or an iridium electrode because of their high electrical conductivity and biocompatibility but their viscosity at 200 – 300 °C is not low enough to be co-drawn with any known thermoplastic polymers. As a result, conductive polymers or tin alloys which possess lower electrical conductivity are selected as the materials for electrodes instead. Consequently, the task for a materials scientist is to investigate and synthesize various materials with desired functionalities and compatible with designed drawing conditions.

1.5 Hypothesis and proposed approaches

In this work, it is hypothesized that mismatch of mechanical properties between the spinal cord tissue and currently available optoelectronic probes made from metals, metal oxides, and semiconductors limits the application of these optoelectonic probes in the spinal cords and impedes the understanding of the spinal neural circuits. Therefore, in order to study the neural circuits in the spinal cords and to help patients with spinal cord injuries to restore their sensory and motor functions, the first task is to create neural interfaces with mechanical properties matching those of the spinal cords that are suitable for long-term implantation.

To create a bidirectional neural interface capable of performing simultaneous optical stimulation and electrical neural recording, we the proposed to mimic the flexibility and fibrous geometry of the spinal cord and develop a neural fiber probes with integrated optical and electrical components. We anticipate that the closed-loop neural interfaces with functions of optical stimulation and electrical recording can allow neuroscientists to investigate the neural circuits in the spinal cord and to develop next generation prosthetic devices.

Chapter II

All-polymer flexible neural probes

[This chapter is based on Lu et al., Adv. Funct. Mater. 2014[165]]

2.1 Summary

Restoration of motor and sensory functions in paralyzed patients requires the development of tools for simultaneous recording and stimulation of neural activity in the spinal cord. In addition to its complex neurophysiology, the spinal cord presents technical challenges stemming from its flexible fibrous structure and repeated elastic deformation during normal motion. To address these engineering constraints, highly flexible fiber probes, consisting entirely of polymers, are developed for or combined optical stimulation and recording of neural activity. The fabricated fiber probes exhibit low-loss light transmission even under repeated extreme bending deformations. Using the fiber probes, simultaneous recording and optogenetic stimulation of neural activity in the spinal cord of transgenic mice expressing the light sensitive protein channelrhodopsin 2 (ChR2)

is demonstrated. Furthermore, optical stimulation of the spinal cord with the polymer fiber probes induces on-demand limb movements that correlate with electromyographical (EMG) activity.

In this chapter, the design, fabrication, characterization, and *in vivo* application of the all-polymer flexible neural probe will be introduced.

2.2 Material selection

2.2.1 Polymer waveguide

Conventionally, optical waveguides and fibers are made of silica because of its high transmission and low loss (typically at 1550 nm, the absorption minimum in a single-mode silica fiber)[166]. However, only polymer waveguides will be discussed here because of the requirement on flexibility. Polymer waveguides are usually made of high-transmission thermoplastic polymers such as PMMA and PC. SU-8 is also commonly used because it is photopatternable and can be easily integrated by using MEMS processes. In this thesis, PC and COC are chosen because of their high transmission (Figure 2.1)[167], refractive index contrast, and T_g (Table 1). The refractive index contrast provides the numerical aperture (NA, Equation 2.1) of 0.43, and $T_{g,PC}$ and $T_{g,COC}$ are compatible for co-drawing.

$$NA = \sqrt{n_{core}^2 - n_{cladding}^2} \qquad \text{(Equation 2.1).}$$

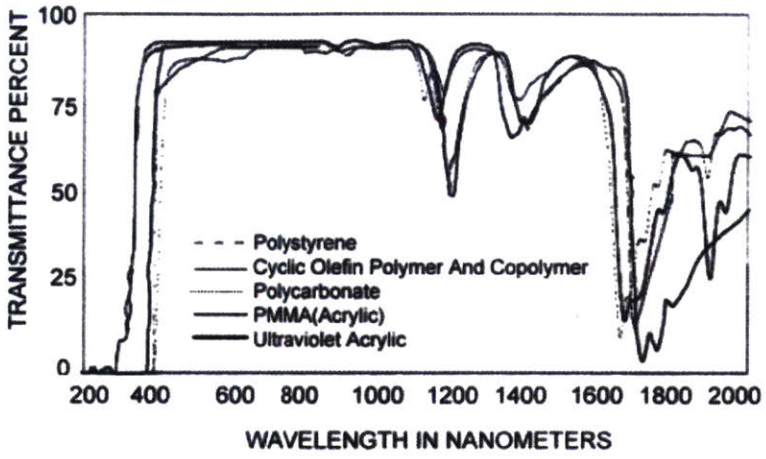

Figure 2.1 Transmission spectra of different polymers
Transmission characteristics of polystyrene, cyclic olefin copolymers, and acrylics[167]. (Image taken from ref. 167)

Materials	T_m or T_g (°C)	Refractive index	Young's modulus (GPa)	Sheet resistance (Ohm/sq)
PC[168]	150	1.586	2.38	--
PMMA[169]	110	1.49	2.2 to 3.8	--
SU-8*[170]	55 to >200	1.596 to 1.67	2.92 to 4.02	--
COC**	158	1.53	3	--
CPE	123	--	--	3×10^3
Silica[171]	1667	1.458	69	--

*All data for SU-8 depends on processing conditions, e.g. baking and curing.

**The COC in this table indicates TOPAS© 6015.

Table 2.1 Chart for material properties
Various material properties for the material selections used in preform fabrication.

2.2.2 Carbon-doped polymer electrode

Traditionally, neural recording electrodes are made of metals such as gold or platinum or heavily doped semiconductors such as silicon[81,84,103,172-174]. However, the big mismatch of mechanical (100 s of GPa for metals and ~100s kPa for tissues[96-98]) properties usually decrease the stability of signal recording over time and cause immune responses from surrounding tissue. To address this issue, polymers provide a convenient design space due to their tunable chemical, mechanical, optical, and electrical properties. Nevertheless, most of polymer is not conductive intrinsically. One of the exceptions is conjugated polymers such as poly(3,4-ethylenedioxythiophene) (PEDOT) and polypyrrole (PPy) which are conductive intrinsically and have already been used for neural recording and other biomedical applications. However, conjugated polymers are not stable at high temperature (degradation, loss of conductivity, etc.)[175,176], which makes them incompatible to be co-drawn with PC and COC. Alternatively, intrinsically insulating polymers can be doped with conductive particles to enable electrical recording/stimulation. Conductive polymer composites can be prepared by dispersing conductive fillers such as carbon black (CB), carbon nanotubes, carbon nanofibers (CNF) or metallic nanoparticles (e.g. gold nanoparticles, silver nanoparticles, and etc.) into thermoplastic polymers[177-183]. The conductivity of polymer composites depends strongly on filler concentration and morphology (e.g. particle size and structure) as well as filler–filler and filler–matrix interactions[181,184-186]. For the all-polymer neural probes, CB-doped polyethylene (CPE, T_m = 120 °C, resistivity $\rho = 3 \times 10^1$ Ω-cm) is used as material for recording electrode in the neural probe (Table1). It is not only conductive but also compatible to other materials (PC and COC) for fiber drawing process (Table 1). It is expected to melt and flow at draw temperatures, but confined and

supported by cladding material (PC). The detailed design and fabrication processes will be introduced in the next section (2.3.1).

2.3 Fabrication and characterization

2.3.1 Fabrication

To fabricate a preform, a polycarbonate (PC) cylinder (diameter = 0.25″, McMaster Carr) is wrapped in cyclic olefin copolymer (COC) sheets (thickness = 0.002″, TOPAS Advanced Polymers, 6014S) until the total diameter of the preform reached 14.8 mm. The entirety is then consolidated at 190 °C for 12 minutes in vacuum. After consolidation, two pockets (L x W x H = 10 mm x 3.53 mm x 4 mm) at symmetrical positions on the surface of the preform are machined and filled with conductive polyethylene slabs (Hillas Packaging, CPE). The entire preform is then tightly wrapped in additional COC and PC sheets until the final outer diameter reaches 32.1 mm to ensure that the preform is thick enough for stable drawing. The final preform is consolidated again at 190 °C for 12 minutes in vacuum (Figures 2.2A and B). The fiber is drawn at 240-245 °C and the size of the preform is reduced by 40–80 times (Figure 2.3). Sacrificial PC cladding was etched away with dichloromethane (Sigma Aldrich) to further reduce the final size of the fiber probes (Figure 2.2C).

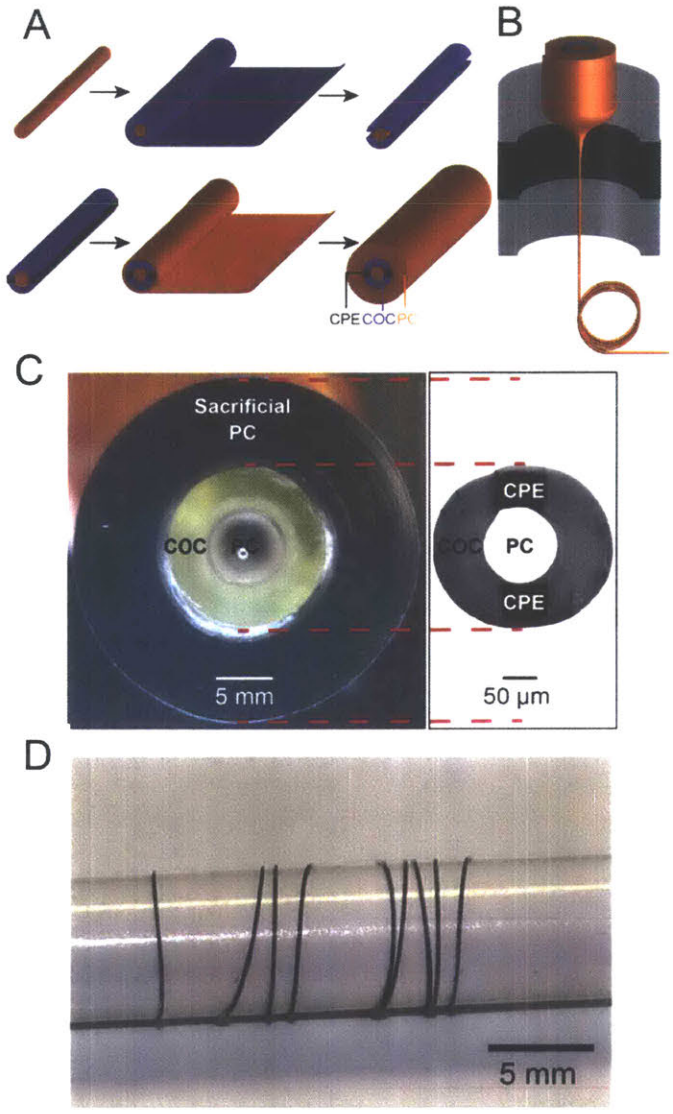

Figure 2.2 Fabrication process of all-polymer neural fiber probes
(A) An illustration of the preform fabrication steps. (B) A schematic showing the drawing of the preform into a fiber by applied heat (C) Left: A photograph of the cross section of the preform comprising the PC core, COC cladding, CPE electrodes and a sacrificial PC layer surrounding the entire structure. Right: A microscope image of the cross-section of the polymer neural probe produced from the preform following the etching of the PC sacrificial layer. The diameter reduction after drawing was 80 times, resulting in 850 m of fiber with a conserved cross section. (D) A photograph of the etched PC/COC/CPE fiber wrapped around a pencil.

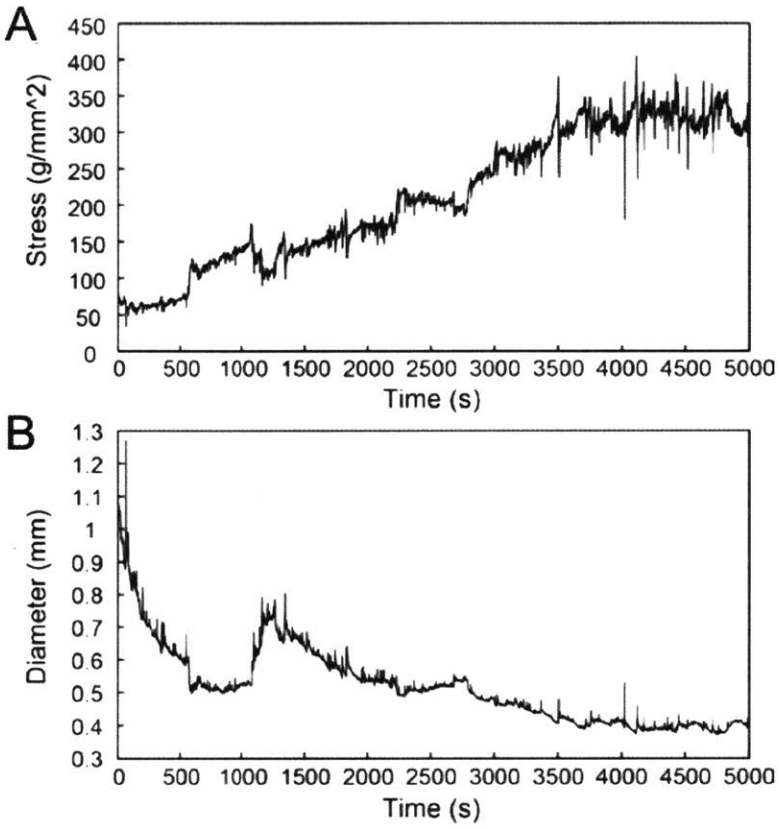

Figure 2.3 Draw data: Tuning fiber diameter by adjusting stress
(A) Stress during drawing process (time period 4000-5000 sec). (B) Diameter of the fiber during the drawing process corresponds to the stress and time period in (A).

To connect the fiber to light source and data acquisition system, the etched fibers are connected to zirconia ferrules (Thorlabs, CF270) using optical epoxy (Thorlabs, F112). The ferrule ends of the fibers are then polished with silicon-carbide sandpaper. The CPE electrodes are exposed by carefully removing the COC cladding, and connected to copper wire using conductive silver paint (SPI Supplies, 04998AB), and then sealed with epoxy (Devcon, 5 Minute® Epoxy). The copper electrode leads are then connected to a 16-channel ZIF connector (Tucker Davis Technologies (TDT)) for electrophysiolocal data acquisition. Prior to implantation, the fiber probes are cleaned with ethanol (diluted with water to 70%) and the connecting points between the ferrule and the probe, and the copper wire and the probe are encapsulated in epoxy (Figure 2.4).

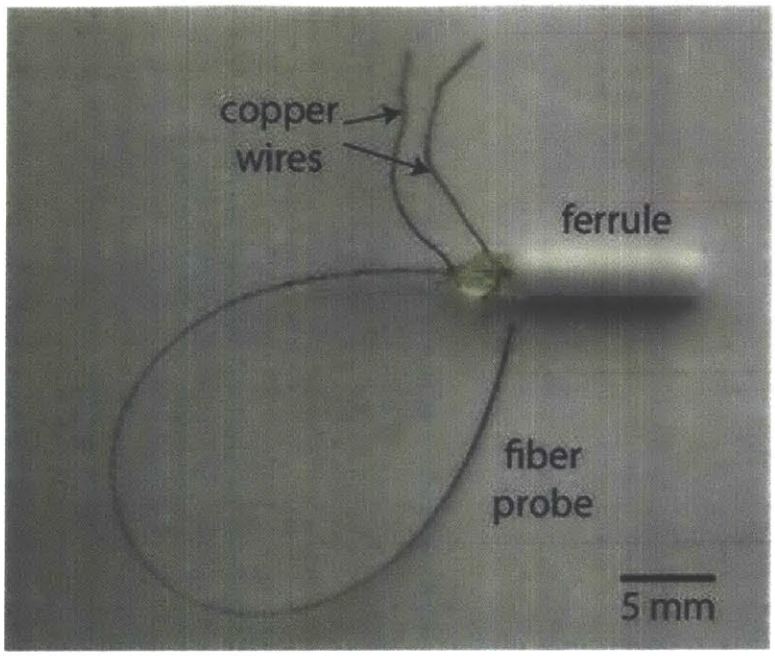

Figure 2.4 Picture of an assembled device
An assembled device connected to a ferrule (for light input) and wires (for electrophysiological recording).

2.3.2 Optical characterization

To ensure the waveguide inside the flexible neural probe is capable of delivering enough light to excite neurons expressing ChR2 (threshold intensity = 1 mW/mm^2)[63], optical characterization is required. Two approaches are used for optical characterization. The optical transmission spectra in the visible range are measured using a broadband spectrometer (Ocean Optics Inc., HR2000CG-UV-NIR) connected to a computer and calibrated with a white light source (Anritsu, MG922A). The transmission spectra of the PC/COC fibers in the visible range are relatively flat and match those of pure PC fibers with similar dimensions, this suggest that the PC/COC fibers can be used to deliver any wavelength of light for the application of optogenetics (Figure 1.9). Introduction of absorptive CPE electrodes lead to a transmission dip at 625–700 nm (Figure 2.5A), but the system is still be able to maintain above 80 % of transmission. In addition to the transmission spectra, the optical loss coefficients (in dB/cm) is accessed by coupling the fibers to a 473 nm blue laser (Laserglow Technologies) via ferrule-to-ferrule connection with zirconia sleeves (Thorlabs, ADAF1) and measuring the output power with a calibrated silicon photodiode (Thorlabs, S121C and PM100D) (Figure 2.5B). The loss coefficient increases from 1.07 ± 0.04 dB/cm in 120 μm core fibers to 2.32 ± 0.12 dB/cm in 65 μm core fibers. For a 90 μm core PC/COC fiber, incorporation of CPE electrodes results in an increase of the loss coefficient from 1.48 ± 0.04 to 2.30 ± 0.02 dB/cm. The latter implies that the optical power densities needed for ChR2-facilitated neural excitation can be easily achieved with commonly available 50–100 mW laser diodes even at fiber probe lengths of >10 cm. The observed optical losses at 473 nm in our bifunctional PC/COC/CPE fiber probes are 3–6 times lower than those of commonly used photopatternable polymer waveguides, such as SU–8 [126,187].

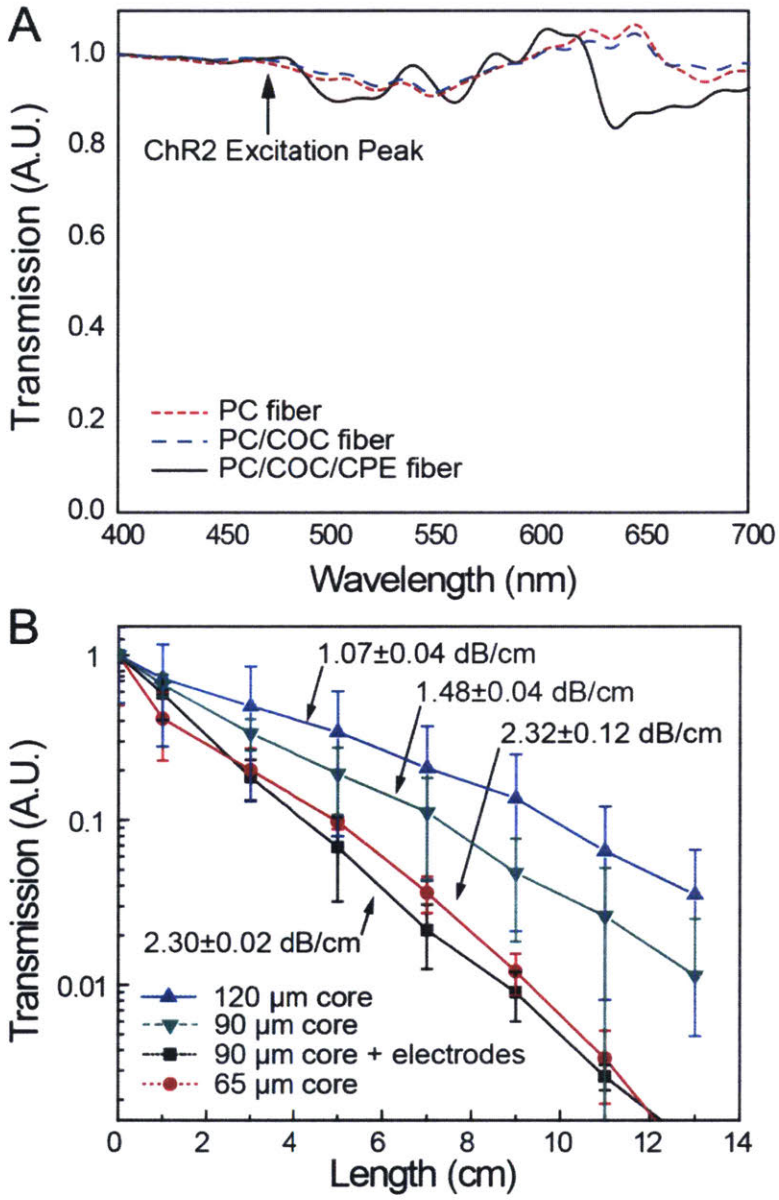

Figure 2.5 Optical characteristics of the fiber probe
(A) Normalized transmission spectra measured in the visible range (400 – 700 nm) for PC and PC/COC fibers. (B) Normalized transmission of PC/COC (core diameters 65 µm, 90 µm and 120 µm) and PC/COC/CPE (core diameter 90 µm) fibers shown for fiber lengths of 0-13 cm. Optical loss coefficients (dB/cm) increase with decreasing core diameter as well as with the incorporation of absorptive CPE electrodes next to the PC core.

2.3.3 Mechanical characterization

Most of the challenges of designing a flexible neural probe for the application in the spinal cord stem from the mismatch of mechanical properties between the neural interface and the tissue and their relative motions[96-98]. Therefore, mechanical characterizations need to be done to quantify how micromotions and bending deformation can impact the performance of the neural fiber probes. To mimic the micromotion induced by mammalian locomotion, respiration, and heartbeat, mechanical tests for the bending stiffness are performed using a dynamic mechanical analyzer (TA Instruments, DMA Q800) in a sinusoidal single cantilever setup with a sample length of 12.7 mm, deflection amplitude of 50 μm, and frequency range of 0.01–10 Hz (Figure 2.6A). The bending stiffness of these polymer fiber probes (diameter 220 μm, length 12.5 mm), measured in a single cantilever setup with 50 μm bending deformation, is an order of magnitude lower than that of a conventional silica fiber with similar diameter and length (240 μm silica fiber with polymer cladding). Silica fibers without polymer cladding rapidly fracture before completing the measurement (results not shown).

In addition to locomotion, larger deformation of the spinal cord can be induced by daily movement of animals such as walking and stretching. Therefore, the performance of fiber probes under mechanical deformation is evaluated. Optical losses at λ = 473 nm are measured at deformation angles of 90° 180°, and 270° with radii of curvature 0.5–15 mm (Figure 2.4B). Tests for light transmission at various bending angles and radii of curvature are performed using a custom machined mold designed to fit fiber probes of diameters of up to 300 μm. Cycling tests are performed by fixing one end of the fiber on a custom-built stage and varying the radii of curvature with a translation stage (Thorlabs, PT3). Approximately 25% transmission is observed at 270° with 0.5 mm radius of curvature, which is impossible with glass fibers. To ensure no degradation

of optical performance occurs under repeated strain during locomotion, a 15-cycle experiment with 180° deformation at 2.5 mm radius of curvature is performed and there is no appreciable decline in performance observed (Figure 2.4C). Consequently, the observed increase in loss during bending deformation (Figure 2.4C) can be solely attributed to an increased scattering and coupling into the cladding rather than to permanent damage to the structure.

The flexibility of the neural fiber probes is capable of functioning under bending; however, bending is not the only type of deformation imposed on the spinal cord, but also stretching. Therefore, it will be ideal to have the neural fiber probe both flexible and stretchable in order to accommodate any kind of movements experiencing by the spinal cord. This will be addressed in the future chapter (Chapter 4).

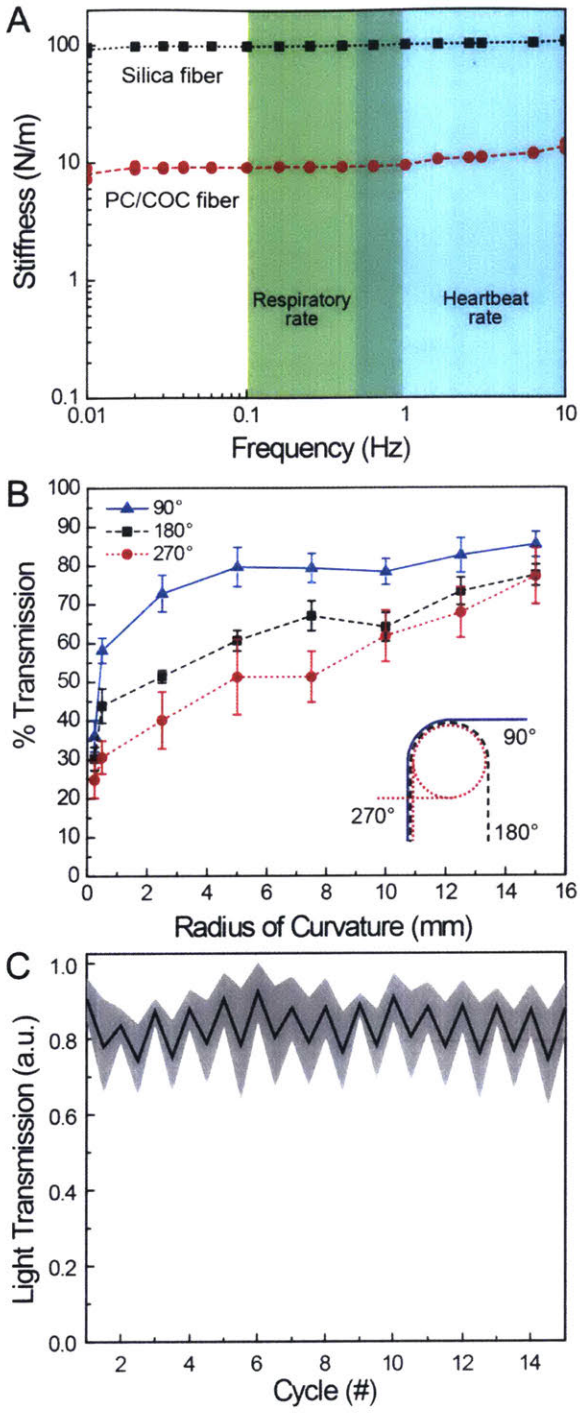

Figure 2.6 Mechanical characteristics of the fiber probe
(A) Bending stiffness of PC/COC and commercially available silica fiber (diameters = 220 and 240 μm, respectively). (B) Relative optical transmission through the PC-COC-CPE fibers at 90°, 180°, 270° deformation with radii of curvature of 0.5-14 mm. Transmission shown as a percentage of optical power transmitted through a deformed device as compared to a straight device. (C) Retained transmission for cycling tests done at 180° angle and radius of curvature = 2.5 mm shows that the optical transmission properties are not affected by repeated stress loading.

2.3.4 Electrical characterization

In addition to light guidance, fiber probes are designed to perform simultaneous electrical recording of neural activity. The quality of neural recording is determined by the noise level, which depends on the electrical impedance. For extracellular recordings, the impedance is determined by the capacitance of the interface between the electrode and the cerebrospinal fluid, which depends on the electrode material and the tip area[101]. To analyze the neural circuits, recording with the highest degree of spatial specificity (i.e., at the level of individual neurons) is required. This can be accomplishing using high impedance (several hundreds of kΩ to a few MΩ) electrodes[188]. Tip impedances of CPE electrodes are measured in saline solution (0.9 wt %) with an LCR meter (Agilent 4284A) (10 mV) in a frequency range of 0.1 to 1000 kHz

Impedance spectroscopy in a frequency range of 0.1-1000 kHz (Figure 2.7A) showed that CPE electrodes inside the fiber probes exhibit impedance values of 28.68 ±5.11 MΩ at 1000 Hz (the frequency range most useful for recording of neuronal activity) and the impedance of the electrodes only has small dependence on the length (Figure 2.7 B); these values are in the upper limit of the range commonly cited for neural probes[93,189,190].

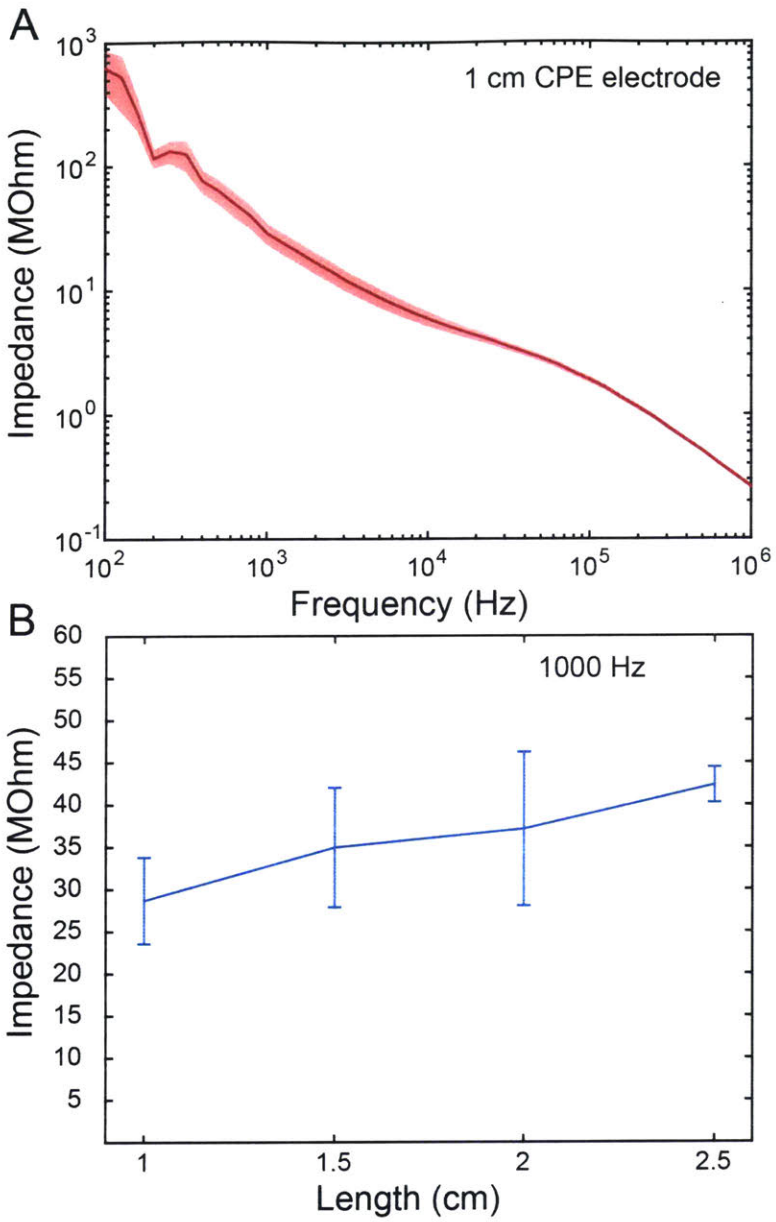

Figure 2.7 Impedance spectrum and characterization of embedded CPE electrode
(A) Impedance spectrum of 1-cm PC/COC/CPE fiber probes (10 Hz – 10 kHz) shown as a mean (line) and the standard error of the mean (s.e.m., shaded area). (B) Impedance of electrodes with length 1-2.5 cm and constant cross section area, measured at 1 kHz shown as a mean (line) and s.e.m. (error bars).

2.4 *Iv vivo* study in the spinal cord

2.4.1 Simultaneous optical stimulation and neural recording

In this section, the detailed implantation procedure and setups of optical stimulation and neural recording will be discussed. All procedures involving animals are approved by the MIT Committee on Animal Care. Male Thy1-ChR2-YFP mice expressing ChR2 fused to the yellow fluorescent protein (YFP) across the excitatory nervous system[191], which includes spinal cords (Figure 2.8) are used for the tests.

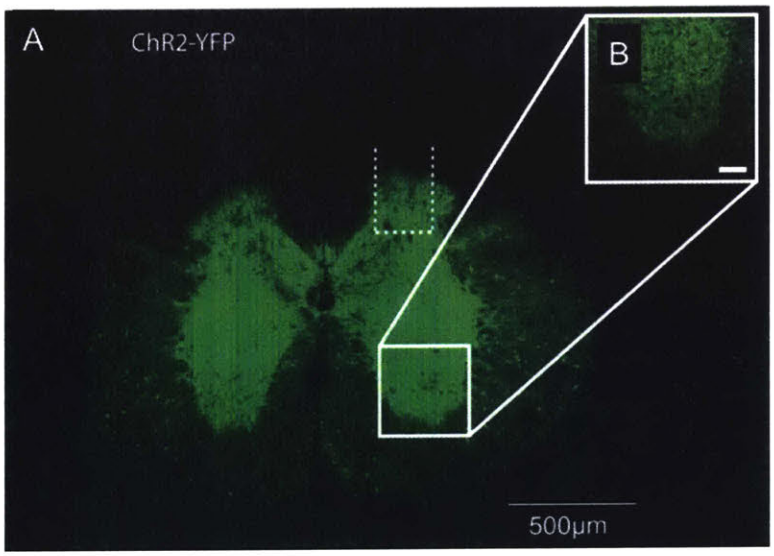

Figure 2.8 ChR2-YFP expressing neurons in the lumbar spinal cord
(A) Transverse section of the lumber spinal cord from a Thy1-ChR2-YFP mouse demonstrating the insertion location of a 200 μm diameter fiber probe, 300 μm deep into the right proximal section of the cord (indicated by dashed lines). (B) Close-up image of the ventral horn indicates robust ChR2-YFP expression (scale bar = 100 μm).
*Method for histology: Two Thy1-ChR2-YFP mice are sacrificed by intraperitoneal injection of pentobarbital sodium and transcardially perfused with 4% paraformaldehyde. Spinal cords are removed and post-fixed for 24 hrs at 4°C. Cords are embedded in 5% agarose (wt% in water) and sliced (50 μm) transversely on a vibratome (Leica). Slices are mounted on superfrost slides and imaged with a Laser Scanning Confocal Microscope (Olympus Fluoview FV100).

The mice are generously donated by Guoping Feng, MIT, and housed at the MIT central animal facility (12h light/dark cycle, 22 °C, food and water *ad libitum*). Before the implantation, setups for optics and electrophysiology should be ready. First, a 473 nm laser (Laserglow Technologies) is coupled into a 2 m-long multimode silica fiber (50 μm diameter, Thorlabs, FG050UGA) "extension cord" and then coupled to the flexible neural probe via a ferrule-to-ferrule connection with a zirconia sleeve. Connection to the RZ5D recording system is established via a PZ2-32 headstage with a ZIF-clip attached to a Headstage-To-Acute-Probe Adapter (TDT). A stainless-steel wire (Goodfellow, FE245840) is used as ground wire while a channel without apparent electrophysiological signals is used as a secondary reference. Afterwards, a flexible neural probe is then placed in a device holder for the stereotactic frame, followed by the implantation surgery.

The implantation procedures are:

1. The day before surgery, hair above the lumbar region (around the hump on the back of the mouse) the spinal cord is removed using depilatory cream (120 seconds in duration, removed using cotton swabs and warm water).
2. Intraperitoneal (IP) injection of the anesthetic agent (Ketamine 100 mg/kg and xylazine 10 mg/kg IP). Alternatively, a nose cone will be positioned and inhalable anesthesia will be applied (isoflurane 1-1.5% in oxygen). The mouse was also injected with slow release buprenorphine analgesia if it was for a chronic experiment.
3. During all surgical procedures, pedal withdrawal reflex is evaluated at least every 20 minutes. Respiratory rate and character are monitored. If IP injection is chosen and the initial dose of anesthesia is not sufficient anymore, a nose cone will be positioned and inhalable anesthesia will be applied (isoflurane 1-1.5% in oxygen).
4. Eye lubricant is placed on the animal's eyes to avoid drying.

5. A heating pad is used to maintain the body temperature. In order to prevent possible burns, a tissue pad will be placed between the animal and the pad.
6. Preparation of the skin: three repetitions of betadine wipe followed by ethanol wipe of the mouse's spine.
7. Pre-operative analgesia (per suggestion of veterinarian): Injection of 0.25% Bupivacaine (1-2 mg/kg) under the skin on the spine where incisions will take place.
8. Incision of the skin above the lumbar region of the spinal cord (Figure 2.9A)[192].
9. Muscles and fat above T12-L1 will be retracted and the spinal cord will be immobilized using a spinal cord immobilizer (Figure 2.9B)[192].
10. For the exposed vertebrae, a unilateral laminectomy will be performed using sterilized forceps (mice) (Figure 2.9C)[192].
11. Lower the flexible neural probe (fixed on the electrode holder attached to the stereotaxic) down to the surface of the spinal cord with the stereotactic micropositioners, once the flexible neural probe touch the surface of the spinal cord, lower the electrode holder for another 300 μm. Note: the flexible neural probe should not be inserted into the spinal cord.
12. Place the reference electrode under the skin of the mouse.
13. Keep the spinal cord moist with 0.09 % saline buffer during the entire surgery.

Once the flexible neural probe is positioned on the spinal cord of the mouse, simultaneous optical stimulation and neural recording can be started. Stimulation frequencies are controlled using the RZ5D system (10, 100 Hz; 5 ms pulse duration, 1 s trial duration, 5 s inter-trial interval, 20 trials, stimulation power 32 mW/mm^2). Electrophysiological data from the spinal cord is collected via the implanted fiber probe. To sort spikes from the raw data, the signal is filtered (0.3 – 10 kHz) and digitized (~50 kHz sampling frequency)[24]. Data analysis is performed in Matlab using built-

in and custom written functions. To quantify reliable neural stimulation in the spinal cord, a threshold on the recorded signal is applied and peri-stimulus time histograms (PSTH) across 20 trials is calculated (Figure 2.10).

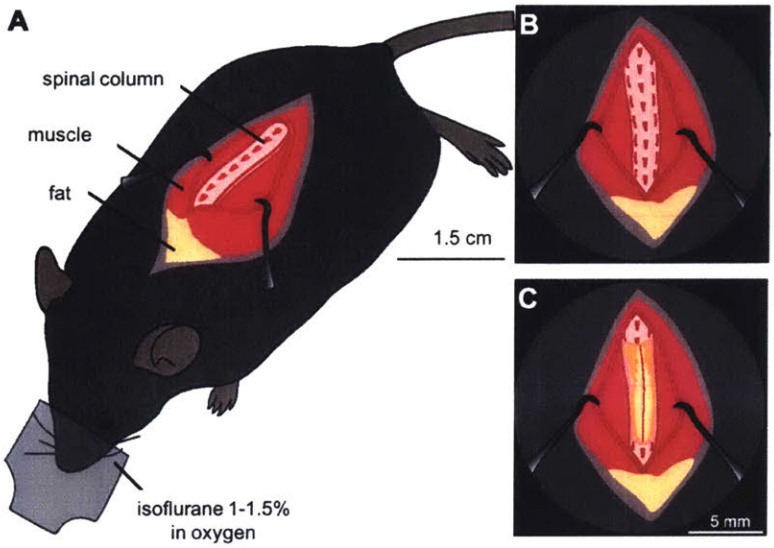

Figure 2.9 Adult mouse spinal cord dissection
(A) An overview of the deeply anesthetized mouse receiving isoflurane in oxygen by a mask. The spinal column is exposed from the dorsal surface by removal of the overlying fat and muscle. (B) Detailed view of the spinal column after removing skin and muscles covering it. (C) Exposed intact spinal cord after performing the partial dorsal laminectomy[192]. (Image modified from ref. 192)

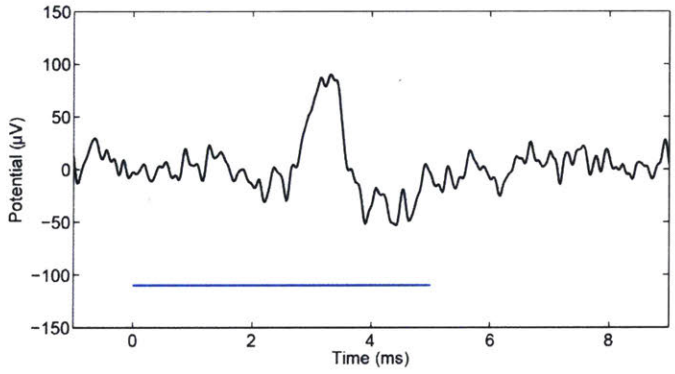

Figure 2.10 A close-up plot for a single light pulse during 10 Hz optical stimulation
A single neural response in the spinal cord evoked by one optical stimulation pulse (wavelength λ = 473 nm, 5 ms pulse width).

During the optical stimulation and neural recording, laser pulses (473 nm, 32 mW/mm^2, 5 ms pulse width, 10 Hz, 1 s epochs, 5 s interval) delivered through the PC core of the fiber probe robustly evoke neural activity in the spinal cord, as recorded with the CPE electrodes integrated within the same device (Figures 2.11A, B and Figures 2.12-2.15). To confirm the physiological nature of the optically evoked activity, stimulation at 100 Hz is preformed (Figures 2.13 & 2.14B), producing initial increase in neural activity, followed by decreased activity without temporal correlation to the laser pulses, consistent with previous reports[125,134]. Furthermore, to control for optoelectronic artifacts that sometimes occur in optogenetic experiments[193], the devices are tested in wild type mice that do not express ChR2, where they show an ability to record neural activity corresponding to sensory stimulation (toe pinch), but do not optically evoke activity (Figure 2.15).

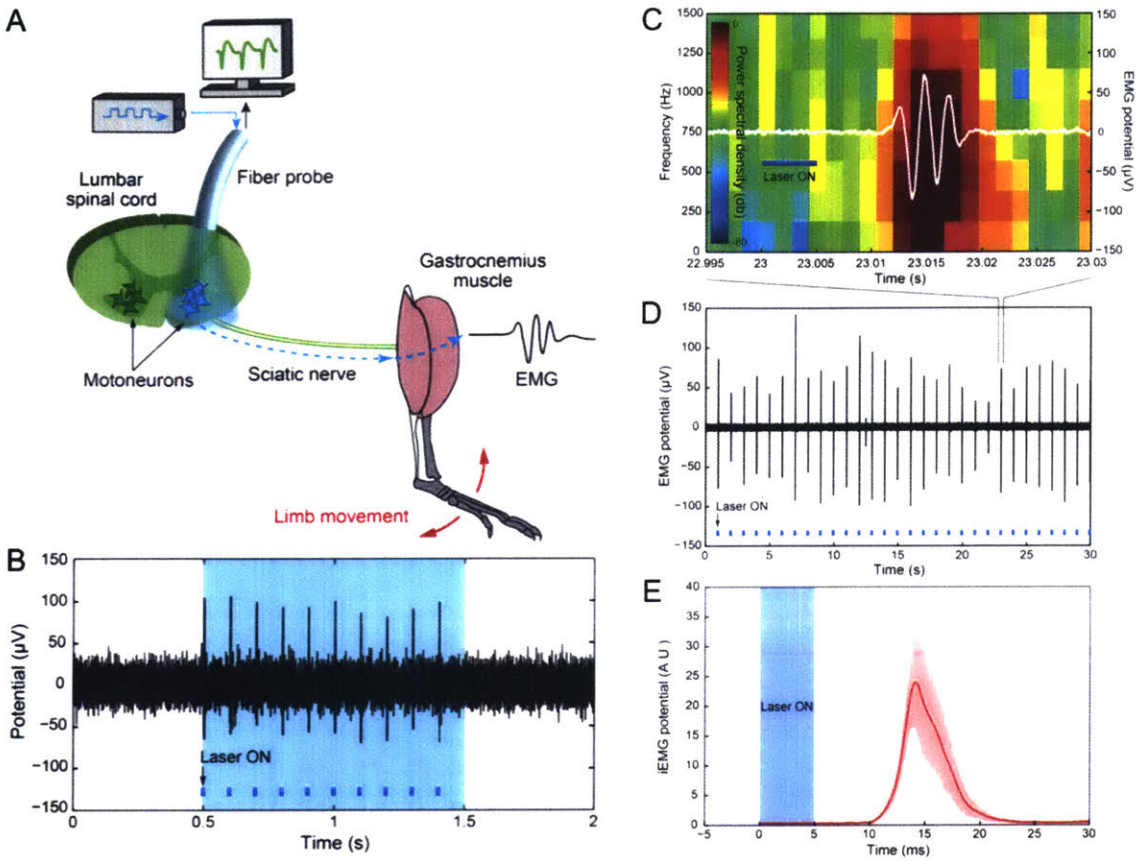

Figure 2.11 Control over spinal cord neural activity and limb movement
(A) Schematic of the experimental setup. Optical stimulation of motoneurons likely activates the gastrocnemius muscle via the sciatic nerve. To quantify the onset of muscle activity, EMG recordings are performed. (B) Neural activity in the spinal cord evoked by 10 Hz optical stimulation (wavelength λ = 473 nm, 5ms pulse width). (C) Example EMG trace (white, right y-axis) closely following the optical stimulus (blue), superimposed on the EMG spectrogram (left y-axis). The signal exhibits a high power up to 1500 Hz. (D) Continuous stimulation at 1 Hz reliably activated the muscle. (E) Integrated EMG (iEMG, n=120 trials, mean (line) ± SD (shaded area)) after filtering (3-3000 Hz) and rectification confirmed the reliability of the muscle activation and accuracy of the EMG recordings.

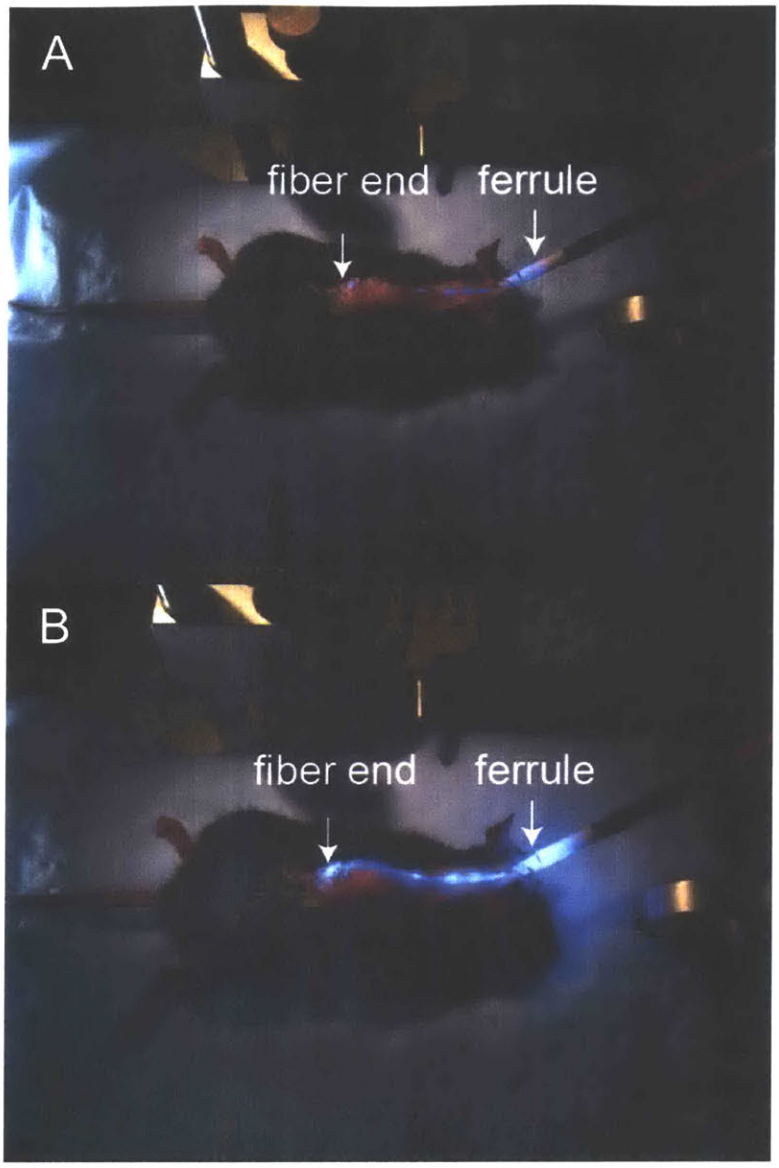

Figure 2.12 Photos illustrating a neural probe acutely implanted in a mouse spinal cord
Fiber probes were fixed at the skull and guided under the skin toward a lumbar spinal cord, where they were bent at 90° towards the cord. (A) Low light image (~100 μW from the source), and (B) Intense light image (~ 10 mW from the source).

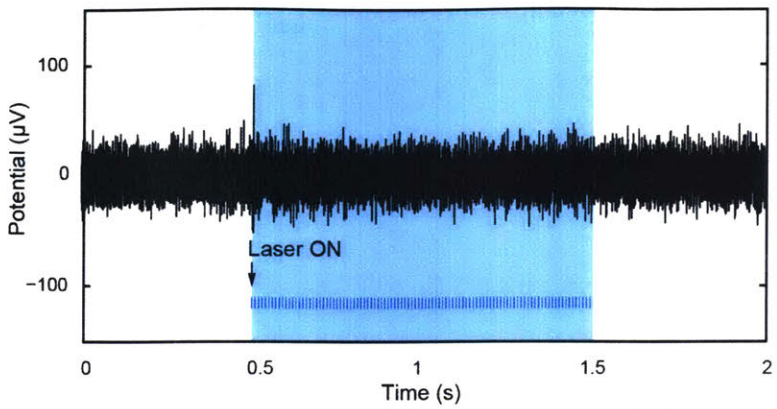

Figure 2.13 Control over neural activity at 100 Hz optical stimulation
Neural activity in the spinal cord evoked by 100 Hz optical stimulation (wavelength λ = 473 nm, 5ms pulse width). Concordant with the ChR2 channel dynamics, stimulation frequencies above 50 Hz resulted in an initial response only, confirming physiological origin of the recorded activity in the spinal cord.

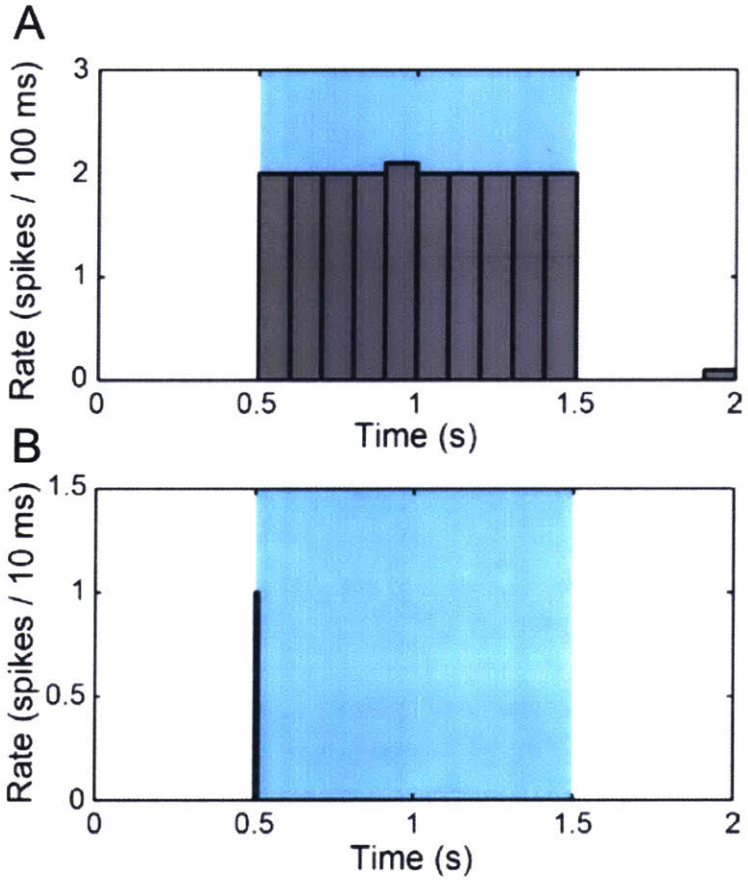

Figure 2.14 PSTH for neural stimulation
A threshold on the recorded signal was applied and peri-stimulus time histograms (PSTH) across 20 trials were calculated to quantify reliable neural stimulation in the spinal cord at (a) 10 Hz and (b) 100 Hz.

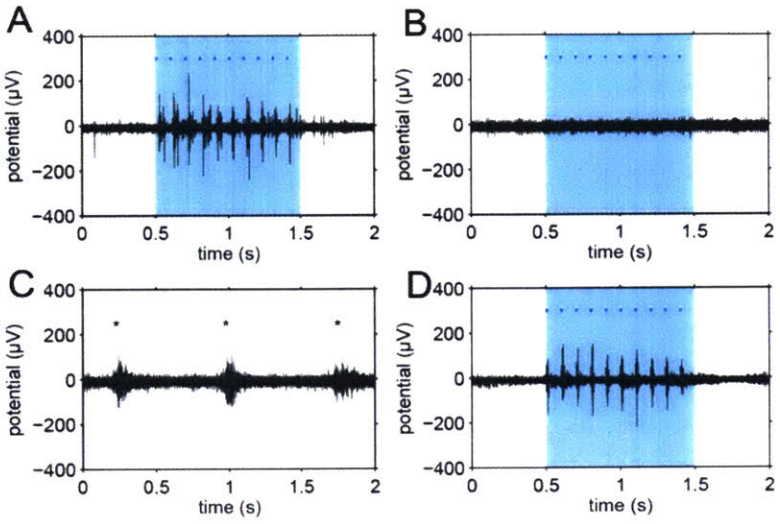

Figure 2.15 Recording and stimulation in Thy1-ChR2-YFP mice and recording in WT mice (A) Stimulation trace in a Thy1-ChR2-YFP mouse with neural activity following laser pulses. (B) Using the same device in a WT mouse laser stimulation does not evoke neural activity, although (C) neural activity can be evoked via toe pinches (asterisks). (D) After replacing the WT mouse with the Thy1-ChR2-YFP mouse, neural activity can still be evoked using laser stimulation, confirming that the probe used was fully functional over the course of the entire experiment.

2.4.2 Light-induced muscle activity

In addition to evoking neural activity, the optical stimulation in the mouse spinal cord can also induce muscle activity. The lumbar region is specifically chosen for optical stimulation because it handles sensory input and motor output coming from and going to the hind limbs[36,194] and creating a neural interface to restore motor function of injured spinal cord is the ultimate goal of this thesis. Optical stimulation has been used to modulate muscle activity[135,137] in mice but none of the previous work has demonstrated simultaneous optical stimulation and neural recording in mouse spinal cord together with light-induced limb control. Optical activation of the lumbar spinal cord circuitry corresponded to hind limb muscle activation indicated by twitches that closely correlated to the laser pulses (Figures 2.11C-E). Based on previous reports, the hypothesis is optical stimulation of the spinal cord leads to firing of motoneuron fibers through the sciatic nerve leading to the recruitment of motor units within the gastrocnemius muscle[137]. To quantify the optically evoked muscle activity we performed EMG recordings during 120 s of 1 Hz optical stimulation with 5 ms pulse width (Figures 2.11C, D). The average envelopes of the EMG waveforms across trials were temporally correlated to laser pulses with a time delay of 10.6±2.3 ms (mean ± s.d.) (Figure 2.11E).

The detailed procedure of measuring muscle activity during optical stimulation is described below. Electromyographical (EMG) recording data is acquired via two stainless steel electrodes (A-M Systems, 0.002"/0.0045" Bare/Coated) inserted into the belly of gastrocnemius muscle (Figure 2.11A) and near the muscle-tendon junction of the Achilles. EMG leads are connected to the PZ2-32 headstage (1 Hz – 10 kHz filter settings, ~50 kHz sampling frequency)[195]. Spectrograms are calculated in Matlab using data sections of 100 data points with an overlap of 25% (Figure 2.11C). Since spectrograms revealed high power up to 1.5 kHz, the signal (3 Hz – 3 kHz, symmetrical 2nd

order Butterworth filter)[195] is filtered and integrated EMGs (iEMG) is calculated by isolating EMG trials, subtracting the mean from each trial, and subjecting the result to a Hilbert transformation to calculate the analytical signal. The real and the imaginary part of the analytical signal are squared, the results summed, and the square root of the sum resulted in the envelope constituting the iEMG (Figure 2.16). The time delay between the laser pulse and the EMG onset is accessed by applying a threshold to the data, and considering the first crossing of that threshold as onset of muscle activity, followed by calculation of mean and SD in Matlab. The threshold is defined as the mean of 'noise' activity (200 ms after one laser pulse to 200 ms before the next pulse) for all trials and adding the corresponding four standard deviations to that value.

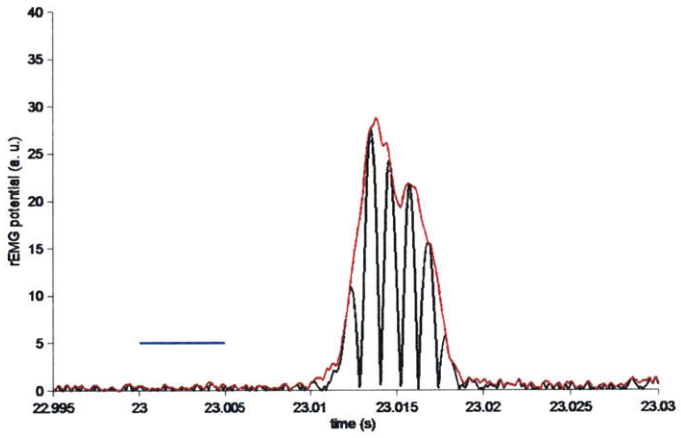

Figure 2.16 Rectified EMG trial with envelope

Rectified EMG (rEMG) trial corresponding to Figure 2.5C. The red line shows the integrated EMG (envelope) of this trial. The envelope was calculated for all trials (Figure 2.11D).

2.5 Conclusions

By applying the fiber drawing process to a material set consisting exclusively of polymers, highly flexible miniature bifunctional neural probes are produced and simultaneous optical stimulation and electrical neural recording in the spinal cord *in vivo* are successfully demonstrated with such probes. The fiber probes exhibit low optical losses and maintain their functionality at deformation angles up to 270°, radii of curvature as small as 500 μm, and following repeated loading. These devices have relatively flat transmission spectra across the visible spectrum, and thus can also be used for optical neural interrogation involving light-sensitive proteins (opsins) with activation spectra in the yellow or green parts of the visible spectrum. The experiments in live mice illustrate the utility of the fiber probes for optical control of motor functions via optogenetic stimulation of the spinal cord, allowing the correlation of evoked neural activity to a behavioral response. Consequently, the all-polymer fiber probes provide a step towards the development of flexible biomimetic optoelectronic neuroprosthetics.

Despite the capability of the all-polymer fiber probes described in the chapter, it does not allow the recording of single-unit activity because of its high impedance, and moreover, there is no *in vivo* test done on freely moving mice. Therefore, the goal the projects described in the next chapters is to address these issues.

Chapter III

Carbon-doped polymer neural probe

3.1 Summary

In Chapter II, CPE strips were embedded into a waveguide (core: polycarbonate (PC), cladding: cyclic olefin copolymers (COC)) to serve as electrodes to measure the neural activity in mouse spinal cord[165]. Albeit improved compared to previous prototypes[43,165], the relatively high impedance of the CPE caused a large noise level of 22.32 ± 2.68 during recording. To improve the noise level, herein, a more conductive polymeric electrode is designed by the addition of carbon nanofibers (CNF) to COC and thermoplastic polyurethane (TPU). Impedance measurement showed that a 10 wt% CNF addition increased the COC conductivity for more than 1000 %. When tested in the mouse brain for neural recording, the noise level was 17.85 ± 1.8530, which is 20 % improvement to the previously introduced CPE electrode.

3.1 Background

3.1.1 Electrodes for single-unit neural recording

To record neural activity, probes with electrode impedances of tens to hundreds of kOhm to a few MOhm are effective[190,196,197]. As shown in Chapter II the impedance of commercially available conductive polyethylene (CPE) electrodes (cross-sectional dimensions of 40 ± 0.2 by $40 \pm 0.2 \mu m^2$) was in the range of tens of MOhm, which only allowed multi-unit recording of neural activity (Figure 2.7). However, one of the objectives of this thesis was to create neural probes for single-unit neural recording in the spinal cord. To obtain single-unit neural recording, it is necessary for the SNR to be 5 or greater[197]. In general, the majority of the noise in single-unit recording arises from the multitude of undifferentiated background action potentials (neural noise)[197]. However, the impedance of an electrode affects the level of noise with higher impedance electrodes causing a lower signal-to-noise ratio[197]. Therefore, the main objective of this chapter was to create low impedance electrodes for single-unit neural recording. The approach used in this chapter is to look for more conductive materials compared to CPE. In the following sections, the design, fabrication, characterization, and *in vivo* test of highly conductive carbon-doped polymer composites will be introduced.

3.1.2 The design of carbon-doped polymer composites

There are two components for the composites – the polymer matrix and the conductive particle. For the polymer matrix, low-temperature COC (T_g = 78°C) and TPU (T_m = 119-139 °C) are selected since their thermomechanical properties are compatible to co-draw with PC. In addition, the high elasticity of TPU (fracture point at 570% strain) as well as its low modulus

(modulus at 50% of elongation E = 1.10 MPa) are reported as favorable properties for implanting in the spinal cord[198].

Carbon nanofibers (CNF) are selected due to their high conductivity. In addition, according to the percolation theory, the high aspect ratio of the CNF[180] minimizes the use of CNF is the electrode composite. The approximate percolation threshold (ϕ_c) of polymer composite is the limit of large aspect ratio (η), based on the excluded volume concept for a statistical distribution of filler particles and can be expressed as the following:

$$\phi_C \approx {}^{1}/_{\eta} \qquad \text{(Equation 3.1)}$$

A typical aspect ratio $\eta \approx 1000$ for CNF reproduces the above mentioned value of 0.1wt%[184]. However, the percolation threshold provides an estimation of when a polymer is transformed from an insulator to a conductor and the effect of doping ratio on the conductivity of the composite needs to be measured[181,184-186,199].

3.2 Electrode design and characterization

3.2.1 Fabrication

CNF (average diameter of 100 nm and length > 10 μm, PR-HT-19, Applied Science) are used as fillers (conductive particles) and added to low T_g COC (Catalog No. 24750-100, Polysciences, Inc.) and TPU (Morthane PS 455-203, Huntsman Polyurethanes) with toluene (Sigma-Aldrich 244511) and dimethyl sulfoxide (DMSO, Sigma-Aldrich D4540) as the respective solvents.

Polymer pellets are dissolved in their solvents (1:10 in volume). CNFs are added to the polymer/solvent mixture for a 0-30 wt.% ratio. The mixture is covered by aluminum foil to avoid

evaporation of solvent (Figure 3.1) and heated at 80°C under agitation overnight until the polymer/solvent mixture becomes a homogeneous solution. The composite is then dried to evaporate excess solvent. The polymer composite is hot-pressed at 180°C under 50 psi for 10 minutes and then cut into stripes with desired sizes (usually 4mm x 4mm x 50mm) with a razor blade.

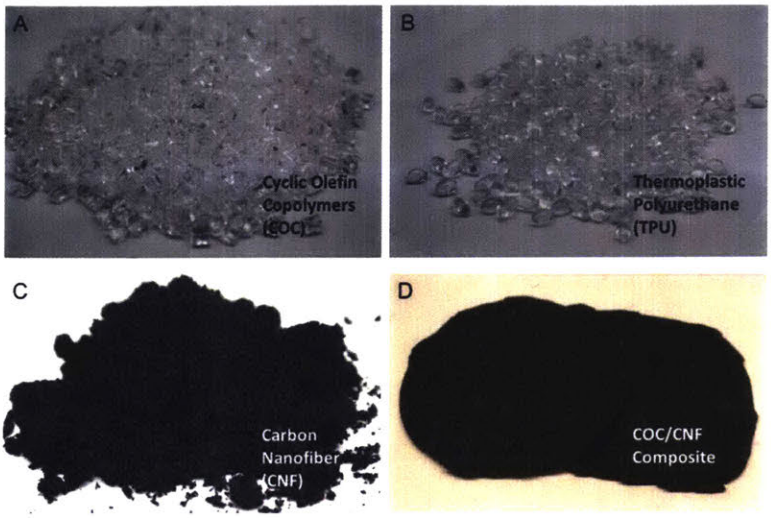

Figure 3.1 Materials for polymer/carbon composites
Images of (A) cyclic olefin copolymer pellets, (B) thermoplastic polyurethane pellets, (C) carbon nanofibers, and (D) COC/CNF composites after processed with hot-press.

3.3.2 Characterization

To assess the electrical property of the synthesized composites, sheet resistance is measured. For both CNF-COC and CNF-TPU, sheet resistance decreases by 6-7 orders of magnitude when the loading percentage of carbon nanofiber exceeds 10 wt% (Figure 3.2). Next, to verify the drawing compatibility of the composites, thermal characterization is perfomred. Thermal gravimetric analysis (TGA) is done to investigate the degradation temperature and the percentage of CNF of the composites at each composition (Figure 3.3). Another thermal characterization is done with differential scanning calorimetry (DSC, Figure 3.4), which is used to measure the T_g of a material. Based on the thermal transition temperatures of CNF-composites ($T_{g,\ CNF\text{-}COC} = 75°C$, and $T_{m,\ CNF\text{-}TPU} = 110°C$) the composites can be drawn with PC ($T_{g,\ PC} = 145\ °C$) (Table 3.1).

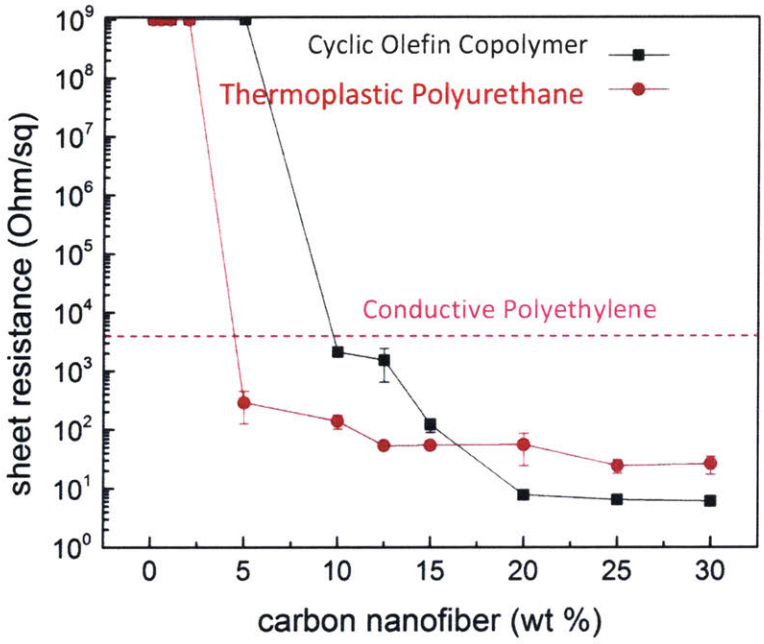

Figure 3.2 Electrical property of carbon-doped polymer composites.
Sheet resistance of different carbon-doped polymer composites as a function of filler loading percentage (wt%).

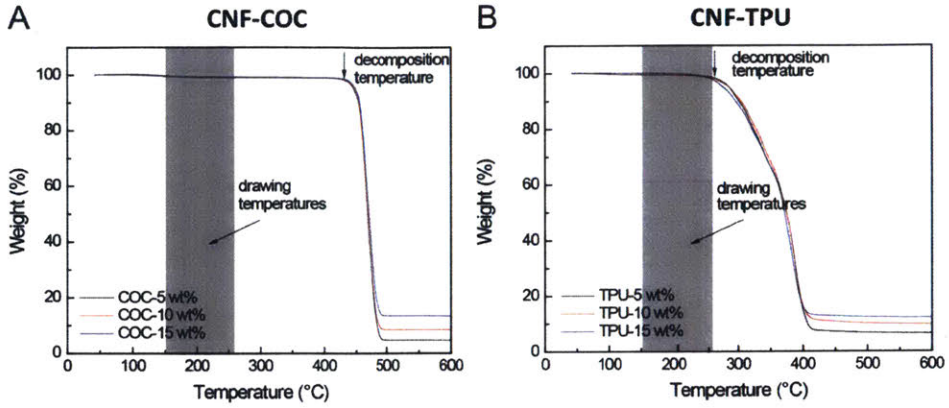

Figure 3.3 Data of thermal gravimetric analysis
Curves of change in weight for (A) CNF-COC composites and (B) CNF-TPU composites with different loading percentage of filler at different temperatures.

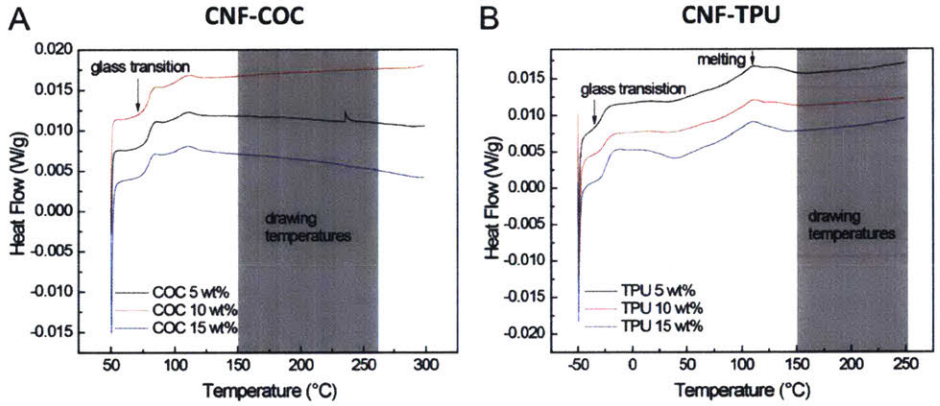

Figure 3.4 Data of differential scanning calorimetry.
Curves of change in heat flow for (A) CNF-COC composites and (B) CNF-TPU composites with different loading percentage of filler at different temperature.

Materials	T_g (°C)	T_m (°C)	Degradation temperature (°C)	Drawing temperature (°C)
CNF-COC 5wt%	75	n/a	430	150-260
CNF-COC 10wt%	75	n/a	430	150-260
CNF-COC 15wt%	75	n/a	430	150-260
CNF-TPU 5wt%	-30	110	250	150-260
CNF-TPU 10wt%	-30	110	250	150-260
CNF-TPU 15wt%	-30	110	250	150-260
PC[200]	145	n/a	n/a	150-260

Table 3.1 Thermal properties of CNF composites and PC.

The design criteria for the CNF composites are to maximize the conductivity while minimize the loading concentration of conductive particles. Therefore, 10 wt% and 15 wt% CNF composition are selected for both CNF-TPU and CNF-COC as the drawing preforms and were machined inside a PC outer cladding (Figure 3.2). When drawn at 245-260 °C, the high loading composites (15wt%) did not flow uniformly and resulted in a non-continuous fiber and fragmented composite sections inside the cladding material. This is possibly due the dramatic change in viscosity caused by the high concentration of CNFs (the viscosity of 15wt% carbon nanotube/PC composite (CNT-PC) is reported to be an order of magnitude higher than that of 5wt% CNT-PC at 260 °C[201]). On the other hand, CNF-TPU (10wt%) and CNF-COC (10wt%) were successfully drawn into continuous fibers; however, only CNF-COC composite is further characterized for impedance and used for *in vivo* study because of the relative stable drawing (Figure 3.5). After drawn into fibers, the impedance spectra of CNF-composites were measured (Figure 3.6). The impedance of CNF-COC electrodes (cross section size 40±4 x40±4 μm^2) were about 700 kOhm at 1000 Hz (Figure 3.5), which is lower than that of CPE electrodes with comparable size and in below 1MOhn.

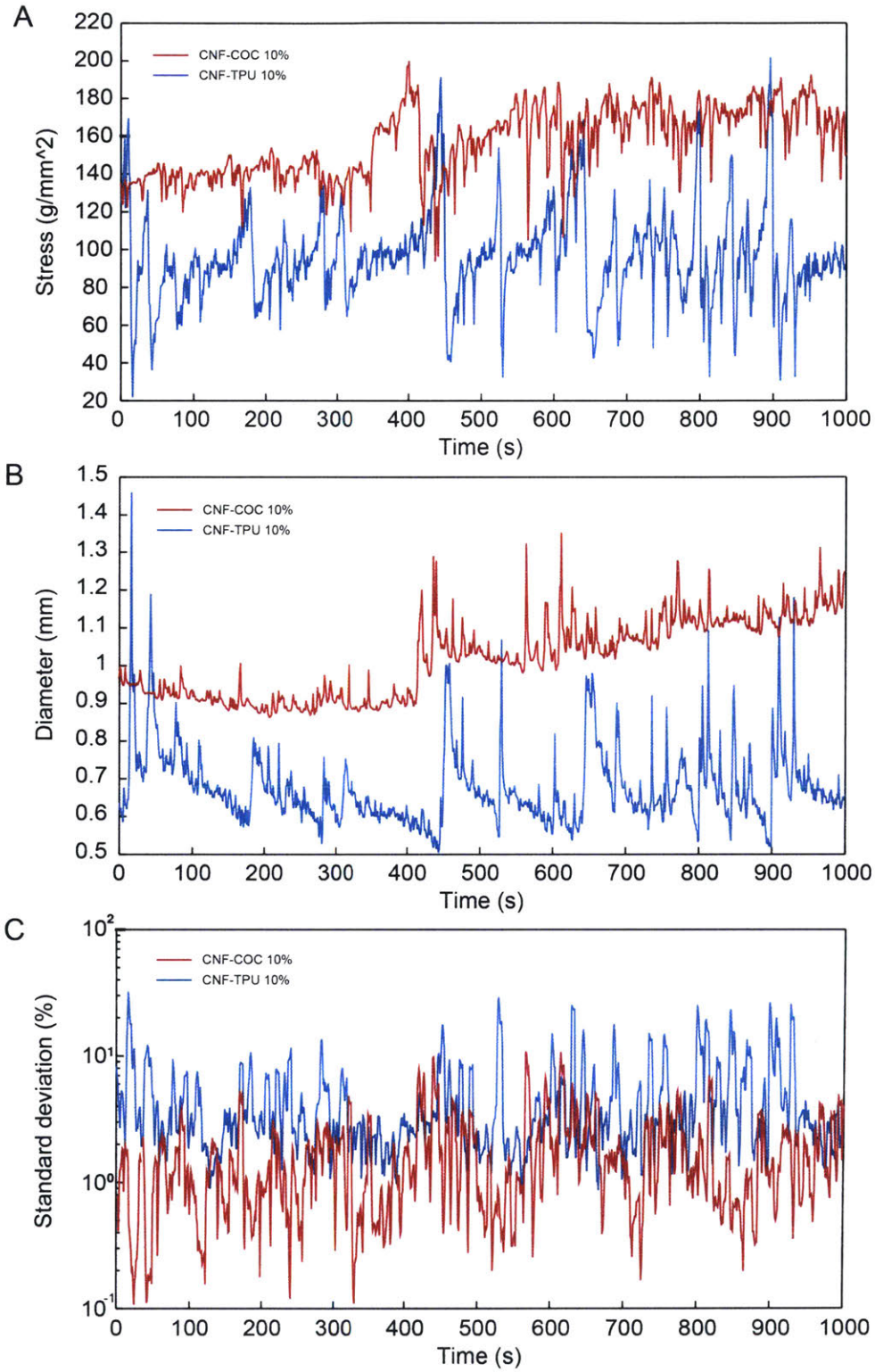

Figure 3.5 Draw data of CNF composites

(A) Stress during drawing process (time is normalized). (B) and (C) Diameter and standard deviation of diameter of the fiber during the drawing process corresponds to the stress and time period in (A).

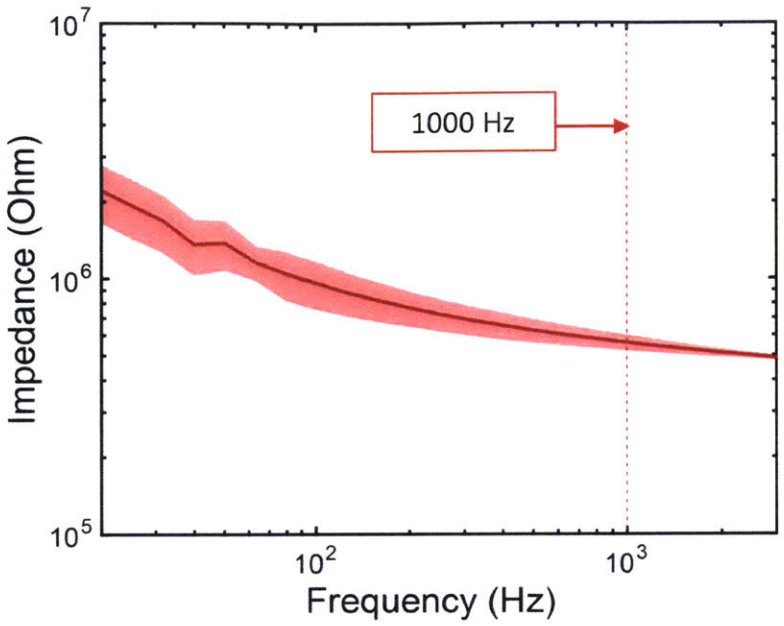

Figure 3.6 Impedance spectrum of electrode made of CNF-COC 10 wt%
Impedance spectrum of electrode made of CNF-COC 10 wt%. The impedance of such electrode at 100 Hz is 700 kOhm.

3.3 *In vivo* study

The electrodes made of CNF-COC (10 wt% CNF) are implanted in the brain of Thy1-ChR2-YFP transgenic mice (surgical procedures described in section 2.4.1). Neural activity evoked by optical stimulation was successfully recorded (Figure 3.7). The SNR of such electrode is 4.2125+/-0.8530 and the noise level is 17.853 μV [43].

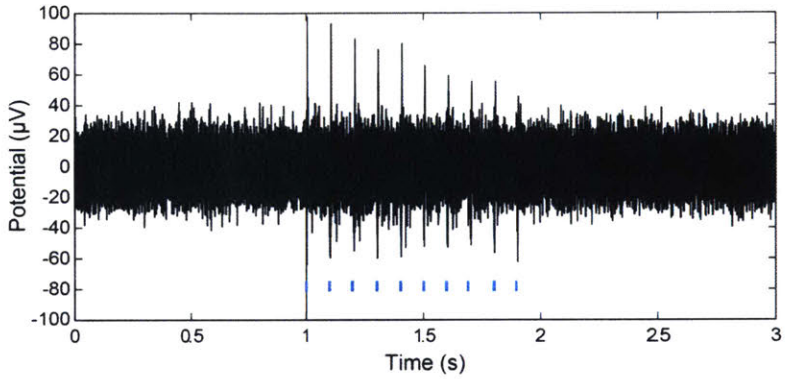

Figure 3.7 Neural recording of brain activity with simultaneous optical stimulation. Recording of neural activity evoked by optical stimulation in Thy1-ChR2-YFP mouse brain.

3.4 Conclusions

In this chapter, the percolation thresholds for electrical conductivity of various CNF composites and their thermomechanical properties have been studied. Based on the results, two types of composites (CNF-TPU and CNF-COC both 10:90 wt:wt) have been drawn into fibers. The CNF-COC fibers were evaluated for impedance and used for *in vivo* experiments. Compared to CPE fibers studied in Chapter II, the impedance of CNF-COC (10 wt%) electrode is reduced by an order of magnitude and the noise level of neural recording decreased by 20 %. However, there are still a few factors preventing single-unit recording. First, the size of the electrodes (40 x 40 μm^2) are larger than neurons (diameter of ~ 5-10 μm). Moreover, the impedance is not low enough for single unit-recording[190,202]. Limited with the thermomechanical properties and rheological behavior of high CNF loading composites, the lower bound of resistivity has been reached. To be free from limitations of T_g and any other rheological behaviors of the selected materials, fabricate electrodes separately to avoid the drawing process might be an alternative solution. Overall, a different electrode material may be necessary to provide single-unit recording.

Chapter IV Flexible and stretchable nanowire-coated neural probe

[This chapter is based on Lu et al., Science Advances 2017[203]]

4.1 Summary

To identify and better understand the neural pathways involved in loss of function in spinal cord injuries (SCI), devices that can modulate and/or record neural activities in the spinal cord may be beneficial. These devices must be sufficiently flexible to match the elastic neural tissue and withstand repeated strains experienced by the spinal cord during normal movement. In this chapter, flexible and stretchable fibers are designed to record the neural activity of mice spinal cords. The probes consist of thermally drawn polymeric fibers coated with micron-thick conductive meshes of silver nanowires. These hybrid probes maintain low optical transmission losses in the visible range and impedance suitable for extracellular recording under strains exceeding those occurring in mammalian spinal cords. Neural recording in freely moving mice confirms the ability of these probes to record endogenous neural activity in the spinal cord. Simultaneous stimulation and recording is demonstrated in transgenic mice expressing

channelrhodopsin 2, where optical excitation evokes electromyographic activity and hind limb movement correlated to local field potentials measured in the spinal cord.

4.2 Design and material selection

4.2.1 Flexible and stretchable waveguides

To match the mechanical properties of neural tissues, flexible polymer-based optical waveguides have been investigated to replace conventional rigid silica fibers[126,204-208]. Waveguides composed of SU-8 and poly(methylmethacrylate) (PMMA) fabricated via a lithographic process have been employed in the context of optogenetic neuromodulation[126], while PDMS and hydrogel-based devices are applied to fluorescence measurements and optical control of gene expression[208-210]. In this chapter, two different polymer systems are used for the fabrication of flexible and stretchable waveguides. Based on prior work applying multi-material fibers to optical neuromodulation[43,165], polycarbonate (PC, refractive index n = 1.58, glass transition temperature T_g = 145 °C, Young's modulus E = 2.38 GPa) and cyclic olefin copolymer (COC, n = 1.52, T_g = 158 °C, E = 3.0 GPa) are selected as the core and cladding of the flexible optical fiber, respectively [211-213] (Table 4.1). As an alternative device, more flexible fibers were fabricated from cyclic olefin copolymer elastomer (COCE, n = 1.51, melting temperature T_m = 84 °C, E = 34 MPa) (Table 4.1). In addition to its elastic properties and low elastic modulus, COCE is also compatible with a range of drawing parameters listed in Table 4.1. Unlike other elastomers with high optical transmission such as polydimethylsiloxane (PDMS) which does not have T_g or T_m below degradation temperature, the T_m of COCE allows it to be processed with fiber drawing. Alternatively, other transparent elastomers such as thermoplastic elastomers (TPE) and thermoplastic polyurethane

(TPU) can also be suitable for thermal drawing process. However, COCE is chosen because of its relatively low melting temperature (most of TPE and TPU have T_m > 100 °C)[214]. To establish stable processing conditions, sacrificial poly(methyl methacrylate) (PMMA, n = 1.49, T_g = 105 °C, E = 3.1 GPa) cladding is introduced into the preform (Table 4.1 and Figure 4.1). The resulting pillow-shaped COCE fibers (cross section width × height in the range from 125 μm × 100 μm to 250 μm × 200 μm) are tested for mechanical property (Figure 4.1). COCE is capable of sustaining more than 200% of strain while the maximum strain normally experienced by mammalian spinal cords is 12%[215] making COCE a promising material as neural probes in the spinal cord.

Materials	T_m or T_g (°C)	Refractive index	Young's modulus (MPa)	Drawing temperature (°C)
COC*	158	1.53	3000	150-270
PC[168]	150	1.586	2380	150-270
COCE	84	1.51	34	150-270
PMMA[169]	110	1.49	2200 to 3800	150-270
PDMS[209,216]	n/a	1.41–1.47	10s-100s	n/a

*The COC in this table indicates TOPAS© 6015.

Table 4.1 Chart for material properties
Various material properties for the material selections used in preform fabrication.

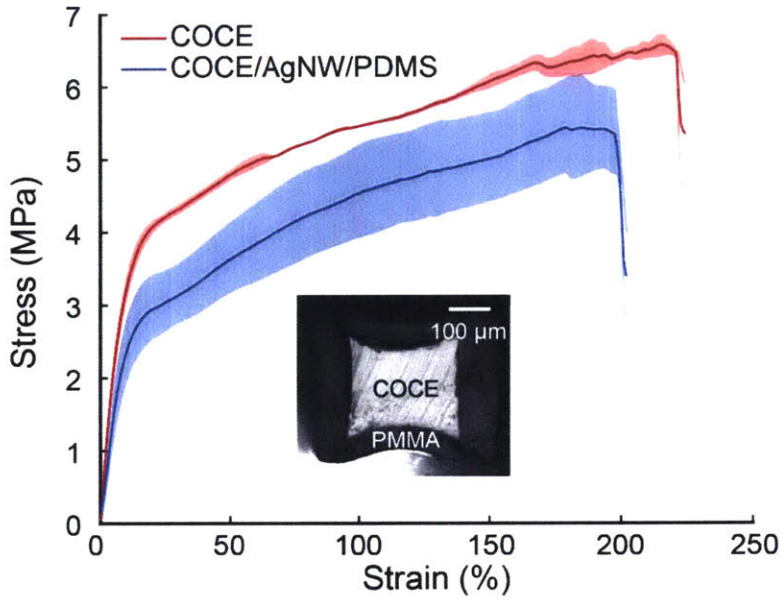

Figure 4.1 Stress- strain curve of COCE
Tensile tests performed for a thermally drawn COCE fiber as well as a COCE fiber probe coated with 3 layers of AgNW mesh and a protective PDMS cladding (COCE/AgNW/PDMS) (n=5 devices).

4.2.2 Silver nanowire mesh electrodes

In addition to a waveguide, integrated electrode within the neural probe is needed to record neural activity during optogenetic neuromudulation[122,124-126,217]. The conductive polymeric electrodes described in Chapters II and III exhibit impedances as high as tens of megaohm[43,165,218] which prevents single-unit recording. Metallic electrodes deposited on polymer substrates possess lower impedance, but are subject to cracking[219]. Fractal and serpentine metallic electrodes defined via contact printing are less fragile compared to metallic electrodes but offer limited spatial resolution[15,16,107,220,221]. Alternatively, a metal mesh network, which is usually a thin film formed with dense dispersion of metal nanowires, can possess the electrical characteristics of metals but also be resilient to bending deformation and is a more promising electrode for flexible electronics applications[185,222-225]. Other than flexible electronics such as display panel, recent work has also reported the application of AgNW meshes in monitoring of cardiac function[182]. In addition to the

advantages mentioned above, AgNW coating is more compatible with facile solution-based processing[222]. Thus, AgNW coating is investigated as the electrode material for flexible neural probes

4.3 Fabrication

4.3.1 Fiber drawing process

To fabricate a preform for PC/COC waveguide, a PC cylinder (diameter = 9 mm, McMaster-Carr) is wrapped in COC sheets (thickness = 0.002″, TOPAS Advanced Polymers, 6015S) to the total preform diameter of 12.5 mm. The entire structure is then consolidated at 190°C for 12 minutes in vacuum. The fiber is drawn at 280°C, and the drawing speed is varied from 1 to 7 m/min to achieve draw-down ratios in the range 30-140 (Figure 4.2).

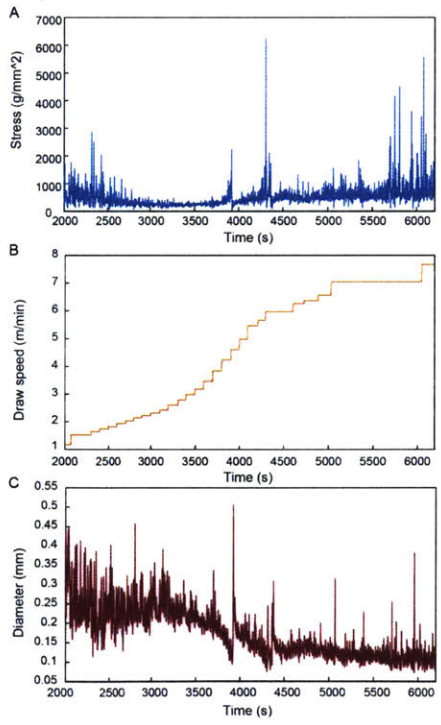

Figure 4.2 Draw data of PC/COC fibers
(A) Stress applied to the fiber with a polycarbonate (PC) core and cyclic olefin copolymer (COC) cladding during the thermal drawing process. (B) Drawing speed used to control the stress within the fiber. (C) Resulting fiber diameter correlated to the drawing speed and stress.

To fabricate the preform for COCE fibers, pellets of COCE (TOPAS® Elastomer E-140) were first cast-molded into rectangular strips (L = 100 mm, W = 6 mm, H = 6 mm) at 180°C in vacuum. PMMA (thickness = 0.5 inch, McMaster-Carr) plates were machined into two 1" wide strips, followed by machining grooves in the center of each strip and filling those with molded COCE. The preform is then consolidated under pressure (50 psi, 125 °C) for 14 hours and cooled to room temperature while concomitantly reducing the applied stress. The preform is drawn at 240°C, and the resulting fiber dimensions are reduced by 40-80 times at the drawing speed of 2-9 m/min (Figure 4.3).

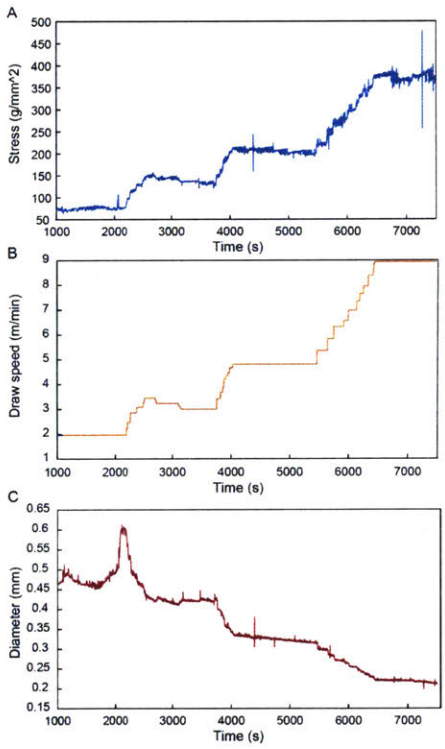

Figure 4.3 Draw data of COCE/PMMA fibers
(A) Stress applied to the fiber with a cyclic olefin copolymer elastomer (COCE) core and poly(methyl methacrylate) (PMMA) cladding during the thermal drawing process. (B) Drawing speed used to control the stress within the fiber. (C) Resulting fiber diameter correlated to the drawing speed and stress.

For PC/COC fibers, the ratio of each material does not affect the drawing stability since both polymers are thermoplastic with similar properties such as elastic modulus and T_g (Table 4.1). However, the volume ratio of COCE and PMMA affects the drawing conditions. Since COCE melts (Table 4.1) during the drawing, the volume of PMMA cladding may need to be thick enough to support the draw or the fiber may break during the draw (Figure 4.4).

Figure 4.4 An example of failed COCE/PMMA preform
The cladding layer (PMMA) is too thin to support the melt COCE inside the preform during the thermal drawing process.

After the fiber drawing process, the fiber probes are connected to zirconia ferrules (Thorlabs, CF128) using optical epoxy (Thorlabs, F112). To ensure maximum light output, the ferrule end of the fiber was polished to reduce light loss between the connecting joint from the laser to the fiber. For the PC/COC system, the fiber can be polished together with the attached ferrule with silicon-carbide sandpaper. However, since COCE is an elastomer, itcould not be polished with sandpaper. Therefore, to maximize the light output, the COCE fiber was glued (UV-curable index matching epoxy n = 1.48, NOA 148, Norland Product, Inc.) to a piece of silica fiber (Thorlabs, FG200LEA) with similar size before it was attached to a ferrule. The COCE and silica fibers were first placed on the fiber launch (MBT610D) with laser aligned to the fiber cores, and a photodetector was placed in the end of the COCE fiber to check the alignment. Once the position was optimized, i.e., the COCE and silica fibers were aligned and the light output was at the maximum level, a drop of index matching epoxy was applied to the interface of the two fibers and cured with a UV lamp (wavelength = 365 nm). Afterwards, the silica end was inserted into the ferrule (Thorlabs, CF230)

and fixed with optical epoxy (Thorlabs, F112). The index matching epoxy between the silica and COCE fibers provideed a smooth optical transmission to minimize the light loss. The silica end inside the ferrule was then polished.

4.3.2 Silver nanowire coating process

To enable neural recording, nanometer- thick conductive layers of silver nanowires (AgNWs) (10 mg/ml in isoproponal, Novarials NovaWire-Ag-A70-IPA, diameter d = 70 nm, length L = 40 μm) were deposited on the fibers via dip coating (Figure 4.5A). To fabricate meshes with low resistivity, different concentrations of AgNWs for dip-coating were tested. At concentrations >6 mg/ml, the resistivity of the AgNW mesh was proportional to the concentration of the dip coating solution (Figure 4.6). To account for potential breakages and delamination of mesh networks on the probe surfaces during deformation, the lowest resistance mesh (9.37×10^{-4} Ohm-cm) was selected for the rest of the study.

Since the hydrophobicity of COC limited the adhesion and deposition of AgNWs from isopropanol[226], fibers were treated with oxygen plasma prior to AgNW-coating to enhance the uniformity of AgNW mesh layers[226,227]. The surface of the fiber probe was first treated with oxygen plasma and then dipped into isopropanol (IPA) solution of AgNW and air-dried. The dip coating was repeated 3 times.

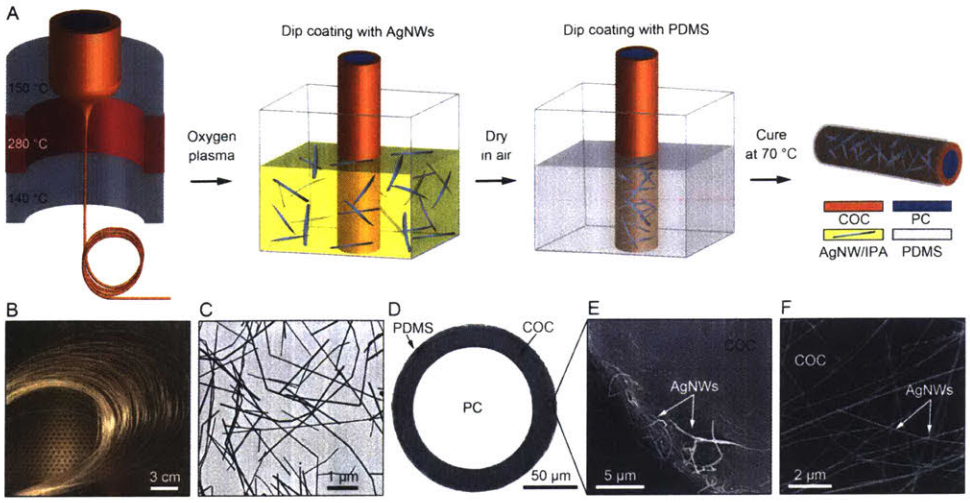

Figure 4.5 An illustration of the fiber probe fabrication
(A) An illustration of the fiber probe fabrication. (B) A spool of a fiber with polycarbonate (PC) core and cyclic olefin copolymer (COC) cladding. (C) A transmission electron microscope image of the silver nanowires (AgNWs). (D) Cross-sectional image of the fiber probe. (E) Scanning electron microscope (SEM) shows a portion of the ring AgNW electrode cross section. (F) SEM image of the AgNW mesh on top of the fiber surface.

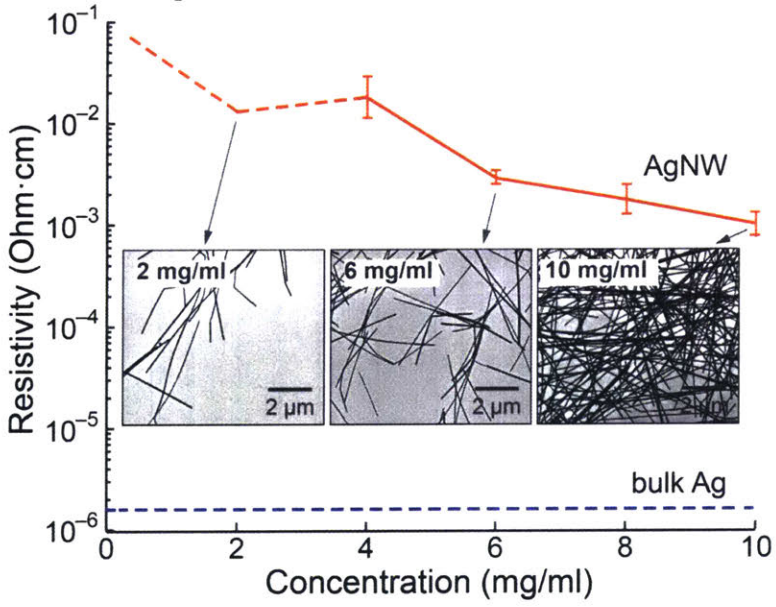

Figure 4.6 Concentration of AgNW solution and its resistivity
Resistivity of the mesh as a function of AgNW solution concentration. Inset: TEM images of the AgNW meshes deposited from solutions with 2%, 6% and 10% concentrations. AgNW mesh deposited from 10% solution was used for further characterization and *in vivo* evaluation.

After the dip-coating process, the fiber was connected to a copper wire (Arcor Electronics, AWG 38) via a conductive silver paint (SPI Supplies, 04998AB), and then air-dried for 2 hours. The joint between the fiber probe and the copper wire was then sealed with epoxy (Devcon, 5 Minute® Epoxy) to enforce the connection. The copper electrode lead was then soldered to a 4-pin connector (Digi-Key ED90528-ND) for electrophysiological data acquisition. The fibers were then coated with polydimethylsiloxane (PDMS, n ~1.41–1.47, thickness 5 μm)[209] at a 30 to 1 weight ratio at 70°C for 1 hour to minimize the direct contact of AgNW with the tissue and prevent surface oxidation and mechanical degradation. PDMS was selected as a protective coating for the conductive layer because of its low modulus (10s of kPa for 30:1 polymer to curing agent by weight) and low refractive index, which improves the confinement of light to the PC/COC and COCE cores[216]. Following dip-coating with PDMS the probe tips were cut orthogonal to the fiber axis exposing thin conductive AgNW ring electrodes (Figures 4.5D-E). The final device diameter ranged between 105-135 μm, and was constrained by the dimensions of the structural fiber core (100-130 μm) (Figure 4.5D). Prior to implantation, the fiber probes were coated with molten water-soluble poly(ethylene glycol) (PEG, molecular weight MW= 1000) to temporarily stiffen them for implantation.

4.4 Characterization

4.4.1 Optical characterization

The difference between the refractive indices of PC and PDMS is 0.18. Although this should in principle be sufficient to sustain multimode transmission through the fiber even in the absence of COC cladding (Figure 4.7), direct coating of AgNWs onto the PC surface resulted in

significant losses due to scattering and evanescent coupling of light into the plasmon modes of these nanomaterials (Fig. 4.8A)[228]. Addition of the COC cladding reduced the losses from 2.5 dB/cm to 1.9 dB/cm (n = 5) (Fig. 4.8A). Due to their flexibility, these probes were able to maintain transmission under deformation (Fig. 4.8B), including when usedas sutures (Fig. 4.8C).

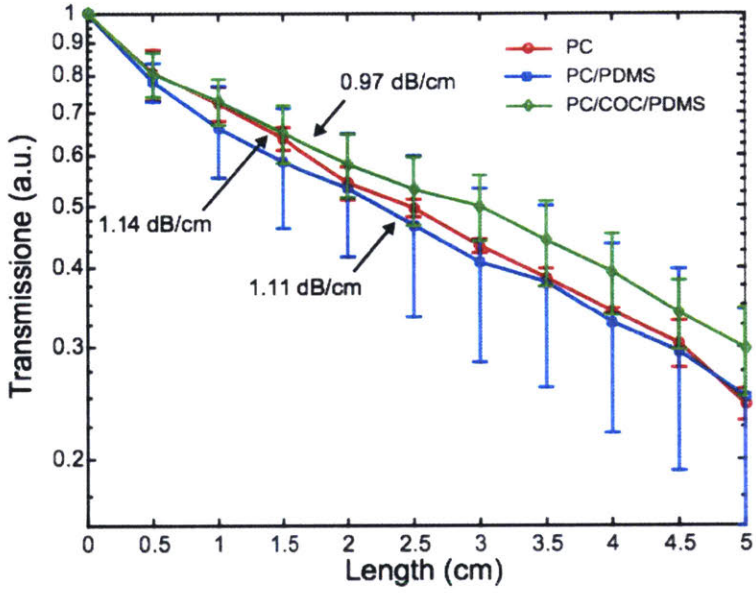

Figure 4.7 Optical characteristics of COC fiber
Transmission at a wavelength λ = 473 nm for pure PC (1.11 dB/cm), PC/COC (0.97 dB/cm), and PC/COC (0.97 dB/cm) fibers coated with poly(dimethylsiloxane) (PDMS) as a function of length. Loss coefficients for the devices are indicated on the plot.

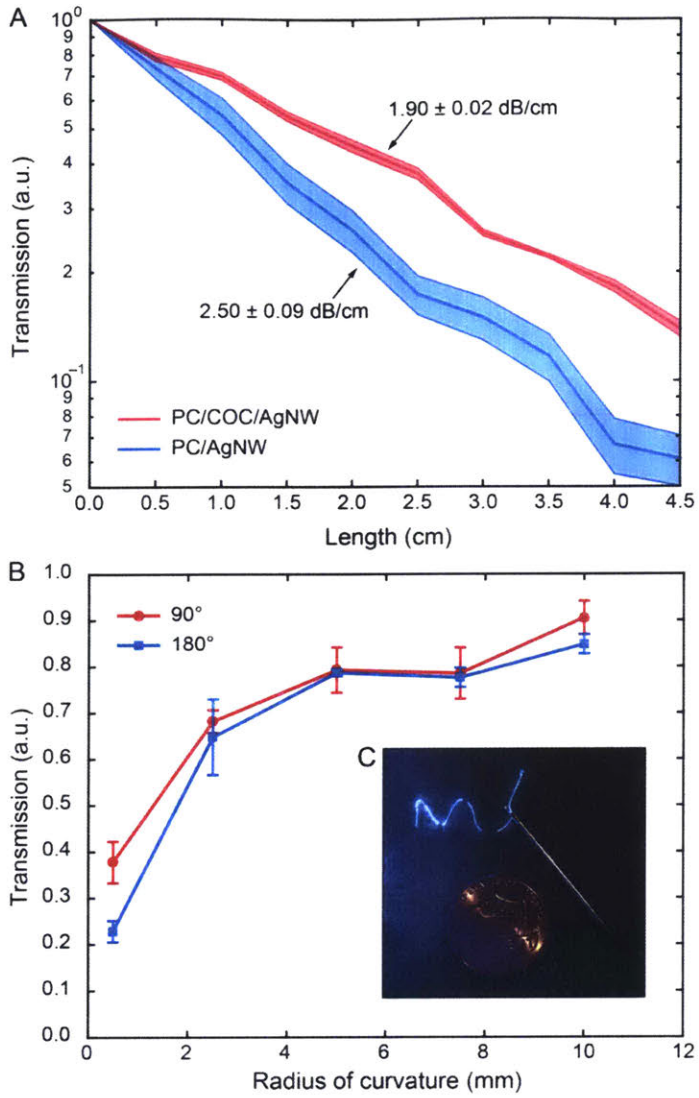

Figure 4.8 Optical loss of PC/COC fiber with AgNW coating
(A) Normalized transmission at a wavelength λ = 473 nm as a function of length for fiber probes with and without COC cladding to separate AgNW mesh from the PC optical core with a diameter of 120 μm. (B) Transmission at λ = 473 nm for PC/COC/AgNW/PDMS fiber probes (core diameter = 120 μm) bent at 90° or 180° with radii of curvature from 0.5 mm to10 mm. Data were normalized to the transmission of straight probes. A photograph of a PC/COC/AgNW/PDMS fiber probe connected to a laser source, threaded through a needle, and used to create several stitches on fabric.

Consistent with lower optical transmission of COCE as compared to PC and COC, higher optical losses of 3.98 dB/cm were observed for AgNW-coated COCE core fibers (n = 3) (Figure 4.9).

Nevertheless, the elastic property of COCE allowed the transmission of light under stretching and bending deformations making it a promising waveguide for optogenetics manipulation in the spinal cord (Figure 4.10).

Consistent with lower optical transmission of COCE as compared to PC and COC, higher optical losses of 3.98 dB/cm were observed for AgNW-coated COCE core fibers (n = 3) (Figure 4.9). Nevertheless, the elastic property of COCE allowed the transmission of light under stretching and bending deformations making it a promising waveguide for optogenetics manipulation in the spinal cord (Figure 4.10).

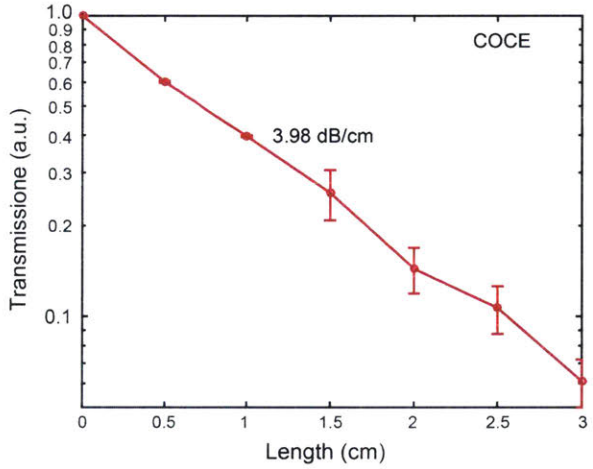

Figure 4.9 Optical loss of COCE fiber
Transmission at a wavelength $\lambda = 473$ nm for COCE fiber. Loss coefficient is indicated on the plot.

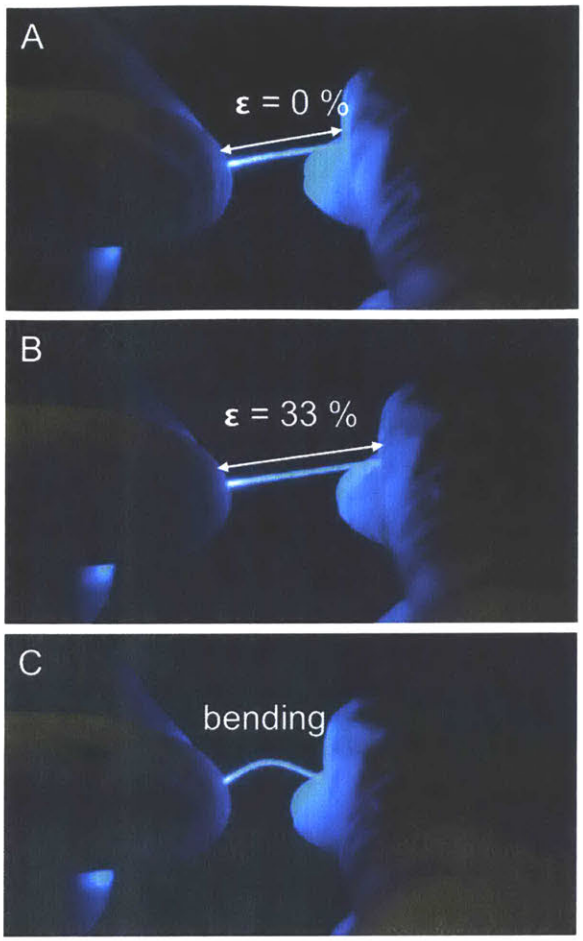

Figure 4.10 Optical performance of COCE fiber under deformation
Laser (wavelength λ = 473 nm) was coupled to a COCE fiber. The COCE was capable of guiding light under various degrees of deformations. (A) no force, (B) tensile stress resulting in 33 % of strain, and (C) bending are applied.

4.4.2 Electrical characterization

The impedance of the probes with nanometer-thick conductive layers of silver nanowires (Figure 4.6B-F) was similar to that of solid metallic electrodes at 1 kHz. In addition, the impedance depended more on the contact area rather than the length. Mesh electrodes within 1 cm and 10 cm fiber probes exhibited impedance values of similar order of magnitude ($|Z_{PC/COC,\ 1cm}| = 50 \pm 26$ kΩ, $|Z_{PC/COC,\ 10cm}| = 58 \pm 21$ kΩ). Therefore, the probes can potentially be scaled up from small rodents to larger animals (Figure 4.11A).

In addition to bending, AgNW mesh concentric electrodes were also resilient to stretching deformation. Uncoated COCE fibers sustained up to 230% strain and when coated with AgNWs and PDMS, could be stretched up to 200% strain (Figure 4.1). AgNW mesh electrodes coated onto 1 cm and 10 cm COCE fibers exhibited somewhat greater difference in impedance ($|Z_{COCE,\ 1cm}|$ = 34 ± 17 kΩ, $|Z_{COCE,\ 10cm}|$ = 162 ± 50 kΩ) (n = 5) as compared to their PC/COC analogs (Figure 4.11B). The absolute values of impedance, however, are still well within the range suitable for extracellular recordings even for 10 cm long fibers.

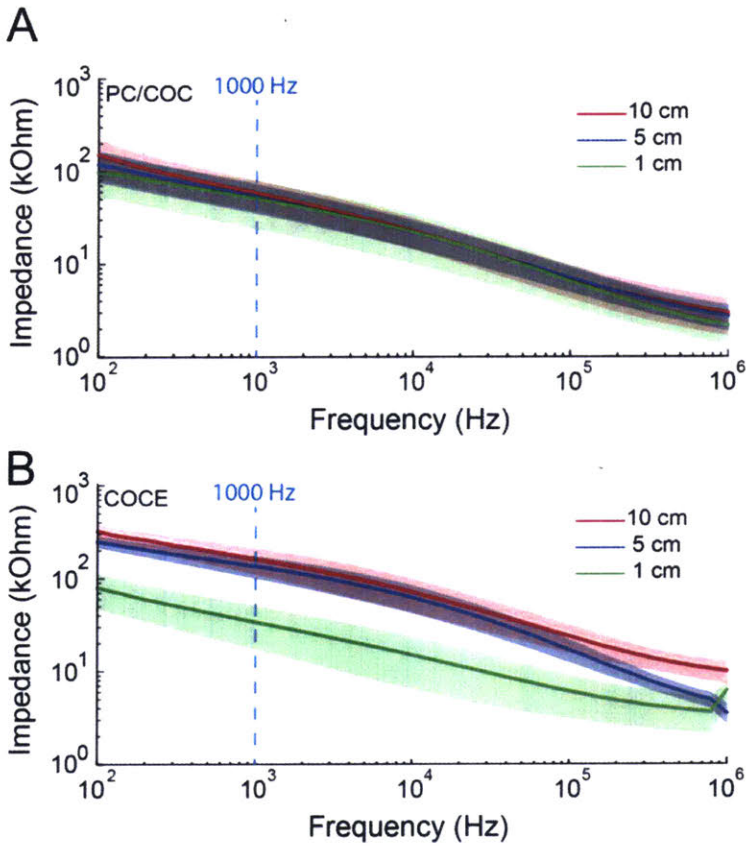

Figure 4.11 Impedance spectra of AgNW mesh electrodes on PC/COC and COCE cores
Impedance spectra of the AgNW mesh electrodes deposited onto 1 cm, 5 cm and 10 cm long fibers with (A) 120 μm PC/COC cores and (B) 200×200 μm^2 COCE cores.

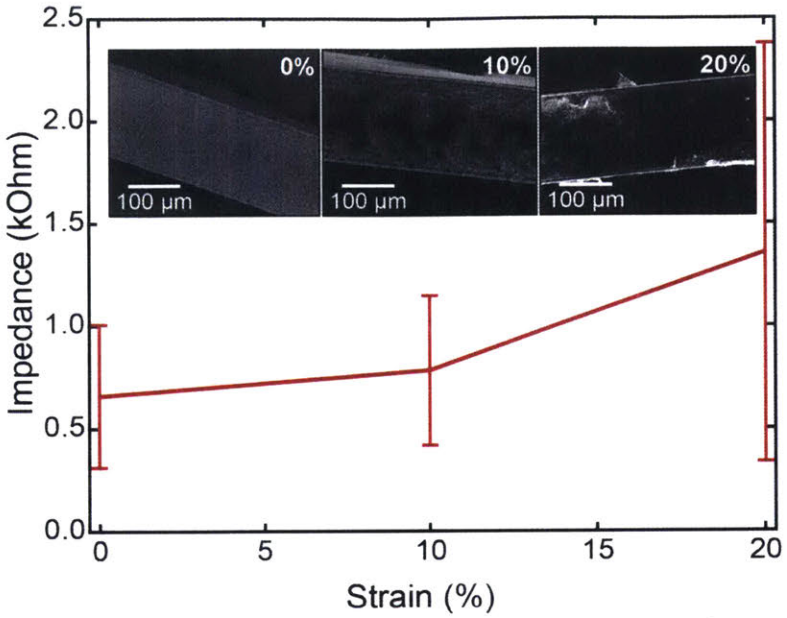

Figure 4.12 Impedance of AgNW mesh electrodes under various strain on COCE cores. Impedance of cyclic olefin copolymer elastomer (COCE) fibers coated with a single layer of silver nanowire (AgNW) mesh and measured at 0%, 10%, and 20% extension strain. Inset: scanning electron microscope (SEM) images of the COCE/AgNW/PDMS fibers under 0%, 10%, and 20% strain.

It is observed that a single-layer AgNW mesh coating couldwithstand strains of ~30% before losing conductivity due to the disruption of the conductive network (Figure 4.12). In contrast, electrodes composed of a 3-layer AgNW mesh maintained low impedance at strains up to ~100% (Figure 4.13A). This is consistent with SEM images, whichdo not reveal any structural differences between the AgNW mesh-coated fibers under 0%, 10%, and 20% strain (Figure 4.13B). Repeated extension of the COCE/AgNW/PDMS fibers resulted in negligible hysteresis of the electrode impedance indicating resilience of these devices to deformation (Figure 4.13C). Since the spinal cord and peripheral nerves only experience strains up to ~12%[215], the low-impedance AgNW-mesh coated fibers provide arbitrarily scalable and stretchable alternatives to polymer-composite and metallic electrodes.

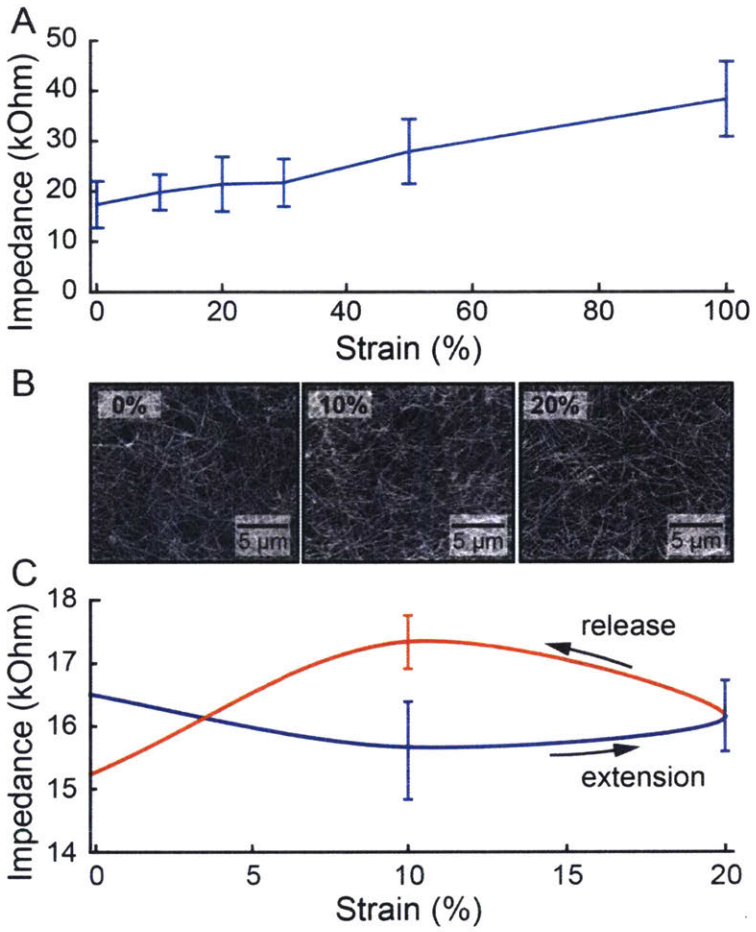

Figure 4.13 Impedance of AgNW mesh electrodes under various strain on COCE cores
(A) Impedance of a 3-layer AgNW mesh within COCE/AgNW/PDMS probes with core dimensions of 200×200 μm^2 as a function of tensile strain. (B) SEM images of the 3-layer AgNW mesh deposited onto COCE fiber at 0%, 10%, and 20% strain. (C) Impedance of fiber probes characterized in (A) measured over 5 extension and release cycles.

4.5 *In vivo* study – acute

4.5.1 Procedures

After all the characterization, flexible/stretchable fiber probes were tested *in vivo*. The surgical procedure and detailed information of optical stimulation were described in section 2.4.1. The probes are connected to a high impedance headstage (Tucker Davis Technologies, ZIF-Clip 32) through a custom PCB adapter board. The signals were sampled at 48 kHz (PZ2, Tucker Davis Technologies) and filtered (0.3-10 kHz, Infinite impulse response, IIR, 3rd order) in MATLAB (Mathworks). Single neuron action potentials (spikes) were isolated by detecting threshold crossings at 2 standard deviations from the noise level, projecting the spikes onto the first two principal components, and then clustering with k-means. Interspike interval (ISI) histograms were calculated from the sorted units.

Electromyographic (EMG) signals were recorded from the gastrocnemius muscle with two polytetrafluoroethylene (PTFE) coated stainless steel wires (A-M Systems, 50 μm/115 μm diameter Bare/Coated). The 1 mm tips of the wires were exposed using a scalpel to reduce impedance before insertion into the muscle belly with a 25-gauge needle. The EMG signals were amplified by the high impedance headstage, and sampled at 48 kHz. Single ended recordings relative to a low impedance distant reference and ground were collected from each electrode. These recordings were low-pass filtered (Finite impulse response, FIR, 25th order, 5 kHz corner frequency) and subtracted in MATLAB to produce a differential recording.

Sensory evoked potentials were recorded from the dorsal columns of anesthetized wild type mice using AgNW mesh electrodes on PC/COC cores. Electrical stimuli are applied peripherally to the ipsilateral hind limb. Two stainless steel wires, identical to those described in the EMG section

above, were inserted subcutaneously near the ankle. The wires were placed medial and lateral to the ankle. Biphasic current pulses (125 μs/phase, 1-8 mA) were delivered every 2 seconds. The resulting volley of activity was recorded at the dorsal columns with the AgNWs electrodes. The experiment was repeated after flipping the polarity of the biphasic pulse as a control. An adaptive filter was applied to remove power line noise without introducing impulse response artifacts near the stimulus. The area under the first positive peak was integrated at each stimulus level to create a recruitment curve. The curve was fit to a sigmoid using a weighted least squares regression on a positive range in MATLAB.

4.5.2 Recording of neural activity and sensory evoked potentials

With the approaches described in the previous section, the ability of the AgNW coated fibers to record neural activity in the mouse spinal cord was evaluated (Figure 4.14).

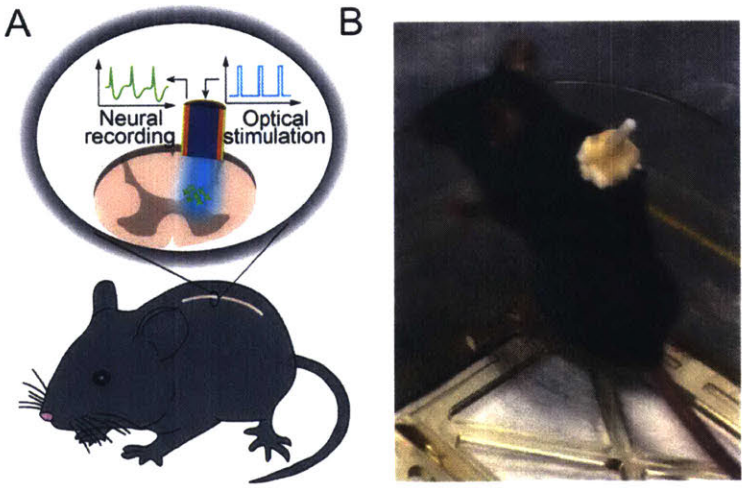

Figure 4.14 Illustration of a fiber probe implanted in a mouse spinal cord
(A) A schematic depicting optical stimulation and electrophysiological recording with a fiber probe in a mouse spinal cord. (B) A picture of mouse implanted with a flexible neural probe between L1 and L2 exploring its environment.

The ability of both PC/COC and COCE fiber probes with AgNW electrodes to record spontaneous neural activity was first evaluated with acute experiments in anesthetized mice (Figure 4.15). Single neuron signals were processed with procedures described in section 1.2.1 and Figure. 1.6. The isolated signals (Figures 4.15 C, D) were assessed by principal component analysis (Figures 4.16A, C) and interspike interval histograms (Figures 4.16B, D) to confirm their characteristics. In addition to spontaneous activity, robust sensory evoked potentials from the dorsal columns were recorded and could be scaled up with current applied to the ipsilateral hind foot (Figure 4.17).

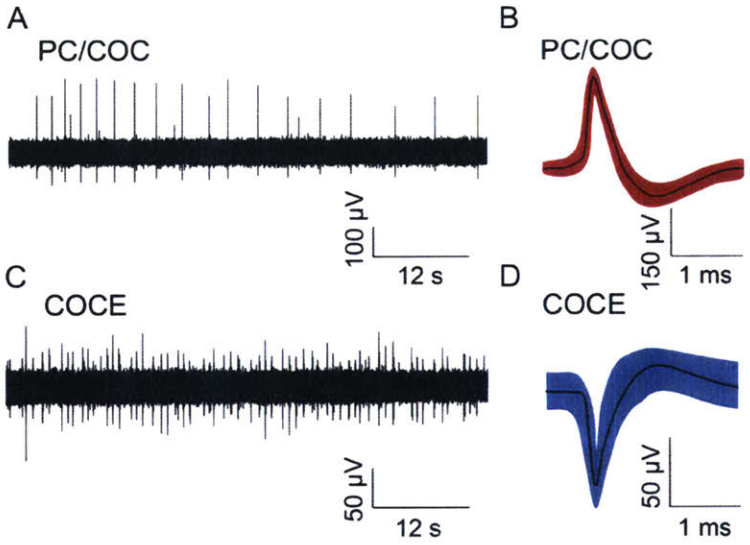

Figure 4.15 Recording of spontaneous activity in mice spinal cords
(A) Spontaneous activity recorded in acute conditions with AgNW concentric mesh electrodes deposited onto PC/COC core fibers in spinal cord of wild type (WT) mice. (B) Action potentials isolated from the recording in (A). (C) Spontaneous activity recorded in acute conditions with AgNW concentric mesh electrodes deposited onto COCE core fibers. (D) Action potentials isolated from the recording in (C).

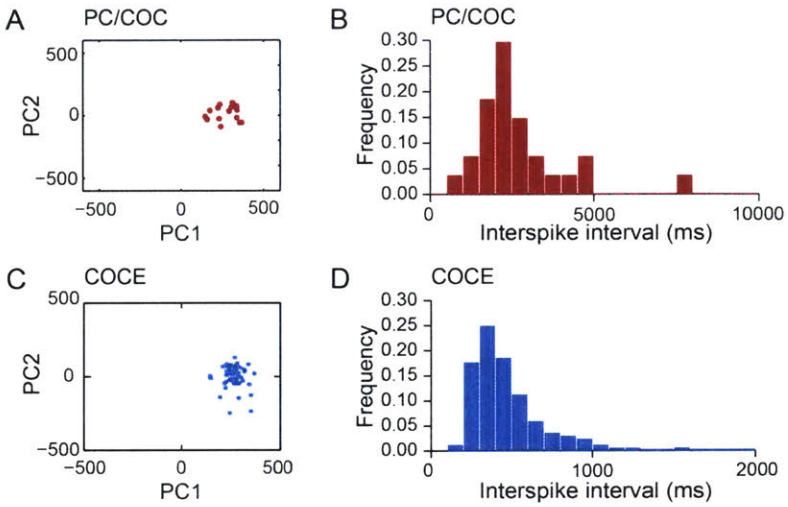

Figure 4.16 Spontaneous single units isolated during acute anesthetized recordings
(A, B) Principal component analysis (A) and the corresponding interspike interval histogram (B) for the unit recorded using a flexible probe with a PC/COC core (raw electrophysiological data and action potential shape are shown in Fig. 4.15A, B). (C, D) Principal component analysis (C) and the corresponding interspike interval histogram (D) for the unit recorded using a stretchable probe with a COCE core (raw electrophysiological data and action potential shape are shown in Fig. 4.15C, D).

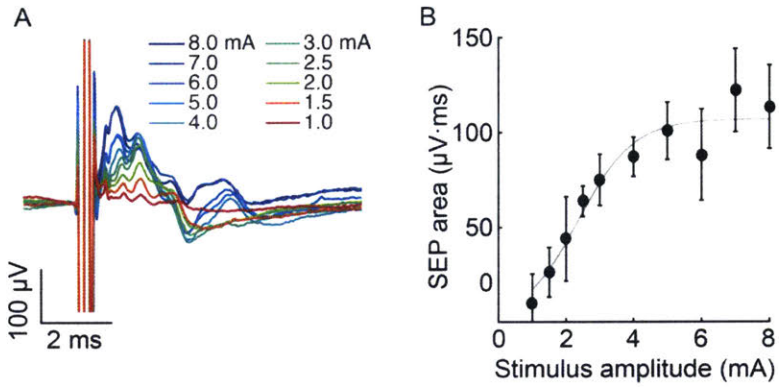

Figure 4.17 Recording of sensory evoked potentials
(A) Sensory evoked potentials recorded acutely from the dorsal column with AgNW mesh electrodes within PC/COC based probes at different input currents (1-8 mA, 125 µs/phase biphasic). Sensory potentials are preceded by the electrical stimulus artifact. (B) Sensory evoked potential recruitment curve relating the area under the first positive peak to the stimulus amplitude.

4.5.3 Simultaneous optical stimulation and recording of evoked activity

To evaluate the capability of the flexible and stretchable neural probes, the optoelectronic fibers with PC/COC and COCE optical cores were implanted into the lumbar region (L1) of the spinal cord of wild type as well as Thy1-ChR2-YFP transgenic mice that broadly express light sensitive cation channel ChR2[191].

In Thy1-ChR2-YFP mice, illuminating the lumbar region of the spinal cord with 125-168 mW/mm^2 laser light with a wavelength $\lambda = 473$ nm (activation peak of ChR2) coupled into fiber cores through ferrules consistently evoked neural activity correlated with the 5 ms optical pulses at 10 Hz (latency 10.6±0.5 ms) (Figures 4.18A, C). Stimulation at a higher frequency of 100 Hz similarly evoked neural activity (Figures 4.18B, D). In this case, however, the observed multi-neuron potentials did not follow each laser pulse, which is consistent with ChR2 kinetics[229].

Neural activity in the lumbar spinal cord induced by optical pulses delivered through the fiber probes was sufficient to produce muscle contractions in the ipsilateral hindlimb (Figures 4.18E, G, and 4.19). To evaluate the downstream effect of optical stimulation in lumbar spinal cord, EMG electrodes were implanted on the gastrocnemius muscle. It is found that the electromyographic activity recorded in a gastrocnemius muscle (Figure 4.18G) was correlated with the optically evoked local field potentials recorded with the AgNW mesh coated COCE fibers in the lumbar spinal cord (Figure 4.18F). Moreover, the amplitude of EMG was also positively correlated with the light intensity from the optical stimulation (Figures 4.19 A and B).

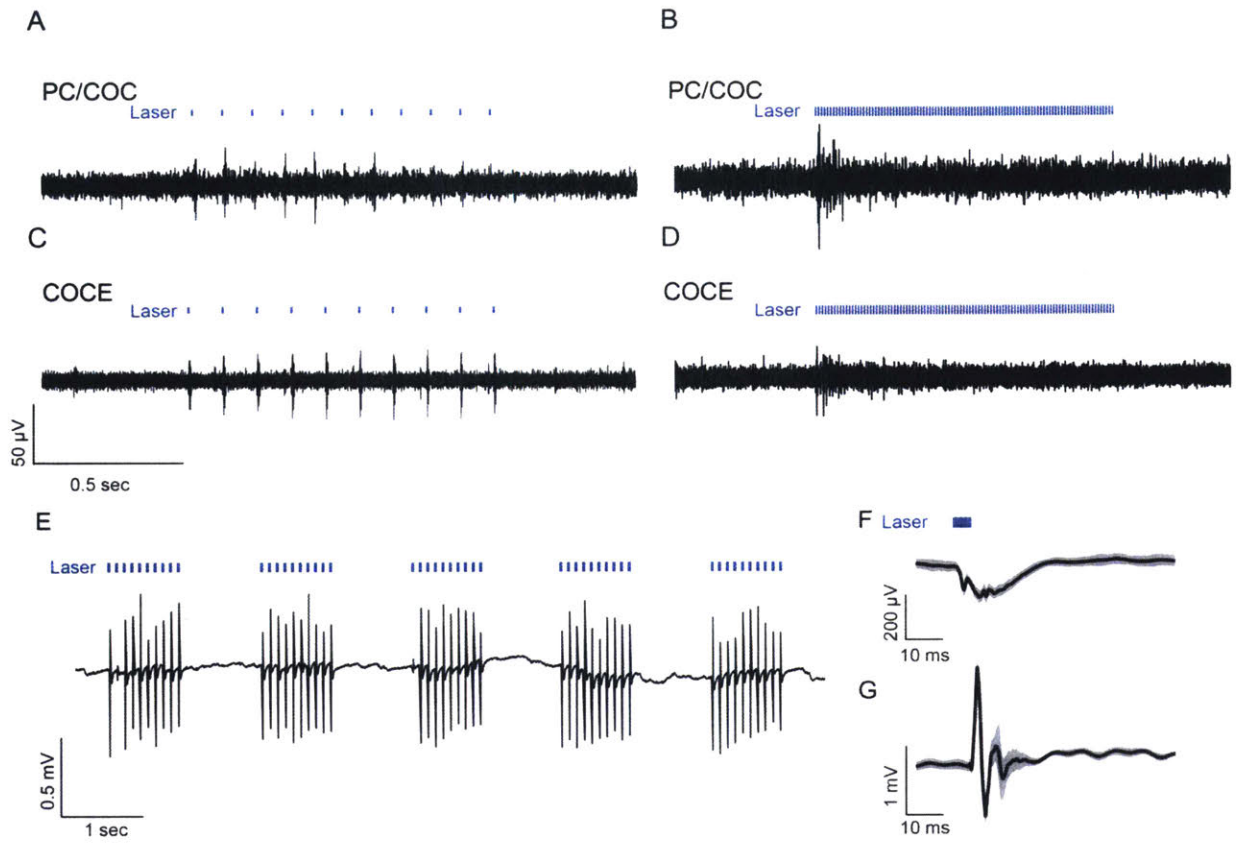

Figure 4.18 Simultaneous optical stimulation and electrical recording
(A, B) Neural activity in a spinal cord of a Thy1-ChR2-YFP mouse evoked by optical stimulation (wavelength $\lambda = 473$ nm, 168 mW/mm^2, 5 ms pulse width, 10 and 100 Hz) delivered through the PC/COC fiber and recorded with the concentric AgNW mesh electrodes. (C, D) Neural activity in spinal cord of a Thy1-ChR2-YFP mouse evoked by optical stimulation (wavelength $\lambda = 473$ nm, 125 mW/mm^2, 5 ms pulse width, 10 and 100 Hz) delivered through the COCE fiber and recorded with the concentric AgNW mesh electrodes. (E) EMG evoked by the optical stimulation in (C). (F) Optically evoked local field potentials recorded with AgNW mesh electrodes within COCE fiber. (G) An expanded view of the averaged EMG signal from (E).

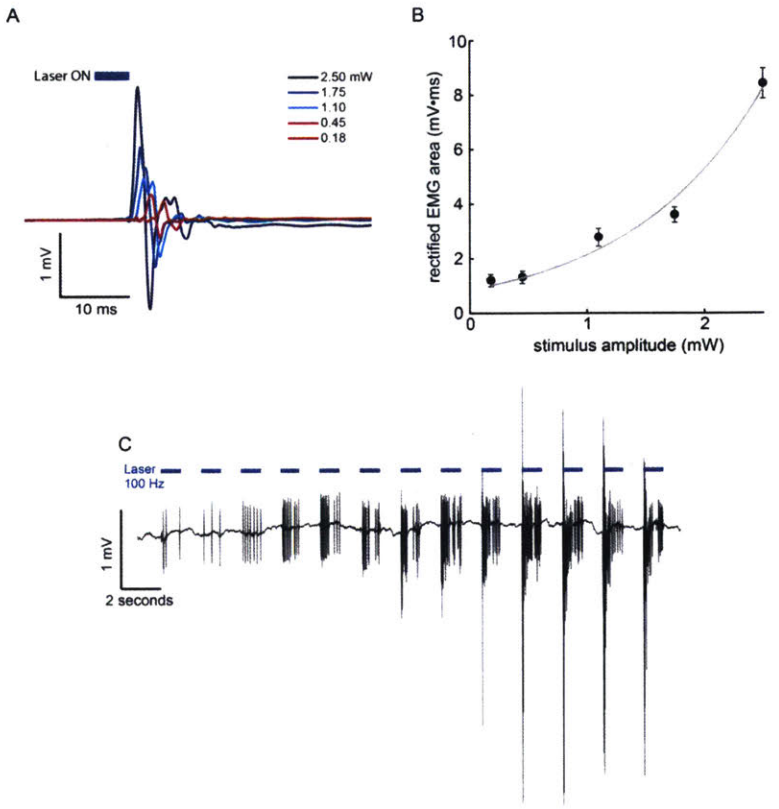

Figure 4.19 *In vivo* electromyographic (EMG) recordings
(A) EMG signals evoked in Thy1-ChR2-YFP mice by optical stimulation (wavelength $\lambda = 473$ nm, 5 ms pulse width, 2 Hz) of the lumber spinal cord via a COCE fiber (size: 200×200 μm^2) inserted 300 μm deep into the cord. The delayed EMG response to optical excitation for lower excitation powers is consistent with the commonly accepted ChR2 activation threshold of 1 mW/mm^2. Specifically, for lower optical powers the amount of light reaching motor pools is insufficient to activate ChR2-mediated firing, and the observed delayed EMG response is likely a result of sensory feedback. Higher optical powers enable direct activation of motor neurons, and a low-latency EMG response is observed. (B) EMG recruitment curve relating the rectified EMG area in (A) to the optical power. (C) Electromyography (EMG) of the gastrocnemius caused by high-frequency optical stimulation (wavelength $\lambda = 473$ m, 125 mW/mm^2, 5 ms pulse width, 100 Hz) applied to the spinal cord. In comparison to 10 Hz stimulation (Fig. 5K), the EMG response does not follow each optical pulse due to the kinetics of ChR2. Interestingly, the EMG response in this example increases over time, indicating that the motor system is far from linear time-invariant.

4.6 *In vivo* study – chronic

4.6.1 Background and challenges

Chronically recording neural activity from the spinal cord is extremely challenging due to the associated movement and the weak mechanical properties of the spinal cord. To achieve chronical recording in the spinal cord, it is crucial to have sufficient mechanical compliance so that the probe can move with the tissue. There are several works demonstrating neural recording in mammalian spinal cords both acutely and chronically. For instance, single-unit recording in cat spinal cord with a chronically implanted chamber and moveable electrodes was demonstrated[173,230,231]. In addition, another study reported a braided microwire device with a compliant tethered for recording single units from the rat spinal cord in a terminal preparation. In this report, the spiking activity in the spinal cord was evoked by electrically stimulating the mesencephalic locomotor region (MLR) of the brainstem in decerebrated rats and neural activity was recorded [232]. To our knowledge, prior to this work, there is only one report of chronic multiunit recordings in rodent spinal cord[233], which reported implantation of PtIr microwires for four weeks into rats. All of these approaches cannot be directly applied on behaving mouse due to the limitations in reducing the size of the microwires. Therefore, we aimed was to develop tools that are suitable for mice, and to take advantage of the wide selection of mouse models, including those suitable for optogenetics, to study spinal cord injury at a cell type-specific level, with closed-loop physiology, and as the mouse behaves. In the following sections, progress on the development of such tool will be reported.

4.6.2 Fiber Implantation Procedures

To evaluate fiber implantation into the mouse spinal cord, a novel surgical approach was developed. All procedures involving vertebrate animals wereapproved by the MIT Committee on Animal Care. Fiber probes were tested in wild type mice (BL6/57, The Jackson Laboratory) (housed at12h light/dark cycle, 22 °C, food and water ad libitum).

The AgNW and PDMS coated PC/COC and COCE fiber probes were chronically implanted into the lumbar region of the spinal cord of Thy1-ChR2-YFP and wild type mice. The surgical procedures were described in section 2.4.1 and the neural probe implant procedure is described as followings. To fix the implant for chronic recording, the following procedures were used:

1. A low impedance ground/reference wire (stainless steel) was coiled and placed next to the veterbral column under the skin.
2. The probe was secured with dental cement (Metabond, Parkell) to the three fused vertebral segments (T13, L1, and L2). The dental cement should cover the area of the entire incision. No suture was necessary, but tissue glue was used whenany small openings on the skin was observed.
3. After the implantation, the mouse was recovered on a warm pad.

After the surgery, the mouse should not be paralyzed and all four limbs should be able to move freely (Figure 4.14B)

4.6.3 Neural recording in the spinal cord of freely moving mice

Electrophysiological activity was recorded with both AgNW-coatedPC/COC and also COCE probes in tethered freely moving wild type mice up to 1 week following the implantation surgery (Figure 4.12). Recordings from freely moving mice contained a combination of multi-unit

activity and movement artifacts and were confounded by greater noise levels than those performed under anesthesia. The noise level, however, remains stable over the week-long study.

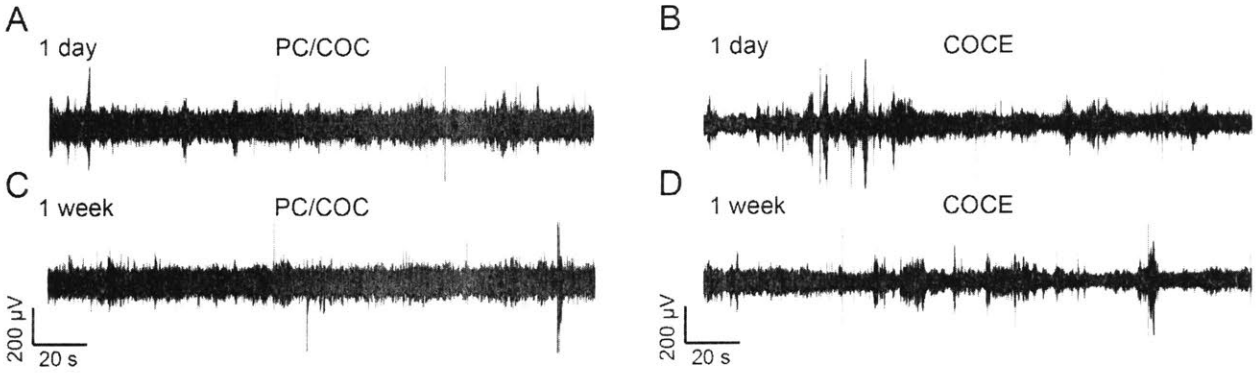

Figure 4.15 Electrophysiological recordings collected during tethered free behavior
Electrophysiological recordings collected during tethered free behavior one day (A, B) and one week (C, D) following implantation. The recordings were performed using AgNW mesh electrodes within flexible probes with PC/COC cores (A, C) and within stretchable probes with COCE cores. Individual neuron action potentials could not be isolated due to the presence of movement artifacts.

4.6.4 Biocompatibility analysis

Immunohistochemical analysis of an implant is usually the last step of chronic studies sand is essential in assessing the biocompatibility of the device and tissue response. A non-biocompatible device does not only damage the surrounding tissue, it can also affect neural recording, the long-term performance of the device and also the animal health. For example, an inflammatory response may cause the formation of astrocytes, which causes a barrier between the recording electrode and neurons and reduces the quality of signal and shortens the lifespan of the probe. Overall, biocompatibility analysis needs to be done in order to complete the study of the fiber probes. More information about the importance and the effects of biocompatibility on neural recording is described in Section 1.3.1.

Two weeks after implantation with PC/COC/AgNW/PDMS or COCE/AgNW/PDMS probes, wild type mice (n=3 per device) were anesthetized via intraperitoneal injection of Fatal Plus solution (100 mg/kg in saline), and perfused with 4% paraformaldehyde (PFA) in phosphate buffered saline (PBS). Spinal cords were extracted and fixed in 4% PFA overnight, and then sliced into 50 μm coronal sections using a vibrating blade microtome (Leica VT1000S). Sections wereblocked in 0.3% (vol/vol) Triton X-100 and 3% (vol/vol) donkey serum in PBS for 30 min. This was followed by overnight incubation at 4°C in a solution of primary antibodies (goat anti-GFAP 1:1000; rabbit anti-NeuN, 1:500, Fisher Scientific) and 3% donkey serum in PBS. Following incubation, the sections were washed 3 times for 30 min each with PBS. The slices were then incubated with secondary antibodies (Alexa Fluor 488 donkey anti-goat 1:1000; Alexa Fluor 633 donkey anti-rabbit 1:1000, Life Technologies) for 1 hour at room temperature. Following 3 more washes with PBS, slices were mounted using PVA-Dabco (Sigma) onto glass microscope slides. A laser

scanning confocal microscope (Fluoview FV1000, Olympus) with 10X (air, NA= 0.16) objective was used for image acquisition.

Staining with antibodies against glial fibrillary acidic protein (GFAP) of the spinal cord tissue surrounding the fiber probes indicated modest astrocytic presence, for the devices positioned on the surfaces as well as within the tissue two weeks after the implantation surgeries (Figure 4.16). Furthermore, the depth probes reaching into the grey matter do not appear to interfere with the viability of the surrounding neuronal populations (Figures 4.16D-E).

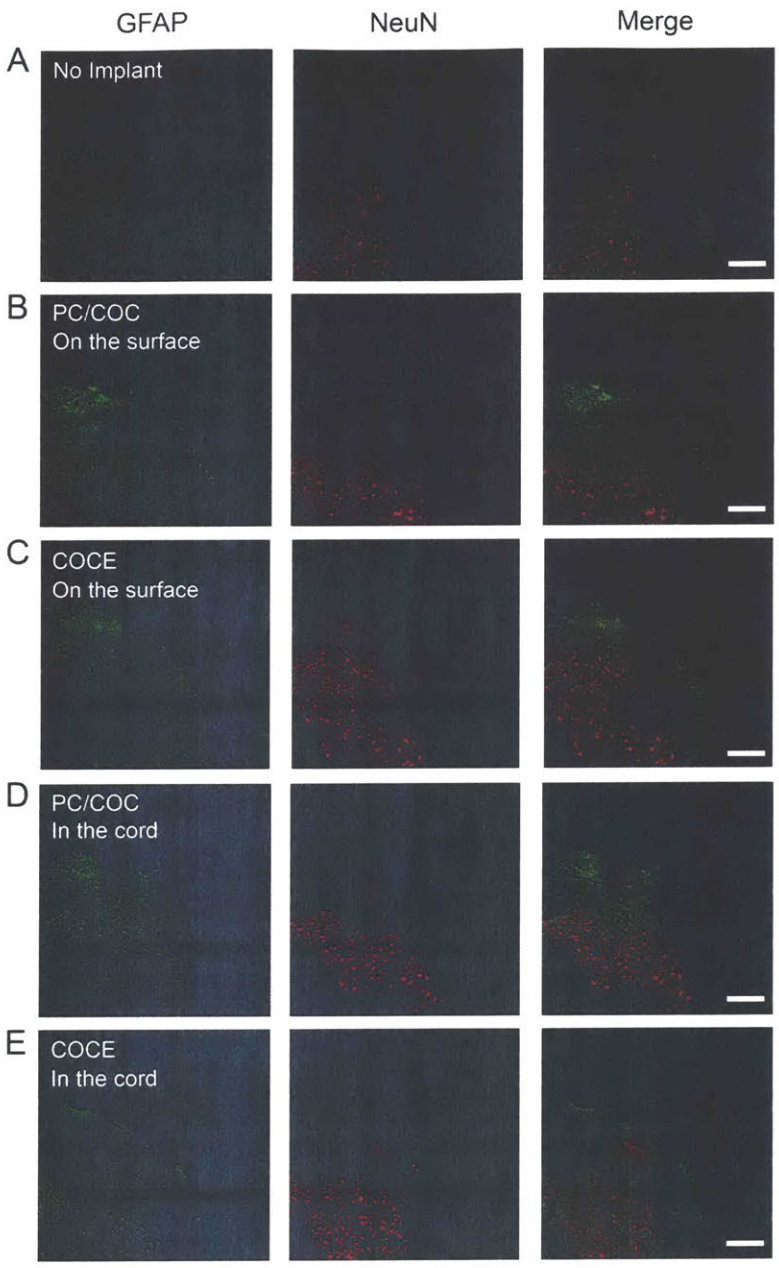

Figure 4.16 Immunohistochemical analysis of the dorsal horn
GFAP (green) marks astrocytes, and NeuN (red) labels neurons. Scale bar is 100 μm. (A) Confocal micrographs of a transverse section of the lumbar spinal cord without an implant. (B) Transverse section of the lumbar spinal cord from a mouse implanted with a PC/COC/AgNW/PDMS probe for two weeks. The device was positioned on the spinal cord surface. (C) Confocal micrographs of a transverse section of the lumbar spinal cord from a mouse implanted with a PC/COC/AgNW/PDMS probe for two weeks. The device was positioned on the spinal cord surface. (D) Transverse section of the lumbar spinal cord from a mouse implanted with a PC/COC/AgNW/PDMS probe for two weeks. The device was inserted into the spinal cord. (E) Confocal micrographs of a transverse section of the lumbar spinal cord from a mouse implanted with a PC/COC/AgNW/PDMS probe for two weeks. The device was inserted into the spinal cord. No tissue erosion and negligible astrocyte proliferation were observed.

4.7 Conclusions

The following milestones have been achieved with the stretchable and flexible neural probes:

- Simultaneous optical stimulation and neural recording in the mouse spinal cords
- Recording of isolated action potentials in the mouse spinal cord
- Recording of compound activity in the spinal cord of freely moving mice

All of these are important achievements in the development of tools enabling investigation of spinal cord circuits; especially the recording of compound activity in freely moving mouse spinal cord, which is to our knowledge, the first time in the field.

Chapter V Summary

5.1 Significance

This thesis aimed to develop a set of tools for probing of spinal cord circuits in rodent models to facilitate the understanding and treatment of spinal cord injury. Fiber drawing process was applied to the design and fabrication of the flexible neural probes. Three material sets were developed for the design and fabrication of flexible neural probes to address the criteria necessary for these probes.

An all-polymer system, integrating a waveguide with polycarbonate (PC) core and cyclic olefin copolymer (COC) cladding and conductive poly ethylene (CPE) electrodes, was first introduced. The probes enabled the simultaneous recording and optical stimulation in the spinal cord of transgenic mice expressing the light sensitive protein ChR2. The optical stimulation could not only evoke neural activity, which was record with the electrodes integrated into the same neural probe, but also induced limb movement. This study was the first work to demonstrate the simultaneous optical stimulation and neural recording of mice spinal cord. In addition, the probes were relatively softer than conventionally used metallic electrodes and therefore partially addressed the problem of the mismatch in mechanical properties between the neural interface and neurons. However, the

probes could only be used in anesthetized mice because the neural probes were not small or soft enough for chronic implantation. In addition, the quality of neural recording was not adequate for single-unit resolution. The work, however, for the first time, introduced a new tool for neuroscientists to investigate neural circuits in the mouse spinal cord.

The neural recording capability of the PC/COC/CPE was limited by the high impedance of CPE, Thus, to reduce the fiber impedance, carbon nanofiber (CNF)-doped polymer composites were used instead of CPE as the electrode. The conductivity of the CNF electrodes was optimized by adjusting the composition of thermoplastic polymers and CNF. To enable the thermal drawing of these composites, the thermomechanical properties of the composites were investigated. Based on the similarity in the T_g, the materials were co-drawn with PC. It was observed that loading more than 10 wt% of CNF to the composite increase the bulk conductivity of polymer. However, high amounts of CNF (above 5%) also increased the viscosity of the polymer to a point in which the composite could not be thermally drawn. *In vivo* tests were done using 10 wt% CNF-COC electrodes. Optically evoked neural activity was recorded in mouse brain with improved SNR compared to the previous work. Although the SNR was improved, the resolution was still not adequate for singe-unit recording in the spinal cord.

Next, to enable single-unit recording while using flexible probes, silver nanowire (AgNW) coated flexible and stretchable fibers were developed. AgNW meshes were used as electrodes and coated on PC/COC and also cyclic olefin copolymer elastomer (COCE) fibers. After thermal drawing process, the fibers maintained high transmission under bending and stretching deformations. Moreover, when coated with AgNWs, conductivity was preserved under repetitive deformation. The superior mechanical properties and performance of this stretchable neural probes enabled the first chronic implantation and recorded compound activity in mouse spinal cord.

5.2 Future directions

There are a few potential directions for improvement of the devices and applications described in this thesis:

Design:

- More recording channels per neural probe to increase resolution[84,90,125] would enhance the prosthetic and research ability of these fibers.
- Integrated light emitting diodes would eliminate fiber-coupling to laser sources and reduce the weight of the implant.

Materials:

- Silver nanowires should be replaced by more biocompatible and stable conductive particles, e.g. gold nanoparticles, for the conductive meshes within stretchable probes.
- Utilizing photo-patternable elastomers may allow for isolation of conductive layers and enable multi-channel recording[234].

Neurobiological studies:

- Applying the neural probes to different animal models to investigate neural circuits in the spinal cord
- Applying fiber-based tools to injury models to assess their prosthetic potentials

References

1 Dafny, N. in *Sensory Systems* (The University of Texas Health Science Center at Houston 1997).

2 Harrison, M. *et al.* Vertebral landmarks for the identification of spinal cord segments in the mouse. *NeuroImage* **68**, 22-29, doi:10.1016/j.neuroimage.2012.11.048 (2013).

3 Dijkers, M. Quality of life after spinal cord injury: a meta analysis of the effects of disablement components. *Spinal cord* **35**, 829-840 (1997).

4 Westgren, N. & Levi, R. Quality of life and traumatic spinal cord injury. *Archives of physical medicine and rehabilitation* **79**, 1433-1439 (1998).

5 Vastenholt, J. M. *et al.* A 7-year follow-up of sacral anterior root stimulation for bladder control in patients with a spinal cord injury: quality of life and users' experiences. *Spinal Cord* **41**, 397 (2003).

6 Kennedy, P., Lude, P. & Taylor, N. Quality of life, social participation, appraisals and coping post spinal cord injury: a review of four community samples. *Spinal cord* **44**, 95-105 (2006).

7 Dumont, R. J. *et al.* Acute spinal cord injury, part I: pathophysiologic mechanisms. *Clinical neuropharmacology* **24**, 254-264 (2001).

8 McDonald, J. W. & Sadowsky, C. Spinal-cord injury. *The Lancet* **359**, 417-425 (2002).

9 Kralj, A. R. & Bajd, T. *Functional electrical stimulation: standing and walking after spinal cord injury*. (CRC press, 1989).

10 Stojanovic, M. P. & Abdi, S. Spinal cord stimulation. *Pain Physician* **5**, 156 (2002).

11 Ragnarsson, K. Functional electrical stimulation after spinal cord injury: current use, therapeutic effects and future directions. *Spinal cord* **46**, 255-274 (2008).

12 Deisseroth, K. Optogenetics. *Nature methods* **8**, 26-29, doi:10.1038/nmeth.f.324 (2011).

13 Deisseroth, K. Optogenetics and psychiatry: applications, challenges, and opportunities. *Biological psychiatry* **71**, 1030-1032, doi:10.1016/j.biopsych.2011.12.021 (2012).

14 Montgomery, K. L., Iyer, S. M., Christensen, A. J., Deisseroth, K. & Delp, S. L. Beyond the brain: Optogenetic control in the spinal cord and peripheral nervous system. *Science translational medicine* **8**, 337rv335-337rv335 (2016).

15 Minev, I. R. *et al.* Electronic dura mater for long-term multimodal neural interfaces. *Science* **347**, 159-163 (2015).

16 Park, S. I. *et al.* Soft, stretchable, fully implantable miniaturized optoelectronic systems for wireless optogenetics. *Nature biotechnology* **33**, 1280-1286, doi:10.1038/nbt.3415 (2015).

17 John Wiley & Sons, I. *Examples of neural circuits*, <http://higheredbcs.wiley.com/legacy/college/tortora/0470565101/hearthis_ill/pap13e_ch12_illustr_audio_mp3_am/simulations/hear/neural_circuits.html> (2011).

18 Kandel, E. R., Schwartz, J. H., Jessell, T. M., Siegelbaum, S. A. & Hudspeth, A. J. *Principles of neural science*. Vol. 4 (McGraw-hill New York, 2000).

19 Purves, D. *et al.* Neuroscience. *Sinauer Associate* (2001).

20 Piccolino, M. Luigi Galvani and animal electricity: two centuries after the foundation of electrophysiology. *Trends in Neurosciences* **20**, 443-448, doi:10.1016/S0166-2236(97)01101-6 (1997).

21 Piccolino, M. & Bresadola, M. *Shocking frogs: Galvani, Volta, and the electric origins of neuroscience*. (Oxford University Press, USA, 2013).
22 Buzsáki, G., Anastassiou, C. A. & Koch, C. The origin of extracellular fields and currents — EEG, ECoG, LFP and spikes. *Nat Rev Neurosci* **13**, 407-420, doi:10.1038/nrn3241 (2012).
23 Law, S. K. Thickness and resistivity variations over the upper surface of the human skull. *Brain topography* **6**, 99-109 (1993).
24 Rey, H. G., Pedreira, C. & Quian Quiroga, R. Past, present and future of spike sorting techniques. *Brain Research Bulletin* **119**, 106-117, doi:10.1016/j.brainresbull.2015.04.007 (2015).
25 Gold, C., Henze, D. A., Koch, C. & Buzsáki, G. On the origin of the extracellular action potential waveform: a modeling study. *Journal of neurophysiology* **95**, 3113-3128 (2006).
26 Quiroga, R. Spike sorting. *Scholarpedia* **2**, 3583, doi:10.4249/scholarpedia.3583 (2007).
27 Bain, P. *Deep brain stimulation*. (Oxford University Press, 2009).
28 Coghlan, E. *New Spinal Cord Stimulation Therapy Showing Promising Results*, <http://nationalpainreport.com/new-spinal-cord-stimulation-therapy-showing-promising-results-8825861.html> (2015).
29 Bruijnzeel, H. *et al.* Systematic Review on Surgical Outcomes and Hearing Preservation for Cochlear Implantation in Children and Adults. *Otolaryngology–Head and Neck Surgery* **154**, 586-596, doi:10.1177/0194599815627146 (2016).
30 Clausen, J. Visual sensations (phosphenes) produced by AC sine wave stimulation. (1955).
31 Dobelle, W. H., Mladejovsky, M. G. & Girvin, J. P. Artificial vision for the blind: electrical stimulation of visual cortex offers hope for a functional prosthesis. *Science* **183**, 440-444 (1974).
32 Parsonnet, P. S. G. V. & Smyth, N. P. Implantable cardiac pacemakers: Status report and resource guideline. *The American journal of cardiology* **34**, 487-500 (1974).
33 Li, Q. *et al.* Therapeutic deep brain stimulation in Parkinsonian rats directly influences motor cortex. *Neuron* **76**, 1030-1041, doi:10.1016/j.neuron.2012.09.032 (2012).
34 Nguyen, T. K. *et al.* Closed-loop optical neural stimulation based on a 32-channel low-noise recording system with online spike sorting. *Journal of neural engineering* **11**, 046005, doi:10.1088/1741-2560/11/4/046005 (2014).
35 Mehta, N. *Spinal cord stimulation for chronic bacm and neck pain*, <http://www.spine-health.com/treatment/back-surgery/spinal-cord-stimulation-chronic-back-and-neck-pain> (2016).
36 Lavrov, I. *et al.* Facilitation of stepping with epidural stimulation in spinal rats: role of sensory input. *The Journal of neuroscience : the official journal of the Society for Neuroscience* **28**, 7774-7780, doi:10.1523/JNEUROSCI.1069-08.2008 (2008).
37 Edgerton, V. R. & Harkema, S. Epidural stimulation of the spinal cord in spinal cord injury: current status and future challenges. *Expert review of neurotherapeutics* **11**, 1351-1353 (2011).
38 Harkema, S. *et al.* Effect of epidural stimulation of the lumbosacral spinal cord on voluntary movement, standing, and assisted stepping after motor complete paraplegia: a case study. *The Lancet* **377**, 1938-1947 (2011).
39 Faghri, P. D., Glaser, R. M. & Figoni, S. F. Functional electrical stimulation leg cycle ergometer exercise: training effects on cardiorespiratory responses of spinal cord injured

subjects at rest and during submaximal exercise. *Archives of physical medicine and rehabilitation* **73**, 1085-1093 (1992).

40 Navarro, X. *et al.* A critical review of interfaces with the peripheral nervous system for the control of neuroprostheses and hybrid bionic systems. *Journal of the Peripheral Nervous System* **10**, 229-258 (2005).

41 Frey, O. *et al.* Simultaneous neurochemical stimulation and recording using an assembly of biosensor silicon microprobes and SU-8 microinjectors. *Sensors and Actuators B: Chemical* **154**, 96-105 (2011).

42 Stauffer, W., Lau, P., Bi, G. & Cui, X. Rapid modulation of local neural activity by controlled drug release from polymer-coated recording microelectrodes. *Journal of neural engineering* **8**, 044001 (2011).

43 Canales, A. *et al.* Multifunctional fibers for simultaneous optical, electrical and chemical interrogation of neural circuits in vivo. *Nature biotechnology*, doi:10.1038/nbt.3093 (2015).

44 Serwer, L., Hashizume, R., Ozawa, T. & James, C. D. Systemic and local drug delivery for treating diseases of the central nervous system in rodent models. *JoVE (Journal of Visualized Experiments)*, e1992-e1992 (2010).

45 Casati, A. & Vinciguerra, F. Intrathecal anesthesia. *Current Opinion in Anesthesiology* **15**, 543-551 (2002).

46 Chen, R. *et al.* Depression of motor cortex excitability by low-frequency transcranial magnetic stimulation. *Neurology* **48**, 1398-1403 (1997).

47 Corthout, E., Barker, A. & Cowey, A. Transcranial magnetic stimulation. *Experimental brain research* **141**, 128-132 (2001).

48 Hallett, M. Transcranial magnetic stimulation and the human brain. *Nature* **406**, 147-150 (2000).

49 Groppa, S. *et al.* A practical guide to diagnostic transcranial magnetic stimulation: Report of an IFCN committee. *Clinical Neurophysiology* **123**, 858-882, doi:10.1016/j.clinph.2012.01.010 (2012).

50 Lefaucheur, J.-P. *et al.* Evidence-based guidelines on the therapeutic use of repetitive transcranial magnetic stimulation (rTMS). *Clinical Neurophysiology* **125**, 2150-2206, doi:10.1016/j.clinph.2014.05.021 (2014).

51 Miller, M. C. Vol. 2017 *Harvard Medical School* (Harvard Health Blog, 2012).

52 Nakayama, T., Hammel, H., Hardy, J. & Eisenman, J. Thermal stimulation of electrical activity of single units of the preoptic region. *American Journal of Physiology--Legacy Content* **204**, 1122-1126 (1963).

53 Chen, R., Romero, G., Christiansen, M. G., Mohr, A. & Anikeeva, P. Wireless magnetothermal deep brain stimulation. *Science* **347**, 1477-1480 (2015).

54 Shapiro, M. G., Homma, K., Villarreal, S., Richter, C.-P. & Bezanilla, F. Infrared light excites cells by changing their electrical capacitance. *Nature Communications* **3**, 736, doi:10.1038/ncomms1742 (2012).

55 Thompson, A. C., Wade, S. A., Pawsey, N. C. & Stoddart, P. R. Infrared neural stimulation: influence of stimulation site spacing and repetition rates on heating. *IEEE Transactions on Biomedical Engineering* **60**, 3534-3541 (2013).

56 Fenno, L., Yizhar, O. & Deisseroth, K. The development and application of optogenetics. *Annual review of neuroscience* **34**, 389-412, doi:10.1146/annurev-neuro-061010-113817 (2011).

57 Yizhar, O., Fenno, L. E., Davidson, T. J., Mogri, M. & Deisseroth, K. Optogenetics in neural systems. *Neuron* **71**, 9-34 (2011).
58 Iyer, S. M. *et al.* Virally mediated optogenetic excitation and inhibition of pain in freely moving nontransgenic mice. *Nature biotechnology* **32**, 274-278, doi:10.1038/nbt.2834 (2014).
59 Pashaie, R. *et al.* Optogenetic Brain Interfaces. *Biomedical Engineering, IEEE Reviews in* **7**, 3-30, doi:10.1109/RBME.2013.2294796 (2014).
60 Iyer, S. M. & Delp, S. L. Neuroscience. Optogenetic regeneration. *Science* **344**, 44-45, doi:10.1126/science.1253088 (2014).
61 Rattay, F. The basic mechanism for the electrical stimulation of the nervous system. *Neuroscience* **89**, 335-346 (1999).
62 Wheeler, A. H. *Spinal Cord Stimulation Technique*, <http://emedicine.medscape.com/article/1980819-technique> (2015).
63 Aravanis, A. M. *et al.* An optical neural interface: in vivo control of rodent motor cortex with integrated fiberoptic and optogenetic technology. *Journal of neural engineering* **4**, S143 (2007).
64 Turner, J. A., Loeser, J. D., Deyo, R. A. & Sanders, S. B. Spinal cord stimulation for patients with failed back surgery syndrome or complex regional pain syndrome: a systematic review of effectiveness and complications. *Pain* **108**, 137-147 (2004).
65 Sack, B. K. & Herzog, R. W. Evading the immune response upon in vivo gene therapy with viral vectors. *Current opinion in molecular therapeutics* **11**, 493 (2009).
66 Izzo, A. D. *et al.* Optical parameter variability in laser nerve stimulation: a study of pulse duration, repetition rate, and wavelength. *IEEE Transactions on Biomedical Engineering* **54**, 1108-1114 (2007).
67 Izzo, A. D. *et al.* Laser stimulation of auditory neurons: effect of shorter pulse duration and penetration depth. *Biophysical journal* **94**, 3159-3166 (2008).
68 Wells, J. *et al.* Biophysical Mechanisms of Transient Optical Stimulation of Peripheral Nerve. *Biophysical Journal* **93**, 2567-2580, doi:10.1529/biophysj.107.104786 (2007).
69 Boyden, E. S., Zhang, F., Bamberg, E., Nagel, G. & Deisseroth, K. Millisecond-timescale, genetically targeted optical control of neural activity. *Nature neuroscience* **8**, 1263-1268, doi:10.1038/nn1525 (2005).
70 Kramer, R. H., Fortin, D. L. & Trauner, D. New photochemical tools for controlling neuronal activity. *Curr Opin Neurobiol* **19**, 544-552, doi:10.1016/j.conb.2009.09.004 (2009).
71 Albert, E. S. *et al.* TRPV4 channels mediate the infrared laser-evoked response in sensory neurons. *Journal of neurophysiology* **107**, 3227-3234 (2012).
72 Güler, A. D. *et al.* Heat-evoked activation of the ion channel, TRPV4. *Journal of Neuroscience* **22**, 6408-6414 (2002).
73 Nagel, G. *et al.* Channelrhodopsin-2, a directly light-gated cation-selective membrane channel. *Proceedings of the National Academy of Sciences of the United States of America* **100**, 13940-13945, doi:10.1073/pnas.1936192100 (2003).
74 Fiala, A., Suska, A. & Schlüter, O. M. Optogenetic Approaches in Neuroscience. *Current Biology* **20**, R897-R903, doi:10.1016/j.cub.2010.08.053 (2010).
75 Zhang, F., Aravanis, A. M., Adamantidis, A., de Lecea, L. & Deisseroth, K. Circuit-breakers: optical technologies for probing neural signals and systems. *Nature Reviews Neuroscience* **8**, 577-581 (2007).

76 Zhang, F. *et al.* Multimodal fast optical interrogation of neural circuitry. *Nature* **446**, 633-639 (2007).
77 López-Muñoz, F., Boya, J. & Alamo, C. Neuron theory, the cornerstone of neuroscience, on the centenary of the Nobel Prize award to Santiago Ramón y Cajal. *Brain Research Bulletin* **70**, 391-405, doi:10.1016/j.brainresbull.2006.07.010 (2006).
78 Adrian, E. D. The Basis of Sensation. *British Medical Journal* **1**, 287-290 (1954).
79 Woldring, S. & Dirken, M. Spontaneous unit-activity in the superficial cortical layers. *Acta physiologica et pharmacologica Neerlandica* **1**, 369-379 (1950).
80 Dowben, R. M. & Rose, J. E. A metal-filled microelectrode. *Science* **118**, 22-24 (1953).
81 Hubel, D. H. Tungsten microelectrode for recording from single units. *Science* **125**, 549-550 (1957).
82 Strumwasser, F. Long-term recording from single neurons in brain of unrestrained mammals. *Science* **127**, 469-470 (1958).
83 Marg, E. & Adams, J. E. Indwelling multiple micro-electrodes in the brain. *Electroencephalography and clinical neurophysiology* **23**, 277-280 (1967).
84 BeMent, S. L., Wise, K. D., Anderson, D. J., Najafi, K. & Drake, K. L. Solid-state electrodes for multichannel multiplexed intracortical neuronal recording. *IEEE transactions on biomedical engineering*, 230-241 (1986).
85 Hoogerwerf, A. C. & Wise, K. D. A three-dimensional microelectrode array for chronic neural recording. *IEEE Transactions on Biomedical Engineering* **41**, 1136-1146 (1994).
86 McApline, K. (ed Kate McApline) (2015).
87 Normann, R. A., Campbell, P. K. & Jones, K. E. in *Engineering in Medicine and Biology Society, 1989. Images of the Twenty-First Century., Proceedings of the Annual International Conference of the IEEE Engineering in.* 939-940 (IEEE).
88 Campbell, P. K., Normann, R. A., Horch, K. W. & Stensaas, S. A chronic intracortical electrode array: preliminary results. *Journal of biomedical materials research* **23**, 245-259 (1989).
89 Jones, K. E., Campbell, P. K. & Normann, R. A. A glass/silicon composite intracortical electrode array. *Annals of biomedical engineering* **20**, 423-437 (1992).
90 Nordhausen, C. T., Rousche, P. J. & Normann, R. A. Optimizing recording capabilities of the Utah Intracortical Electrode Array. *Brain Research* **637**, 27-36, doi:10.1016/0006-8993(94)91213-0 (1994).
91 Rousche, P. J. & Normann, R. A. Chronic recording capability of the Utah Intracortical Electrode Array in cat sensory cortex. *Journal of neuroscience methods* **82**, 1-15 (1998).
92 Gordon Kindlmann, R. A. N., Arun Badi, James Bigler, Charles Keller, Richard Coffey, Greg M. Jones, Christopher R. Johnson. in *NIH Symposium on Biocomputation & Bioinformation Digital Biology: The Emerging Paradigm* (Maryland, USA, 2003).
93 Hatsopoulos, N. G. & Donoghue, J. P. The science of neural interface systems. *Annual review of neuroscience* **32**, 249 (2009).
94 Polikov, V. S., Tresco, P. A. & Reichert, W. M. Response of brain tissue to chronically implanted neural electrodes. *Journal of neuroscience methods* **148**, 1-18 (2005).
95 Ward, M. P., Rajdev, P., Ellison, C. & Irazoqui, P. P. Toward a comparison of microelectrodes for acute and chronic recordings. *Brain research* **1282**, 183-200 (2009).
96 Lee, H., Bellamkonda, R. V., Sun, W. & Levenston, M. E. Biomechanical analysis of silicon microelectrode-induced strain in the brain. *Journal of neural engineering* **2**, 81 (2005).

97 Barrese, J. C. *et al.* Failure mode analysis of silicon-based intracortical microelectrode arrays in non-human primates. *Journal of neural engineering* **10**, 066014 (2013).
98 Lind, G., Linsmeier, C. E. & Schouenborg, J. The density difference between tissue and neural probes is a key factor for glial scarring. *Scientific reports* **3** (2013).
99 Szarowski, D. *et al.* Brain responses to micro-machined silicon devices. *Brain research* **983**, 23-35 (2003).
100 Kotzar, G. *et al.* Evaluation of MEMS materials of construction for implantable medical devices. *Biomaterials* **23**, 2737-2750 (2002).
101 Chen, R., Canales, A. & Anikeeva, P. Neural recording and modulation technologies. *Nature Reviews Materials* **2**, 16093 (2017).
102 Cardarelli, F. *Materials handbook: a concise desktop reference.* (Springer Science & Business Media, 2008).
103 Green, J. A simple microelectrode for recording from the central nervous system. *Nature* **182**, 962-962 (1958).
104 (Cambridge University Engineering Department, 2003).
105 Campbell, P. K., Jones, K. E., Huber, R. J., Horch, K. W. & Normann, R. A. A silicon-based, three-dimensional neural interface: manufacturing processes for an intracortical electrode array. *Biomedical Engineering, IEEE Transactions on* **38**, 758-768 (1991).
106 Buzsaki, G. Large-scale recording of neuronal ensembles. *Nature neuroscience* **7**, 446-451, doi:10.1038/nn1233 (2004).
107 Rogers, J. A., Someya, T. & Huang, Y. Materials and mechanics for stretchable electronics. *Science* **327**, 1603-1607 (2010).
108 Brian, J. K. & Ellis, M. Review of polymer MEMS micromachining. *Journal of Micromechanics and Microengineering* **26**, 013001 (2016).
109 McCoul, D., Hu, W., Gao, M., Mehta, V. & Pei, Q. Recent Advances in Stretchable and Transparent Electronic Materials. *Advanced Electronic Materials*, n/a-n/a, doi:10.1002/aelm.201500407 (2016).
110 Kim, T. I. *et al.* Injectable, cellular-scale optoelectronics with applications for wireless optogenetics. *Science* **340**, 211-216, doi:10.1126/science.1232437 (2013).
111 Rodger, D. C. *et al.* Flexible parylene-based multielectrode array technology for high-density neural stimulation and recording. *Sensors and Actuators B: chemical* **132**, 449-460 (2008).
112 Lacour, S. P., Courtine, G. & Guck, J. Materials and technologies for soft implantable neuroprostheses. *Nature Reviews Materials* **1**, 16063 (2016).
113 Patolsky, F. *et al.* Detection, stimulation, and inhibition of neuronal signals with high-density nanowire transistor arrays. *Science* **313**, 1100-1104 (2006).
114 Keefer, E. W., Botterman, B. R., Romero, M. I., Rossi, A. F. & Gross, G. W. Carbon nanotube coating improves neuronal recordings. *Nature nanotechnology* **3**, 434-439, doi:10.1038/nnano.2008.174 (2008).
115 Cohen-Karni, T., Qing, Q., Li, Q., Fang, Y. & Lieber, C. M. Graphene and nanowire transistors for cellular interfaces and electrical recording. *Nano letters* **10**, 1098-1102 (2010).
116 Vitale, F., Summerson, S. R., Aazhang, B., Kemere, C. & Pasquali, M. Neural stimulation and recording with bidirectional, soft carbon nanotube fiber microelectrodes. *ACS nano* **9**, 4465-4474 (2015).

117 Azim, E., Jiang, J., Alstermark, B. & Jessell, T. M. Skilled reaching relies on a V2a propriospinal internal copy circuit. *Nature* **508**, 357-363 (2014).
118 Ranck, J. B. Which elements are excited in electrical stimulation of mammalian central nervous system: a review. *Brain research* **98**, 417-440 (1975).
119 Adamantidis, A. R., Zhang, F., Aravanis, A. M., Deisseroth, K. & de Lecea, L. Neural substrates of awakening probed with optogenetic control of hypocretin neurons. *Nature* **450**, 420-424, doi:10.1038/nature06310 (2007).
120 Pastrana, E. Optogenetics: controlling cell function with light. *Nature methods* **8**, 24-25, doi:10.1038/nmeth.f.323 (2010).
121 Zhang, J. *et al.* Integrated device for optical stimulation and spatiotemporal electrical recording of neural activity in light-sensitized brain tissue. *Journal of neural engineering* **6**, 055007, doi:10.1088/1741-2560/6/5/055007 (2009).
122 Wang, J. *et al.* Integrated device for combined optical neuromodulation and electrical recording for chronic in vivo applications. *Journal of neural engineering* **9**, 016001, doi:10.1088/1741-2560/9/1/016001 (2012).
123 Im, M., Cho, I.-J., Wu, F., Wise, K. D. & Yoon, E. in *Micro Electro Mechanical Systems (MEMS), 2011 IEEE 24th International Conference on.* 1051-1054 (IEEE).
124 Royer, S. *et al.* Multi-array silicon probes with integrated optical fibers: light-assisted perturbation and recording of local neural circuits in the behaving animal. *The European journal of neuroscience* **31**, 2279-2291, doi:10.1111/j.1460-9568.2010.07250.x (2010).
125 Anikeeva, P. *et al.* Optetrode: a multichannel readout for optogenetic control in freely moving mice. *Nature neuroscience* **15**, 163-170, doi:10.1038/nn.2992 (2012).
126 Rubehn, B., Wolff, S. B., Tovote, P., Luthi, A. & Stieglitz, T. A polymer-based neural microimplant for optogenetic applications: design and first in vivo study. *Lab Chip* **13**, 579-588, doi:10.1039/c2lc40874k (2013).
127 Warden, M. R. *et al.* A prefrontal cortex-brainstem neuronal projection that controls response to behavioural challenge. *Nature* **492**, 428-432, doi:10.1038/nature11617 (2012).
128 Kravitz, A. V. *et al.* Regulation of parkinsonian motor behaviours by optogenetic control of basal ganglia circuitry. *Nature* **466**, 622-626, doi:10.1038/nature09159 (2010).
129 Letzkus, J. J. *et al.* A disinhibitory microcircuit for associative fear learning in the auditory cortex. *Nature* **480**, 331-335 (2011).
130 Hagglund, M., Borgius, L., Dougherty, K. J. & Kiehn, O. Activation of groups of excitatory neurons in the mammalian spinal cord or hindbrain evokes locomotion. *Nature neuroscience* **13**, 246-252, doi:10.1038/nn.2482 (2010).
131 Hagglund, M. *et al.* Optogenetic dissection reveals multiple rhythmogenic modules underlying locomotion. *Proceedings of the National Academy of Sciences of the United States of America* **110**, 11589-11594, doi:10.1073/pnas.1304365110 (2013).
132 Alilain, W. J. *et al.* Light-induced rescue of breathing after spinal cord injury. *The Journal of neuroscience : the official journal of the Society for Neuroscience* **28**, 11862-11870, doi:10.1523/JNEUROSCI.3378-08.2008 (2008).
133 Caggiano, V., Sur, M. & Bizzi, E. Rostro-caudal inhibition of hindlimb movements in the spinal cord of mice. *PloS one* **9**, e100865 (2014).
134 Liske, H., Qian, X., Anikeeva, P., Deisseroth, K. & Delp, S. Optical control of neuronal excitation and inhibition using a single opsin protein, ChR2. *Scientific reports* **3** (2013).
135 Liske, H. *et al.* Optical inhibition of motor nerve and muscle activity in vivo. *Muscle & nerve* **47**, 916-921 (2013).

136 Dougherty, K. J. *et al.* Locomotor rhythm generation linked to the output of spinal shox2 excitatory interneurons. *Neuron* **80**, 920-933 (2013).
137 Llewellyn, M. E., Thompson, K. R., Deisseroth, K. & Delp, S. L. Orderly recruitment of motor units under optical control in vivo. *Nature medicine* **16**, 1161-1165 (2010).
138 Fiford, R. J. & Bilston, L. E. The mechanical properties of rat spinal cord in vitro. *Journal of biomechanics* **38**, 1509-1515 (2005).
139 Cheng, S., Clarke, E. C. & Bilston, L. E. Rheological properties of the tissues of the central nervous system: a review. *Medical engineering & physics* **30**, 1318-1337 (2008).
140 Sparta, D. R. *et al.* Construction of implantable optical fibers for long-term optogenetic manipulation of neural circuits. *Nature protocols* **7**, 12-23, doi:10.1038/nprot.2011.413 (2012).
141 Wark, H. *et al.* A new high-density (25 electrodes/mm2) penetrating microelectrode array for recording and stimulating sub-millimeter neuroanatomical structures. *Journal of neural engineering* **10**, 045003 (2013).
142 Prasad, A. & Sanchez, J. C. Quantifying long-term microelectrode array functionality using chronic in vivo impedance testing. *Journal of neural engineering* **9**, 026028, doi:10.1088/1741-2560/9/2/026028 (2012).
143 Kao, C. K. Nobel Lecture: Sand from centuries past: Send future voices fast. *Reviews of Modern Physics* **82**, 2299 (2010).
144 Richardson, D., Nilsson, J. & Clarkson, W. High power fiber lasers: current status and future perspectives [Invited]. *JOSA B* **27**, B63-B92 (2010).
145 Abouraddy, A. F. *et al.* Towards multimaterial multifunctional fibres that see, hear, sense and communicate. *Nature materials* **6**, 336-347, doi:10.1038/nmat1889 (2007).
146 Behabtu, N. *et al.* Strong, light, multifunctional fibers of carbon nanotubes with ultrahigh conductivity. *Science* **339**, 182-186, doi:10.1126/science.1228061 (2013).
147 Hart, S. D. *et al.* External reflection from omnidirectional dielectric mirror fibers. *Science* **296**, 510-513 (2002).
148 Bayindir, M. *et al.* Metal–insulator–semiconductor optoelectronic fibres. *Nature* **431**, 826-829 (2004).
149 Shapira, O. *et al.* Surface-emitting fiber lasers. *Optics express* **14**, 3929-3935 (2006).
150 Danto, S. *et al.* Fiber Field-Effect Device Via In Situ Channel Crystallization. *Advanced materials* **22**, 4162-4166 (2010).
151 Kaufman, J. J. *et al.* Thermal drawing of high-density macroscopic arrays of well-ordered sub-5-nm-diameter nanowires. *Nano letters* **11**, 4768-4773, doi:10.1021/nl202583g (2011).
152 Gumennik, A. *et al.* All-in-fiber chemical sensing. *Advanced materials* **24**, 6005-6009, doi:10.1002/adma.201203053 (2012).
153 Stolyarov, A. M. *et al.* Microfluidic directional emission control of an azimuthally polarized radial fibre laser. *Nature Photonics* **6**, 229-233 (2012).
154 Stolyarov, A. M. *et al.* Fabrication and characterization of fibers with built-in liquid crystal channels and electrodes for transverse incident-light modulation. *Applied Physics Letters* **101**, 011108, doi:10.1063/1.4733319 (2012).
155 Kaufman, J. J. *et al.* In-fiber production of polymeric particles for biosensing and encapsulation. *Proceedings of the National Academy of Sciences of the United States of America* **110**, 15549-15554, doi:10.1073/pnas.1310214110 (2013).
156 Daniels, C. A. *Polymers: structure and properties.* (CRC Press, 1989).
157 Lampman, S. *Characterization and failure analysis of plastics.* (ASM International, 2003).

158 Effenberger, J. A., Koerber, K. G., Latorra, M. N. & Petriello, J. V. (Google Patents, 1991).
159 Kruth, J.-P., Levy, G., Schindel, R., Craeghs, T. & Yasa, E.
160 Van Krevelen, D. W. & Te Nijenhuis, K. *Properties of polymers: their correlation with chemical structure; their numerical estimation and prediction from additive group contributions*. (Elsevier, 2009).
161 Escaig, B. & G'sell, C. *Plastic deformation of amorphous and semi-crystalline materials*. (Editions de physique, 1982).
162 Haward, R. N. *The physics of glassy polymers*. (Springer Science & Business Media, 2012).
163 Zhao, J. *et al.* Scalable Manufacturing of Metal Nanoparticles by Thermal Fiber Drawing. *Journal of Micro and Nano-Manufacturing* **4**, 041002 (2016).
164 Tadmor, Z. & Gogos, C. G. *Principles of polymer processing*. (John Wiley & Sons, 2013).
165 Lu, C. *et al.* Polymer Fiber Probes Enable Optical Control of Spinal Cord and Muscle Function In Vivo. *Advanced Functional Materials*, 6594-6600, doi:10.1002/adfm.201401266 (2014).
166 Ivan, P. & Ting, L. Vol. 3 876 (Academic Press, San Diego, CA, 2002).
167 Plummer, W. T. (Google Patents, 2011).
168 Mark, J. Polymer data handbook. *Oxford University Press: New York* (1999).
169 Koleva, M. *Poly(methyl methacrylate) (PMMA)*, <http://webhotel2.tut.fi/projects/caeds/tekstit/plastics/plastics_PMMA.pdf> (
170 Chollet, F. (2013).
171 Hull, R. *Properties of crystalline silicon*. (IET, 1999).
172 Buzsáki, G. Large-scale recording of neuronal ensembles. *Nature neuroscience* **7**, 446-451 (2004).
173 Collins, J. A technique for chronic extracellular recording of neuronal activity in the dorsal horn of the lumbar spinal cord in drug-free, physiologically intact, cats. *Journal of neuroscience methods* **12**, 277-287 (1985).
174 Kennedy, P. R. The cone electrode: a long-term electrode that records from neurites grown onto its recording surface. *Journal of neuroscience methods* **29**, 181-193 (1989).
175 Somboonsub, B. *et al.* Preparation of the thermally stable conducting polymer PEDOT – Sulfonated poly(imide). *Polymer* **51**, 1231-1236, doi:10.1016/j.polymer.2010.01.048 (2010).
176 Skotheim, T. A. & Reynolds, J. *Handbook of Conducting Polymers, 2 Volume Set*. (CRC press, 2007).
177 Alexander, M. D. & Wang, C. S. (Google Patents, 2004).
178 Deng, H. *et al.* Preparation of High-Performance Conductive Polymer Fibers through Morphological Control of Networks Formed by Nanofillers. *Advanced Functional Materials* **20**, 1424-1432 (2010).
179 Koerner, H. *et al.* Deformation–morphology correlations in electrically conductive carbon nanotube—thermoplastic polyurethane nanocomposites. *Polymer* **46**, 4405-4420 (2005).
180 Koerner, H., Price, G., Pearce, N. A., Alexander, M. & Vaia, R. A. Remotely actuated polymer nanocomposites--stress-recovery of carbon-nanotube-filled thermoplastic elastomers. *Nature materials* **3**, 115-120, doi:10.1038/nmat1059 (2004).
181 Moreno, I., Navascues, N., Arruebo, M., Irusta, S. & Santamaria, J. Facile preparation of transparent and conductive polymer films based on silver nanowire/polycarbonate

nanocomposites. *Nanotechnology* **24**, 275603, doi:10.1088/0957-4484/24/27/275603 (2013).
182 Park, J. *et al.* Electromechanical cardioplasty using a wrapped elasto-conductive epicardial mesh. *Science Translational Medicine* **8**, 344ra386 (2016).
183 Wang, C.-S. & Alexander, M. D. (Google Patents, 2004).
184 Bauhofer, W. & Kovacs, J. Z. A review and analysis of electrical percolation in carbon nanotube polymer composites. *Composites Science and Technology* **69**, 1486-1498 (2009).
185 Lee, P. *et al.* Highly stretchable and highly conductive metal electrode by very long metal nanowire percolation network. *Advanced materials* **24**, 3326-3332 (2012).
186 Sandler, J. K. W., Kirk, J. E., Kinloch, I. A., Shaffer, M. S. P. & Windle, A. H. Ultra-low electrical percolation threshold in carbon-nanotube-epoxy composites. *Polymer* **44**, 5893-5899, doi:10.1016/s0032-3861(03)00539-1 (2003).
187 Bilenberg, B., Nielsen, T., Clausen, B. & Kristensen, A. PMMA to SU-8 bonding for polymer based lab-on-a-chip systems with integrated optics. *Journal of Micromechanics and Microengineering* **14**, 814-818, doi:10.1088/0960-1317/14/6/008 (2004).
188 Shenoy, K. V. & Chesteck, C. Neural Prosthetics. *Scholarpedia* **7**, 11854, doi:10.4249/scholarpedia.11854 (2012).
189 Watanabe, K. *et al.* Noninvasive measurement of heartbeat, respiration, snoring and body movements of a subject in bed via a pneumatic method. *Biomedical Engineering, IEEE Transactions on* **52**, 2100-2107 (2005).
190 Williams, J. C., Hippensteel, J. A., Dilgen, J., Shain, W. & Kipke, D. R. Complex impedance spectroscopy for monitoring tissue responses to inserted neural implants. *Journal of neural engineering* **4**, 410 (2007).
191 Arenkiel, B. R. *et al.* In Vivo Light-Induced Activation of Neural Circuitry in Transgenic Mice Expressing Channelrhodopsin-2. *Neuron* **54**, 205-218, doi:10.1016/j.neuron.2007.03.005 (2007).
192 Husch, A., Cramer, N. & Harris-Warrick, R. M. Long-duration perforated patch recordings from spinal interneurons of adult mice. *Journal of Neurophysiology* **106**, 2783-2789, doi:10.1152/jn.00673.2011 (2011).
193 Cardin, J. A. *et al.* Targeted optogenetic stimulation and recording of neurons in vivo using cell-type-specific expression of Channelrhodopsin-2. *Nature protocols* **5**, 247-254, doi:10.1038/nprot.2009.228 (2010).
194 Nicolopoulos-Stournaras, S. & Iles, J. F. Motor neuron columns in the lumbar spinal cord of the rat. *Journal of Comparative Neurology* **217**, 75-85 (1983).
195 De Luca, G. Fundamental concepts in EMG signal acquisition. *Copyright Delsys Inc* (2003).
196 Stein, R. B. *et al.* Principles underlying new methods for chronic neural recording. *Canadian Journal of Neurological Sciences/Journal Canadien des Sciences Neurologiques* **2**, 235-244 (1975).
197 Cogan, S. F. Neural stimulation and recording electrodes. *Annu. Rev. Biomed. Eng.* **10**, 275-309 (2008).
198 in *IROGRAN Thermoplastic Polyurethanes* (Huntsman CORPORATION, 2012).
199 Coleman, J. N. *et al.* Percolation-dominated conductivity in a conjugated-polymer-carbon-nanotube composite. *Physical Review B* **58**, R7492 (1998).
200 LeGrand, D. G. & Bendler, J. T. *Handbook of polycarbonate science and technology*. Vol. 56 (CRC Press, 2000).

201 Pötschke, P., Fornes, T. D. & Paul, D. R. Rheological behavior of multiwalled carbon nanotube/polycarbonate composites. *Polymer* **43**, 3247-3255, doi:10.1016/S0032-3861(02)00151-9 (2002).
202 Dean, D. A., Ramanathan, T., Machado, D. & Sundararajan, R. Electrical Impedance Spectroscopy Study of Biological Tissues. *Journal of electrostatics* **66**, 165-177, doi:10.1016/j.elstat.2007.11.005 (2008).
203 Lu, C. *et al.* Flexible and stretchable nanowire-coated fibers for optoelectronic probing of spinal cord circuits. *Science Advances* **3** (2017).
204 Ma, H., Jen, A. K.-Y. & Dalton, L. R. Polymer-based optical waveguides: materials, processing, and devices. *Advanced materials* **14**, 1339-1365 (2002).
205 Li, H., Qi, Y., Ryle, J. P. & Sheridan, J. T. Self-written waveguides in a dry acrylamide/polyvinyl alcohol photopolymer material. *Applied Optics* **53**, 8086, doi:10.1364/ao.53.008086 (2014).
206 Snakenborg, D., Perozziello, G., Klank, H., Geschke, O. & Kutter, J. P. Direct milling and casting of polymer-based optical waveguides for improved transparency in the visible range. *Journal of Micromechanics and Microengineering* **16**, 375 (2006).
207 Yun, S. *et al.* Polymer-Waveguide-Based Flexible Tactile Sensor Array for Dynamic Response. *Advanced materials*, doi:10.1002/adma.201305850 (2014).
208 Choi, M. *et al.* Light-guiding hydrogels for cell-based sensing and optogenetic synthesis in vivo. *Nat Photon* **7**, 987-994, doi:10.1038/nphoton.2013.278 (2013).
209 Chang-Yen, D. A., Eich, R. K. & Gale, B. K. A monolithic PDMS waveguide system fabricated using soft-lithography techniques. *Journal of lightwave technology* **23**, 2088 (2005).
210 Choi, M., Humar, M., Kim, S. & Yun, S. H. Step-Index Optical Fiber Made of Biocompatible Hydrogels. *Advanced materials* **27**, 4081-4086 (2015).
211 Aden, M., Roesner, A. & Olowinsky, A. Optical characterization of polycarbonate: Influence of additives on optical properties. *Journal of Polymer Science Part B: Polymer Physics* **48**, 451-455 (2010).
212 van Midwoud, P. M., Janse, A., Merema, M. T., Groothuis, G. M. & Verpoorte, E. Comparison of biocompatibility and adsorption properties of different plastics for advanced microfluidic cell and tissue culture models. *Analytical chemistry* **84**, 3938-3944, doi:10.1021/ac300771z (2012).
213 Khanarian, G. Optical properties of cyclic olefin copolymers. *Optical Engineering* **40**, 1024, doi:10.1117/1.1369411 (2001).
214 Amin, S. & Amin, M. Thermoplastic elastomeric (TPE) materials and their use in outdoor electrical insulation. *Reviews on Advanced Materials Science* **29**, 15-30 (2011).
215 Clarke, E. C. in *Neural Tissue Biomechanics* 25-40 (Springer, 2011).
216 Kim, T. K., Kim, J. K. & Jeong, O. C. Measurement of nonlinear mechanical properties of PDMS elastomer. *Microelectronic Engineering* **88**, 1982-1985, doi:10.1016/j.mee.2010.12.108 (2011).
217 Fiedler, E., Haas, N. & Stieglitz, T. in *Engineering in Medicine and Biology Society (EMBC), 2014 36th Annual International Conference of the IEEE.* 438-441 (IEEE).
218 Kymakis, E. & Amaratunga, G. A. Electrical properties of single-wall carbon nanotube-polymer composite films. *Journal of applied physics* **99**, 084302 (2006).

219 Lacour, S. P., Chan, D., Wagner, S., Li, T. & Suo, Z. Mechanisms of reversible stretchability of thin metal films on elastomeric substrates. *Applied Physics Letters* **88**, 204103 (2006).
220 Kim, D. H. *et al.* Epidermal electronics. *Science* **333**, 838-843, doi:10.1126/science.1206157 (2011).
221 Fan, J. A. *et al.* Fractal design concepts for stretchable electronics. *Nat Commun* **5**, doi:10.1038/ncomms4266 (2014).
222 Hu, L., Kim, H. S., Lee, J.-Y., Peumans, P. & Cui, Y. Scalable Coating and Properties of Transparent, Flexible, Silver Nanowire Electrodes. *ACS Nano* **4**, 2955-2963, doi:10.1021/nn1005232 (2010).
223 Lee, M.-S. *et al.* High-performance, transparent, and stretchable electrodes using graphene–metal nanowire hybrid structures. *Nano letters* **13**, 2814-2821 (2013).
224 Guo, C. F., Sun, T., Liu, Q., Suo, Z. & Ren, Z. Highly stretchable and transparent nanomesh electrodes made by grain boundary lithography. *Nature communications* **5** (2014).
225 Yu, Z. *et al.* Highly Flexible Silver Nanowire Electrodes for Shape-Memory Polymer Light-Emitting Diodes. *Advanced materials* **23**, 664-668 (2011).
226 Cortese, B., Mowlem, M. C. & Morgan, H. Characterisation of an irreversible bonding process for COC–COC and COC–PDMS–COC sandwich structures and application to microvalves. *Sensors and Actuators B: Chemical* **160**, 1473-1480 (2011).
227 Quaglio, M. *et al.* Evaluation of different PDMS interconnection solutions for silicon, Pyrex and COC microfluidic chips. *Journal of Micromechanics and Microengineering* **18**, 055012 (2008).
228 van de Groep, J., Spinelli, P. & Polman, A. Transparent conducting silver nanowire networks. *Nano letters* **12**, 3138-3144 (2012).
229 Gunaydin, L. A. *et al.* Ultrafast optogenetic control. *Nature neuroscience* **13**, 387-392, doi:10.1038/nn.2495 (2010).
230 Simone, D. A., Baumann, T. K., Collins, J. & LaMotte, R. H. Sensitization of cat dorsal horn neurons to innocuous mechanical stimulation after intradermal injection of capsaicin. *Brain research* **486**, 185-189 (1989).
231 Kawamata, M. *et al.* Changes in response properties and receptive fields of spinal dorsal horn neurons in rats after surgical incision in hairy skin. *The Journal of the American Society of Anesthesiologists* **102**, 141-151 (2005).
232 Kim, T., Branner, A., Gulati, T. & Giszter, S. F. Braided multi-electrode probes: mechanical compliance characteristics and recordings from spinal cords. *Journal of neural engineering* **10**, 045001 (2013).
233 Prasad, A. & Sahin, M. in *Engineering in Medicine and Biology Society, EMBC, 2011 Annual International Conference of the IEEE.* 2993-2996 (IEEE).
234 Adrega, T. & Lacour, S. P. Stretchable gold conductors embedded in PDMS and patterned by photolithography: fabrication and electromechanical characterization. *Journal of Micromechanics and Microengineering* **20**, 055025 (2010).